Modelling the Anomalous Oxidation Behavior of Zirconium Alloys

by

Isha Gupta

A dissertation submitted in partial fulfillment
of the requirements for the degree of
Doctor of Philosophy
(Mechanical Engineering)
in The University of Michigan
2021

Doctoral Committee:

Professor Wei Lu, Co-Chair
Professor Michael Thouless, Co-Chair
Professor James Barber
Assistant Professor John Heron
Professor Greg Hulbert

Isha Gupta

ishag@umich.edu

ORCID iD: 0000-0002-0382-5855

Dedication

To my parents, sisters, and friends

Acknowledgements

I am most grateful to my advisors, Professor Michael Thouless, Professor James Barber, and Professor Wei Lu, for their enormous contribution in helping me become a better researcher. Their constant guidance, support, and encouragement has been truly enriching and it has been a tremendous privilege to have them as my advisors. I would also like to thank Professor Greg Hulbert and Professor John Heron for their useful insights and comments on this thesis.

I am thankful to the CASL program (http://www.casl.gov), an Energy Innovation Hub (http://www.energy.gov/hubs) for Modeling and Simulation of Nuclear Reactors under U.S. Department of Energy, and the University of Michigan Rackham Graduate School (Rackham Conference Travel Grants) for supporting this research. I appreciate the Department of Mechanical Engineering for giving me the opportunity to be a Graduate Student Instructor for several undergraduate courses. I truly believe teaching to be a two-way learning process and I am thankful to all the undergraduate students I have interacted with as a GSI.

I am sincerely grateful to Professor Vikram Gavini and Professor Ellen Arruda for taking out time to discuss my PhD application to the University of Michigan, and my research interests, before I joined the program. I would also like to thank Professor Yue Fan for offering a great course in molecular dynamics analysis of materials. Concepts learned from his class have been crucial for some of the research presented in this thesis.

I thank my colleagues: Kisik Hong, Dandan Wang, Marie Rice, James Gorman, Will LePage, Kaitlyn Mallett, Callan Luetkemeyer, Tianhan Gao, Zhitong Bai, Benjamin Marchi, and Jon Estrada for insightful technical discussions and their support during my graduate

years. I am also grateful to all my friends in Ann Arbor: Rohith, Neeharika, Bikash, Mayur, Nelson, Anish, Geetha, Neha, Pallav, Sharang, Shruti, and also those outside Ann Arbor: Shalini, Abhishek, and Akansha for all the great times and fun conversations.

I am deeply thankful to my father, as to none of my professional goals would have been fulfilled without his support and encouragement. I am extremely grateful to my sister Neha, for always being there for me. It has been a true blessing having her in my life. I am also thankful to my eldest sister, Amrita, for all her love and support. A big thanks to my lovely nephews, Sid, Daksh, and Darsh, for bringing a smile on my face even on the toughest days.

Lastly, I would like to express my eternal gratefulness to the most important person in my life: my mother, for all of her invisible sacrifices and unconditional love for me. She has been my constant pillar of strength and nothing I have achieved in my life would have been possible without her.

Table of Contents

Dedication ii

Acknowledgements iii

List of Figures viii

List of Tables xiii

Abstract xiv

Chapter

1. Introduction 1

1.1 Overview 1
1.2 Mechanistic modelling of oxide stresses 5
1.3 Martensitic phase transformation in the oxide 5
1.4 Turing model of pattern formation in oxidation-type systems 5
1.5 Candidate mathematical models for Zircaloy oxidation 6

2. Mechanistic Model of Stresses in the Oxide Layer Formed on Zirconium Alloys 7

2.1 Introduction 7
2.2 Statement of the problem 8
2.3 Material behaviour 9
2.3.1 Elastic deformation 9
2.3.2 Thermal strain 10
2.3.3 Substrate creep 10
2.3.4 Oxide creep 11
2.3.5 Oxide growth strains 12
2.4 Calculation of stresses 15
2.4.1 Estimation of $\dot{\epsilon}_0$ 15
2.5 Results 18
2.5.1 Effect of substrate strain 20

2.5.2 Stress distributions . . . 22
2.6 Other geometries . . . 24
2.7 Conclusions . . . 25

3. Energetic Analysis of Constrained Tetragonal-to-Monoclinic Phase Transformation in Polycrystalline Zirconia Films . . . 26

3.1 Introduction . . . 26
3.1.1 Crystallography of tetragonal and monoclinic zirconia . . . 27
3.2 Free-energy continuum framework . . . 30
3.2.1 Calculation of free-energy change ($\Delta G_{T\rightarrow M}$) . . . 32
3.3 Results . . . 40
3.3.1 Effect of grain type and interface conditions . . . 40
3.3.2 Effect of oxide stress and temperature . . . 42
3.3.3 Proposed range for twin boundary energy value (γ_{tw}) . . . 44
3.4 Comparison with experimental observations . . . 45
3.5 Molecular dynamics analysis . . . 46
3.5.1 Modelling framework . . . 46
3.6 Preliminary results . . . 47
3.6.1 Effect of an anion interstitial . . . 48
3.6.2 Effect of a cation substitutional defect . . . 49
3.7 Conclusions . . . 51

4. Application of Turing's Pattern Formation Theory to Oxidation-Type Systems 52

4.1 Introduction . . . 52
4.1.1 Mathematical structure . . . 53
4.1.2 Moving boundary problems . . . 54
4.2 Activator-inhibitor system . . . 55
4.2.1 Numerical procedure . . . 58
4.2.2 Characterization of the model response . . . 58
4.2.3 Dependence of Turing-pattern wavelength on boundary kinetics . . . 64
4.3 Activator-substrate system . . . 70
4.4 Conclusions . . . 73

5. Candidate Mathematical Models for Zircaloy Oxidation . . . 75

5.1 Introduction . . . 75
5.1.1 Diffusion model of oxide growth . . . 75
5.1.2 Wagner's electrochemical-migration model of oxide growth 79
5.1.3 Zircaloy oxidation: Departing from classical models . . . 81
5.2 Turing models for periodic oxidation behavior . . . 82
5.2.1 Weight-gain controlled by metal-oxide interface reaction . . 83

5.2.2 Weight-gain controlled by oxide-oxygen environment interface reaction . . . 86
5.2.3 Proposed activator-inhibitor species in oxide films . . . 89
5.3 An alternative model for Zircaloy oxidation . . . 93
5.3.1 Mathematical structure . . . 93
5.3.2 Model details . . . 96
5.3.3 Model predictions . . . 98
5.3.4 Limitations . . . 100
5.4 Conclusions . . . 101

6. Conclusions and Future Work . . . 102

Bibliography . . . 107

List of Figures

Figure

2.1 Two-sided oxidation of a thin sheet specimen 8

2.2 Estimation of the pre-exponential coefficient $\dot{\epsilon}_0$ in (Equation (2.8)), based on experimental data for the *ex situ* average in-plane compressive stress $|\bar{s}_{\text{ox}}|$ in the oxide [5] at $T = 633$ K. The shaded region represents predicted results for chosen range of oxide's thermal expansion coefficient, $\alpha_{\text{ox}} = 5 \pm 2 \times 10^{-6}$ K^{-1}. 16

2.3 An iterative procedure for the simultaneous solution of Equations (2.10, 2.11). 18

2.4 Comparison of predictions of average in-plane oxide compressive stress ($|\bar{s}_{\text{ox}}|$) at $T = 923$ K and $T = 983$ K with *in-situ* experimental data from [24]. Error bars show the effect of uncertainty in the model parameters. 19

2.5 Comparison of predictions of the present model including substrate strains [solid line] and neglecting them [dashed line] at temperatures $T = 923$ K and $T = 983$ K. The dashed line is obtained from the approximation of Section "An approximate solution". Error bars represent the uncertainty in Zr-4 creep parameters. 21

2.6 Comparison of predictions of in-plane oxide stress (s_{ox}) distribution across its thickness at $T = 688$ K with *ex-situ* experimental data for ZIRLO from [26]. The shaded region represents predicted results for the range $\alpha_{\text{ox}} = 5 \pm 2 \times 10^{-6}$ K^{-1}. 22

2.7 Predicted in-plane stress distribution in the oxide layer at various times t for (a) $T = 633$ K , and (b) $T = 973$ K. Vertical lines represent location of the metal-oxide interface at time t. 23

3.1 Crystal structures of the tetragonal and the monoclinic phases. 28

3.2 2D representation of the deformation required for the tetragonal-to-monoclinic phase transformation, in the plane containing crystal axes a and c. 29

3.3 Geometric representation of the system analyzed in this phase transformation study, considering a tetragonal oxide grain transforming in homogeneous oxide. 31

3.4 Schematic of the grain structure in the oxide film formed on zirconium alloys. Arrows indicate the oxidation stage at which that particular grain structure is observed. 34

3.5 Two possible configurations for phase transformation in a plane perpendicular to the metal-oxide interface. 35
3.6 Crystal orientation in a plane parallel to the metal-oxide interface for (a) a hexagonal grain and (b) an equiaxed grain. Hexagonal grain shows a 60° symmetry with respect to the grain geometry while the equiaxed grain shows a 180° symmetry. 36
3.7 Variation of free energy with twin density for an equiaxed grain. 37
3.8 Finite element simulation of two specific orientations of the hexagonal grain. Case (a) is for $\theta = 0^{o}$ and case (b) is for $\theta = 30^{o}$. Refer Figure 3.6(a) for the description of angle θ. 38
3.9 Deformed grain shapes post-transformation under optimized twinning conditions. Deformations are magnified by a factor of 10. Color contour indicates shear strain in the grain (red/yellow and blue regions have positive and negative shear strains respectively). 40
3.10 Free energy of transformation for all grains for different interface and grain twinning conditions at $T = 633$ K. Smallest equiaxed grain and largest columnar grains provide the maximum and minimum limits on the energy barrier respectively. 42
3.11 Effect of the in-plane compressive stress in the oxide on the strain energy barrier (ΔU) for the phase transformation. The results presented are for an equiaxed grain bonded with the oxide matrix and undergoing twinning. . . 43
3.12 Variation of the chemical driving force $|\Delta G_{ch}|$ and the strain energy barrier ΔU with temperature for a frictionless (or completely incoherent) grain-oxide interface undergoing twinning. 44
3.13 Free energy of transformation of columnar grains with incoherent interface, showing that a twin boundary energy value of $\gamma_{tw} < 0.24$ J/m^2 is required for it to be favorable in the temperature range of $T = 633 - 1000$ K. 45
3.14 Relaxed lattice structures of the two phases of zirconia at $T = 0$ K in absence of any crystallographic defects. Bigger spheres represent the oxygen atoms and the smaller ones represent the zirconium atoms. 48
3.15 Relaxed lattice structures of the two phases of zirconia at $T = 0$ K in the presence of an oxygen interstitial. The atoms are colored based on the coordination number, with blue being the lowest and red the highest. Bigger spheres represent the oxygen atoms and the dots represent the zirconium atoms. 49
3.16 Relaxed lattice structures of the two phases of zirconia at $T = 0$ K with substitution of a zirconium atom (green) with tin atom (pink). The atoms are colored based on the their type. Blue spheres represent the oxygen atoms. 50

4.1 Periodic Behaviour : (a) Contours of $\tilde{u}$ showing periodic transitions between convex-upward segments of the boundary kinetics, each caused by a peak in $\tilde{u}$ at the moving front. The distance traversed between two transitions, $\tilde{h}_{\text{period}}$, is equal to the wavelength ($\tilde{\lambda}$) of the stationary pattern left behind the moving front. (b) Spatiotemporal concentration profile for the species $\tilde{u}$ showing development of peaks at the moving front. $\tilde{x}$ is the distance from the fixed surface. Results are obtained using Gierer-Meinhardt activator (v)-inhibitor (u) kinetics with $\tilde{c}_4 = 0.6$, $R_D = 3/40$, $\tilde{c}_3 = 1$, $\tilde{u}_0 = 1$, $\tilde{v}_{\tilde{h}} = 0.3$, $\tilde{Q} = 1$ and $\tilde{k} = 1$. 60

4.2 Random behaviour: (a) Contours of $\tilde{u}$ showing erratic boundary kinetics. (b) Spatiotemporal evolution of the species $\tilde{u}$ showing random development of peaks at the moving boundary, and the following erratic fluctuations in the amplitude for Gierer-Meinhardt activator (v)-inhibitor (u) kinetics with $\tilde{c}_4 = 1.8$, $R_D = 3/40$, $\tilde{c}_3 = 1$, $\tilde{u}_0 = 1$, $\tilde{v}_{\tilde{h}} = 0.3$, $\tilde{Q} = 1$ and $\tilde{k} = 1$. Homogeneous initial conditions consistent with the boundary conditions are used. 62

4.3 Turing pattern wavelength as a function of the growth-rate parameter $\tilde{k}$ in (Equation (4.11)). Hollow symbols [A] are for $R_D = 1/16$, $\tilde{c}_3 = 0.83$, $\tilde{v}_h = 0.3$ and solid symbols [B] are for $R_D = 3/40$, $\tilde{c}_3 = 1.0$, $\tilde{v}_h = 0.1$. In both cases, $\tilde{c}_4 = 0.5$, $\tilde{u}_0 = 1$ and $\tilde{Q} = 1$. Triangles identify cases leading to peak decay, whilst circles identify cases of peak splitting. Dashed lines represent bounds on wavelengths of stable patterns (see Appendix 4.A). 64

4.4 Periodic behaviour with peak-splitting: (a) Spatiotemporal evolution of the species $\tilde{u}$ showing each peak formed at the boundary splitting once. (b) Contours of $\tilde{u}$ showing a strong transition in the boundary kinetics for each peak formed at the boundary. The peaks farther away from the moving front are observed to be stationary with a wavelength of $\tilde{\lambda}$. Strong transitions are separated by a distance $\tilde{h}_{\text{period}} = 2\tilde{\lambda}$. Results are obtained using Gierer-Meinhardt activator (v)-inhibitor (u) kinetics with $\tilde{c}_4 = 0.5$, $R_D = 3/40$, $\tilde{c}_3 = 1$, $\tilde{u}_0 = 1$, $\tilde{v}_{\tilde{h}} = 0.01$, $\tilde{Q} = 1$ and $\tilde{k} = 1$. 67

4.5 The solid symbols in this map indicate numerical simulations that resulted in pattern formation, and the open symbols indicate numerical simulations that did not result in pattern formation. The triangular symbols indicate conditions under which the boundary moved in a linear fashion, rather than in a periodic fashion. The lower shaded area, and the corresponding circular points, represent a region in which peak-splitting was observed. The upper shaded region represents where chaotic, random behavior was observed that was very sensitive with respect to small changes in the values of input parameters. The lower dotted line corresponds to the condition $\tilde{c}_4 = 5.8R_D$, which is the instability condition of (Equation (4.17)). These results were obtained using Gierer-Meinhardt activator (v)-inhibitor (u) kinetics with $R_D = 0.075$, $\tilde{c}_3 = 1$, $\tilde{u}_0 = 1$, $\tilde{Q} = 1$ and $\tilde{k} = 1$. 69

4.6 Behavior of Schnakenberg's activator-substrate model for $R_D = 3/400$, $\tilde{a} = 0.9$, $\tilde{b} = 0.1$, $\tilde{u}_0 = 1$, $\tilde{v}_h = 0.1$, $\tilde{Q} = 1$ and $\tilde{k} = 0.05$: (a) Contours of $\tilde{u}$ showing troughs developed at the boundary causing periodic transitions between concave-upward segments, in contrast with the convex-upwards behaviour in Fig. 1(b). (b) Contours of $\tilde{v}$ show every second peak formed at the boundary splitting. The peaks farther away from the moving front are observed to be stationary. Peaks in $\tilde{v}$ coincide with troughs in $\tilde{u}$. Transitions are separated by a distance $\tilde{h}_{\text{period}} = (3/2)\tilde{\lambda}$. $\tilde{x}$ is the distance from the fixed surface. . . 72
4.7 Bifurcation diagram for Gierer-Meinhardt activator (v)-inhibitor (u) kinetics with $R_D = 3/40$, $\tilde{c}_3 = 1.0$, $\tilde{c}_4 = 0.5$ (case [B] in Figure 4.3), assuming the domain to be fixed. Solid squares represent the stable steady-states while hollow squares mark the unstable steady-states, obtained under zero-flux boundary conditions. Stable patterns are obtained in the wavelength range of $3.1 < \tilde{\lambda} < 6.8$ (bounds $\tilde{\lambda}_1^{\text{B}}, \tilde{\lambda}_2^{\text{B}}$). H.S.S stands for the homogeneous-steady-state solution of Equation (4.15). 74
5.1 Growth of an oxide layer via diffusion of the oxidizing species (c) from the oxide-oxygen environment interface to the metal-oxide interface. The metal-oxide interface moves by an amount dh in time dt due to the formation of new oxide at the metal-oxide interface. 76
5.2 Deal-Grove model of oxidation. Oxidation kinetics is limited by the reaction kinetics in the initial stages of oxidation $\tilde{t} << 1$. As the oxide layer thickens, the process becomes limited by diffusion, leading to a parabolic behavior. . 78
5.3 Growth of an anion-deficient oxide layer by reaction with the lattice oxygen at the metal-oxide interface. Positively charged anion-vacancies and electrons diffuse to the free surface of the oxide. 79
5.4 Growth kinetics of a locally-electroneutral oxide film obtained from Wagner's theory of electrochemical migration. Limiting behavior is observed to be approximately parabolic. For the case of equal diffusivity of electrons and oxygen vacancies, $D_n = D_v$, electric field contribution is 0 (Equation (5.16)), reducing it to the classical diffusion model of Section 5.1.1. Weight-gain kinetics is only shown for the case $D_n = 1000D_v$. 81
5.5 Schematic of periodic weight-gain kinetics observed during oxidation of Zr alloys such as Zircaloy-4 and ZIRLO (reproduced from [1]). 82
5.6 Behavior of the modified Turing model outlined in Section 5.2.1 showing transitions in the weight-gain kinetics, as well as in the boundary motion kinetics, for (a) $\tilde{k} = 0.01$ and (b) $\tilde{k} = 1$ (refer Equation (5.19) for the description of this constant). Other parameter values are $\tilde{c}_4 = 0.5$, $R_D = 3/40$, $\tilde{c}_3 = 1$, $\tilde{u}_0 = 1$, $\tilde{v}_{\tilde{h}} = 0.1$, $\tilde{Q} = 1$ and $\tilde{k} = 1$, $R2_D = 100$. 86
5.7 Behavior of the modified Turing model of Section 5.2.2 for parameter values of $\tilde{c}_4 = 0.5$, $R_D = 0.009$, $\tilde{c}_3 = 1$, $A = 0.1$, $\tilde{v}_0 = 2$, $\tilde{u}_h = 4$, $\tilde{Q} = 1$ $\tilde{k} = 0.1$, $\tilde{k_2} = 2$, $R2_D = 1$, showing transitions in the (a) weight-gain kinetics, as well as in the (b) boundary motion kinetics. 88
5.8 Assumed shape of a thermally-nucleated monoclinic oxide in a grain of the tetragonal oxide. 90
5.9 Energy landscape with respect to the size of the nucleus. 91

5.10 2D view of a tetragonal grain in a plane parallel to the metal-oxide interface. 91
5.11 Oxide structure considered for the mathematical model outlined in Section 5.3. 97
5.12 Evolution of stress-multiplier σ used in Equations (5.33), (5.34) and (5.36) 98
5.13 Contours of pore density (v) obtained from the model of section Section 5.3. Parameter values of $a = 0.5$, $k_1 = 1$, $k_2 = 1$, $u_0 = 1$, $D_p = 1$, $k_3 = 1$, $s = 1$, $n = 6$, $A = 2$, $b = 1$ and $k = 0.005$ are used in Equations (5.33)–(5.36), (5.43), (5.45) and (5.46). The results show a spatial periodicity in pore distribution correlated with the transitions in the boundary kinetics (as observed experimentally in zr oxide layers) 99
5.14 Phase distribution obtained from the model of section Section 5.3. Parameter values of $a = 0.5$, $k_1 = 1$, $k_2 = 1$, $u_0 = 1$, $D_p = 1$, $k_3 = 1$, $s = 1$, $n = 6$, $A = 2$, $b = 1$ and $k = 0.005$ are used in Equations (5.33)–(5.36), (5.43), (5.45) and (5.46). It shows a spatial periodicity that is approximately correlated with the transitions in the boundary kinetics (as observed experimentally in Zr oxide layers). Also, after initial transients, the phase content does not change away from the interface. 100

List of Tables

Table

3.1 Crystal structure parameters for tetrgonal and monoclinic zirconia 28
3.2 Grain shapes and sizes analyzed in this study 33

Abstract

Zirconium alloys, widely used as the cladding material for fuel rods in pressurized-water-reactors, undergo oxidation during service. The initial oxidation kinetics is very similar in form to that of a classically passivating layer. However, as the oxide layer reaches a certain critical thickness, a sudden increase in the rate of weight-gain is observed while the oxide layer remains adhered to the substrate. This process repeats itself with an approximately regular period in time. Microscopy images reveal a co-related periodicity in the oxide's microstructure as well. The acceleration in the oxidation kinetics associated with these transitions leads to an increase in the amount of hydrogen entering the Zircaloy, limiting the fuel burn-up in the reactors by causing hydrogen embrittlement. The aim of this thesis, therefore, is to develop physics-based-models to understand the mechanisms which govern this anomalous behavior. Specifics of the three major parts of this work are outlined below.

Mechanistic model for oxide growth stresses: The stresses within the oxide layer have been postulated to play an important role in affecting its protectiveness, for example, by allowing crack formation. Therefore, a mechanistic model for the oxide stresses is presented, showing that the oxide deforms primarily by dislocation glide for $T < 900$ K, while the creep of the substrate only becomes significant at higher temperatures. Model predictions also suggest that the transitions in the oxidation kinetics cannot be attributed to a macroscopic fracture of the oxide. Hence, a possible indirect influence of the oxide stresses via a phase transformation is studied next.

Model for the martensitic phase transformation in the oxide: Tetragonal-to-monoclinic phase transformation driven by stress-relaxation has been postulated to affect the porosity of the oxide layer by forming micro-cracks. Therefore, a free-energy-based

framework is developed to investigate its favorability using 3-D twinning-based simulations in ABAQUS. Results show that the loss of coherency at the grain-oxide interface plays a crucial role in driving this phase transformation. Furthermore, the stress evolution within the oxide is found to have a negligible effect on the transformation-energy barriers. Therefore, alternate mathematical models for the periodic oxidation kinetics of Zircaloys are proposed next.

Application of Turing's pattern formation theory to oxidation-type systems: Turing's reaction-diffusion theory has provided crucial insights into the periodic behavior of various physical systems. Candidate mathematical models for Zircaloy oxidation based on the application of this theory to a moving-boundary system are proposed. These models consider two species which satisfy the Turing criteria of pattern formation, and a third species which corresponds to the oxygen ion. Model behavior shows periodic spatial distribution of the Turing species, as well as transitions in the oxidation kinetics [hence reproducing all of the prominent features of the experimental data]. An alternative preliminary oxidation model is proposed, based on the stress-dependent interaction that occurs between two immobile species: tetragonal phase of the oxide, and pores. Model predictions show a spatial periodicity in the distribution of both of these species, in addition to the transitions in the boundary kinetics, as observed experimentally.

In summary, this thesis furthers a largely experimental literature on Zircaloy oxidation with a rigorous quantitative understanding of the underlying physical mechanisms. Furthermore, to the best of our knowledge, this is the first time that mathematical models for the oxidation behavior of Zircaloys have been proposed without using the unreasonable assumption of oxide cracking.

Chapter 1

Introduction

1.1 Overview

Nuclear energy plays a pivotal role in the present times, by providing an approximate 10% of world's electricity. Nuclear reactors have been broadly classified into light-water reactors, and heavy-water reactors, with normal water being used in the former kind and deuterium-mixed water in the latter. Pressurized-water-reactors (PWRs), a specific type of light-water reactors, form the most common category of nuclear reactors. In these reactors, a primary supply of pressurized-water is used as a coolant for controlling the temperature of the reactor core, where fission reaction in the uranium dioxide fuel pellets releases a large amount of energy. This heated, high-pressure water supply is then directed to a heat exchanger, where it transfers heat to a low-pressure secondary water supply, converting it to steam. This steam is then used to drive the power turbines to produce electricity.

Reactor core of a PWR constitutes an assembly of fuel rods, each of which has pellets of uranium dioxide fuel in a cladding tube typically made of a zirconium alloy, e.g that of Zircaloy-4, ZIRLO etc. Zirconium alloys used for this application have low neutron-absorption capability and resistance to high-temperature corrosion and radiation damage, and are generally termed as Zircaloys.

The Zircaloy cladding undergoes oxidation while being exposed to the pressurized water used as a coolant in a PWR. Notably, the oxidation of some of the Zircaloys, such as that

of Zircaloy-4, shows an anomalous behavior. The initial oxidation kinetics are very similar in form to that of a classically passivating layer, with the rate decaying as the oxide layer thickness increases. At a certain critical thickness (depending on the particular alloy and temperature) the layer appears to lose its protective nature, and the oxidation rate resets back to the initial rate corresponding to the absence of any protective layer [1]. This transition occurs without any loss of thickness. As the oxide continues to grow, the kinetics associated with a protective layer are re-established, until the transition occurs again. This cycle repeats itself with a regular period in thickness throughout the oxidation process. Oxidation occurs at the metal-oxide interface, with the oxidizing species diffusing through the oxide to the interface. During the first few hundred nanometers of oxide growth, when the oxidation rate is very rapid, the oxide grains that form at the interface are small and equiaxed. As the oxidation rate slows down, the grains that form at the metal-oxide interface tend to be larger and columnar. The small equiaxed grains are left as a thin layer on top of the columnar grains within the oxide microstructure, as oxidation progresses. After the transition to the faster oxidation kinetics occurs, the grains that form at the interface become small and equiaxed again for the first few hundred nanometers of oxidation after the transition. Once the oxidation rate slows down again, the relatively large columnar grains form again. This alternating structure of a relatively thick region of large columnar grains sandwiched between thin regions of small equiaxed grains repeats itself throughout the oxide, and is visible in transmission-electron microscopy images [2]. The other microstructural feature that is observed near the equiaxed grains that correspond to rapid oxidation are void-like features running parallel to the metal-oxide interface [3].

Oxidation of zirconium is accompanied by a very high Pilling-Bedworth ratio of 1.56, associated with the increase in molar volume upon oxidation. This results in large in-plane compressive stresses within the oxide. In-situ measurements by XRD indicate in-plane compressive stresses of magnitude $2 \sim 4$ GPa [4, 5] within the layer of oxide immediately associated with the metal interface. The magnitude of the stresses within a given element of the

oxide layer then relaxes as the oxidation front proceeds into the metal. While the oxide layer remains relatively thin, this relaxation of stresses is probably associated with creep within the oxide. Furthermore, oxide stress has been postulated to play a significant role in driving the transitions in the oxidation kinetics by allowing the formation of through-thickness cracks. Therefore, in chapter 2 of this thesis, we propose a model for stress-relaxation within the oxide layer and analyze if the stress-distributions allow for the possibility of formation of such cracks.

XRD measurements have also been used to determine the phases in the oxide [6, 7]. The monoclinic phase of zirconia is thermodynamically stable at temperatures below 1400 K, above which the tetragonal phase is stable up to 2600 K, when the cubic phase becomes stable. However, in the oxide layers formed on zirconium alloys, the tetragonal phase is observed even at temperatures well below 1000 K. Studies have shown that the oxide that first forms at the interface with the alloy substrate has a significantly higher fraction of the tetragonal phase ($60\% \sim 80\%$) than the monoclinic phase. The average volume fraction of the tetragonal phase in the oxide layer drops to a limiting value of $5\% \sim 10\%$ when the oxide is very thick. While one set of experiments indicate this drop to occur at a rate that decreases monotonically over time [6, 5], there are others which report a sudden increase in this rate near the observed transitions in the oxidation kinetics [8, 9]. Due to such discrepancies in the experimental trends, which are a possible consequence of both known and unknown factors, e.g type of alloy, manufacturing processes, chemistry of the oxidation environment, specimen preparation etc., it has been challenging to make rigorous conclusions on the behavior of this phase transformation. However, an analytical understanding of this phenomenon is crucial, as it has been postulated to affect the porosity of the oxide layer due to its ability to cause micro-cracks [10]. Therefore, in chapter 3 of this thesis, we focus on developing a quantitative understanding of the energetics of this phase transformation in a free-energy framework.

One of the most prominent feature of zirconium oxidation is a layered appearance of the oxide films reported in several independent microscopy studies [1, 3, 11], wherein each

layer is observed to be separated by periodically located void-like structures. Furthermore, some studies also indicate a periodicity in the spatial distributions of the tetragonal and monoclinic phase fraction [3]. We considered several candidates of pattern formation theories to understand this behavior. Spinodal decomposition has been found to result in periodic microstructures [12]. However, zirconium-oxygen phase diagram does not exhibit a spinodal curve. Patterns have been found to form during dendritic growth as well. This phenomenon, however, generates a pattern at the moving front/interface. Whereas, in case of zirconium oxidation, pattern is observed to form in the wake of the moving metal-oxide interface.

Alan Turing's theory of pattern formation for the type of systems that follow reaction-diffusion type of equations has been widely used to explain patterns in developmental biology [13, 14, 15, 16, 17, 18]. Notably, Turing patterns have been observed to form in the wake of domain boundaries that move at a constant velocity, which makes this theory a reasonable candidate of study to understand the oxidation of Zircaloys. However, in case of zirconium oxidation, we observe a periodicity in the rate of the metal-oxide interface movement that is strongly correlated with the spatial periodicity within the oxide, which hints towards an interdependence between the two phenomenon. Therefore, we want to understand the Turing systems where the process of pattern formation interacts with the boundary motion, which is the focus of chapter 4 of this thesis.

Chapter 5 of this thesis focuses on the mathematical modelling of oxidation of zirconium alloys. We propose necessary modifications to the Turing framework proposed in chapter 4, for the purpose of application to zr alloys. However, this framework requires an extensive list of criteria to be satisfied by the interacting species, which makes it challenging to bridge connections with the actual physical mechanisms. Therefore, we also propose an alternative model for oxidation in zr alloys, based on the the interaction between the tetragonal phase of the oxide and the pores.

In the following sections, we will discuss the specifics of work presented in each of the chapters in brief.

1.2 Mechanistic modelling of oxide stresses

We proposed a mechanistic model for growth stresses in the oxide layer formed on zirconium alloys at the temperatures of $T = 600 - 1000$ K. We consider double-sided oxidation of a plane sheet specimen. This model predicts the evolution of stresses as the oxide thickens, for a given profile of the oxidation temperature with respect to time. Material parameters for elastic deformation, linear, as well as non-linear creep, and thermal expansion are taken from appropriate experimental studies and the resulting predictions for the evolution of the stress distributions are compared with other experimental data. The governing differential equations are solved using an iterative procedure implemented in MATLAB.

1.3 Martensitic phase transformation in the oxide

We developed a free-energy-based framework to investigate the favorability of the martensitic transformation of the tetragonal phase of the oxide to the monoclinic phase for temperatures of $T = 600 - 1000$ K. Finite-element 3D modelling was used to estimate the strain energy barrier for equiaxed and columnar shaped tetragonal grains transforming in a homogeneous matrix of the oxide. The grain sizes considered for the analysis are consistent with the grain morphology observed experimentally in the oxide layers. We supplement this continuum-based-analysis with molecular dynamics simulations to understand the effect of various crytal defects present within the oxide layer on the relative stability of each phase, using LAMMPS software package.

1.4 Turing model of pattern formation in oxidation-type systems

We analyze the behavior of two-species Turing systems with a moving boundary, the motion of which is assumed to be governed by the diffusing species, e.g. oxygen ions in the case of zirconium oxidation. Turing's pattern formation theory involves a system that follows reaction-diffusion type of governing equations. There are two types of system which sat-

isfy Turing's diffusion-driven-instability criterion, activator-inhibitor systems and activator-substrate systems, based on the nature of the reaction terms in the equations. We consider one model of each of these categories. The system of governing PDEs is first transformed to a fixed-domain, and then solved numerically using FlexPDE professional software package.

1.5 Candidate mathematical models for Zircaloy oxidation

Most of the oxidation studies for metals and alloys measure the weight-gain of the sample and use that to obtain an estimate of the oxide-thickness, rather than a direct measurement of the latter. For certain materials, including Zircaloys, the weight-gain kinetics is observed to be periodic in nature ($3 \sim 4$ cycles from the beginning of the oxidation process) [1, 19, 20, 21]. For the particular case of Zircaloys, there is a strong evidence of a correlated periodicity in the rate of movement of the metal-oxide (M-O) interface as well, directly through the oxide-thickness measurements [11], and indirectly through the periodic grain morphology observed within the oxide layer [3]. Therefore, an appropriate model for the oxidation of Zircaloys should exhibit a correlated periodicity in the weight-gain kinetics and the M-O interface movement kinetics for at least a few initial cycles. It should also result in a spatial periodicity that is strongly correlated with the boundary kinetics [3, 2]. We propose modifications of the Turing models outlined in Section 1.4 to reproduce this behavior. These modifications consider a system of 3-species, interacting in a manner that ensures that the species that controls the rate of boundary movement is conserved. We also propose an alternative oxidation model based on the interaction between the tetragonal phase of the oxide and pores, both of which are observed to form periodic spatial distributions within the oxide. This model uses a localized interaction zone at the metal-oxide interface, and immobility of these species to generate a periodic behavior, while satisfying only a subset of the Turing conditions.

Chapter 2

Mechanistic Model of Stresses in the Oxide Layer Formed on Zirconium Alloys

2.1 Introduction

Zirconium alloys are used as the cladding material for fuel rods in a Pressurized-Water Reactor (PWR) because of their low neutron-absorption capability and their resistance to high-temperature corrosion and radiation damage. The cladding undergoes oxidation while being exposed to the pressurized water used as a coolant in a PWR. Oxide films formed on zirconium alloys are subjected to in-plane compressive stresses associated with a Pilling-Bedworth ratio of 1.56 [22]. The compressive stress and the good adherence between the oxide and substrate make these films inherently protective in nature, because the compressive stress prevents the formation of cracks which could provide a low resistance path for diffusion of the oxidizing species. However, despite the compressive stress, transitions in the nature of the oxide and its kinetics have been observed [1]. The resultant accelerated oxidation rates lead to an increase in the amount of hydrogen entering the Zircaloy, and embrittlement by the resultant formation of hydrides, which can place limits on the fuel burn-up in reactors.

The monoclinic phase of zirconia is thermodynamically stable below 1400 K, above which the tetragonal phase is stable up to 2600 K. However, phase-characterization studies [5, 6, 23, 24] show that there is a high density of the tetragonal phase in the oxide film, even at temperatures below 1000 K. It is recognized that the high compressive stresses within the

oxide may be a contributing factor to this observation [25]. Experiments show that both the volume fraction of the tetragonal phase and the compressive stresses in the oxide decrease continuously with time, and this phase transformation has been postulated as a possible trigger for a transition in the oxidation kinetics of zirconium alloys [10].

Since the oxide stresses play an important role in these processes, we would like to be able to predict the evolution of the stress field under varying mechanical and thermal conditions. This is the objective of this chapter.

2.2 Statement of the problem

We consider the problem illustrated in Figure 2.1 in which a plane sheet is oxidized on both sides, since this geometry has been used in several experimental studies [5, 24, 26]. We shall argue later that the methods developed are easily applied to other geometries more representative of practical PWR systems. We assume that the oxide film thickness $h_{\text{ox}}(t)$ and the [spatially uniform] temperature $T(t)$ are known functions of time t, and we wish to predict the evolution of the corresponding stress field.

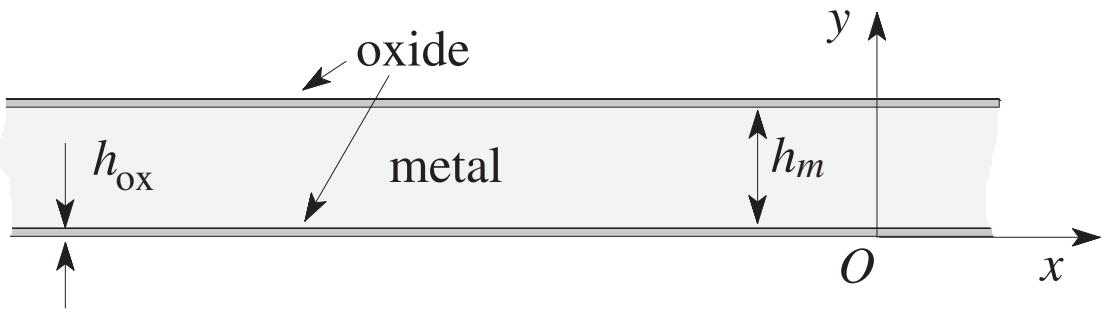

Figure 2.1: Two-sided oxidation of a thin sheet specimen

We define a coordinate system such that the y-axis is perpendicular to the plate surfaces and x and z are in-plane directions. The symmetric geometry implies that no bending occurs and hence the in-plane strains $\epsilon_{xx}(t), \epsilon_{zz}(t)$ are independent of y. The sheet is free to expand in both x and z-directions, so these strain components must be equal and the corresponding

stress state is also biaxial — i.e.

$$\epsilon_{xx} = \epsilon_{zz} \equiv \varepsilon(t) \quad \text{and} \quad \sigma_{xx} = \sigma_{zz} \equiv s(y,t)\ ; \quad \sigma_{yy} = 0 \tag{2.1}$$

which serves to define the in-plane biaxial stress $s(y,t)$ and strain $\varepsilon(t)$. Notice that in the oxide, $s(y,t)$ is a function of both y and t, since different regions of the oxide are generated at different times, whereas in the metal, $s(t)$ is a function of t only.

Since no forces are applied to the sheet, the mean value of $s(y,t)$ across the thickness must be zero for all t — i.e.

$$\int_0^h s(y,t)dy = 0\ , \quad \text{where} \quad h = h_{\rm m} + 2h_{\rm ox} \tag{2.2}$$

This equilibrium condition and the constitutive laws for the materials [i.e. the relations between stress, strain and temperature] are sufficient to determine $s(y,t)$ for given $h_{\rm ox}(t), T(t)$.

2.3 Material behaviour

Strain components in both metal and oxide can be anticipated due to (1) elastic deformation, (2) thermal strain, and (3) inelastic deformation, notably creep. We shall consider each of these contributions separately and draw on published experimental data to decide on appropriate functional forms and material properties. The properties of the metal substrate are generally well-documented, though creep mechanisms can be quite complex [27]. By contrast, oxide properties are complicated by the fact that the oxide involves a mixture of two phases, both of which are anisotropic.

2.3.1 Elastic deformation

For Zircaloy-4, Polatidis *et al.* [5] quote the values $E_{\rm m} = 96$ GPa, $\nu_{\rm m} = 0.34$, where E, ν are respectively Young's modulus and Poisson's ratio. Since elastic properties for alloys are relatively insensitive to small changes in composition, we shall also use these values for

ZIRLO. For the oxide the same authors give the values $E_{\mathrm{ox}} = 253$ GPa, $\nu_{\mathrm{ox}} = 0.282$.

2.3.2 Thermal strain

Guerain *et al.* [28] give the value $\alpha_{\mathrm{m}} = 5.8 \times 10^{-6}$ K^{-1} for the thermal expansion coefficient of the substrate.

For monoclinic zirconia, the thermal expansion coefficient varies between 1.2×10^{-6} K^{-1} and 12.6×10^{-6} K^{-1}, depending on the crystal orientation [6], so the degree of uncertainty introduced by these factors is quite large. However, these authors report XRD studies for a sheet specimen oxidized as in Figure 2.1, after which the temperature was cycled between $T = 743$ K and $T = 293$ K. Under these conditions, the equilibrium condition (Equation (2.2)) and strain compatibility imply that the in-plane stress in the oxide should change by

$$\Delta s_{\mathrm{ox}} = (\alpha_{\mathrm{m}} - \alpha_{\mathrm{ox}})\,\Delta T \Bigg/ \left[\frac{(1-\nu_{\mathrm{ox}})}{E_{\mathrm{ox}}} + \frac{2h_{\mathrm{ox}}}{h_{\mathrm{m}}}\frac{(1-\nu_{\mathrm{m}})}{E_{\mathrm{m}}}\right] \tag{2.3}$$

where ΔT is the change in temperature. Using this result and elastic properties from "Elastic deformation" Section, the XRD data from [6] imply a thermal expansion coefficient $\alpha_{\mathrm{ox}} = 5 \times 10^{-6}$ K^{-1}. However, in view of the uncertainty of oxide composition and orientation, we here use values in the range $\alpha_{\mathrm{ox}} = 5 \pm 2 \times 10^{-6}$ K^{-1}.

2.3.3 Substrate creep

Wang *et al.* [27] developed a deformation-mechanism map for creep of Zircaloy-4, based on a comprehensive survey of published experimental data. For temperatures and stress levels in typical PWR applications, the dominant mechanisms are diffusional creep and power-law creep.

The power-law creep mechanism exhibits a relationship between the von Mises effective normal stress, σ_{eq}, and the effective normal strain rate $\dot{\epsilon}_{\mathrm{eq}}$ of the form [27]

$$\dot{\epsilon}_{\mathrm{eq}} = \frac{AG}{T}\exp\left(-\frac{Q_p}{RT}\right)\left(\frac{\sigma_{\mathrm{eq}}}{G}\right)^{5.1} \tag{2.4}$$

where $Q_p = 285 \pm 20$ kJ/mol is the activation energy, T is the absolute temperature, R is the molar gas constant, and the shear modulus $G = (39400 - 13.4T)$ MPa. Wang *et al.* [27] estimate the constant A as 2.1×10^{24} K MPa^{-1} s^{-1}, based on a wide range of experimental studies, though outliers in this data correspond to values with upper and lower bounds 5.2×10^{24} K MPa^{-1} s^{-1} and 7×10^{23} K MPa^{-1} s^{-1} respectively. Because of the 5.1 power, the predicted stresses are rather weak functions of A, so variation within this range has comparatively little effect on the results.

Diffusional creep is generally assumed to follow a linear relation [29]

$$\dot{\epsilon}_{\mathrm{eq}} = \frac{B\sigma_{\mathrm{eq}}}{T} \exp\left(-\frac{Q_d}{RT}\right) \tag{2.5}$$

Data for diffusional creep parameters for Zr-4 is sparse, but using experimental data from Kaddour *et al.* [30] [based on specimens with an average grain dimension of 8 μm] and $Q_d = 190$ kJ/mol [30], the constant B can be estimated as $B = 1.76 \times 10^6$ K MPa^{-1} s^{-1}.

The strain-rate tensor is related to $\dot{\epsilon}_{\mathrm{eq}}$ by

$$\dot{\epsilon}_{ij} = \frac{3\sigma'_{ij}}{2\sigma_{\mathrm{eq}}} \dot{\epsilon}_{\mathrm{eq}} \tag{2.6}$$

where $\sigma'_{ij} = \sigma_{ij} - \sigma_{kk}/3$ is the deviatoric component of the stress tensor. For the particular case of in-plane biaxial stress $\sigma_{xx} = \sigma_{zz} = s$, $\sigma_{\mathrm{eq}} = |s|$ and the in-plane creep strain rate is

$$\dot{\varepsilon} = \frac{3}{2|s|}\left(s - \frac{2s}{3}\right)\dot{\epsilon}_{\mathrm{eq}} = \mathrm{sgn}(s)\frac{\dot{\epsilon}_{\mathrm{eq}}}{2} \tag{2.7}$$

where $\mathrm{sgn}(s) = s/|s|$ is the signum function, equal to $+1$ if $s > 0$ and -1 if $s < 0$.

2.3.4 Oxide creep

We are not aware of published creep data for the oxide formed on Zircaloy, so we here assume that this can reasonably be approximated by data for other forms of zirconia [29].

In particular, we note that diffusional creep will be of negligible significance compared with other creep mechanisms at the compressive stresses typically exhibited in the oxide layer [31].

Platt *et al.* [24] assumed the Coble-creep law proposed by Choksi *et al.* [31] for stabilized-tetragonal zirconia, and showed that this mechanism had negligible impact on the oxide stresses. However, the possibility of other creep mechanisms was not considered. In particular, it should be noted that the high compressive stresses that occur in an oxide film suppress brittle fracture. This permits deformation mechanisms associated with dislocation motion to occur, such as dislocation glide and power-law creep. Indeed, experimental studies [32] have indicated that such plastic deformation occurs both in the oxide films formed on zirconium alloys and in pure monoclinic zirconia.

Based on these arguments, we assume that deformation occurs by dislocation glide, for which we use the generic model

$$\dot{\epsilon}_{\mathrm{eq}} = \dot{\epsilon}_0 \exp\left[-\frac{Q_g}{RT}\left(1 - \frac{\sigma_{\mathrm{eq}}}{\sigma_g}\right)\right] \tag{2.8}$$

[29]. In this equation, the yield strength at 0 K is taken to be $\sigma_g = 7800$ MPa, and the activation energy is $Q_g = 173.5$ kJ/mol, as reported for lattice-resistance-controlled dislocation-glide in yttria-stabilized cubic zirconia by Baufeld *et al.* [33]. We shall estimate the pre-exponential coefficient $\dot{\epsilon}_0$ in Section "Estimation of $\dot{\epsilon}_0$" below, using oxide strain measurements at 633 K from Polatidis *et al.* [5], but first we need to discuss the stress state under which the oxide is formed.

2.3.5 Oxide growth strains

Zirconium oxide has a higher molar volume than zirconium, so a biaxial compressive stress is developed in the oxide film owing to the constraint exerted by the substrate while the oxide forms. The Pilling-Bedworth ratio, V_{PB}, defined as the ratio of the molar volume of

the oxide to the molar volume of the metal. Calculation of this ratio for zirconium oxidation is outlined in the next section.

2.3.5.1 Calculation of the Pilling-Bedworth ratio

Pilling-Bedworth ratio for oxidation is given as

$$V_{PB} = \frac{V_o}{V_m} \tag{2.9}$$

where V_o and V_m is the molar volume of the oxide and the metal respectively. Molar volume of a chemical species can be calculated as follows

$$V = \frac{N_A V_{cell}}{Z} \tag{2.10}$$

where Z is the number of formula units in the unit cell, N_A is the Avogadro's constant and V_{cell} is the volume of a single unit cell. Zirconium has HPC lattice structure with unit cell dimensions of $a = 0.323$ nm, $c = 0.515$ nm. Volume of a unit cell can then be obtained as

$$V_{Zr_{cell}} = \frac{3\sqrt{3}a^2c}{2} = 0.1396 \text{ nm}^3 \tag{2.11}$$

As there are 6 atoms per unit cell, molar volume is estimated to be

$$V_{Zr} = 14.01 \text{ cm}^3/\text{mol} \tag{2.12}$$

For monoclinic ZrO_2, lattice parameters are $a = 0.5184$ nm, $b = 0.5207$ nm, $c = 0.537$ nm, $\beta = 98.8^o$ and it has 12 atoms or 4 formula units in a unit cell. Therefore, we obtain

$$V_{ZrO_{2cell}} = abc\sin(\beta) = 0.1432 \text{ nm}^3 \tag{2.13}$$

$$V_{ZrO_2} = 21.83 \text{ cm}^3/\text{mol} \tag{2.14}$$

Pilling-Bedworth ratio for zr to monoclinic zirconia is given by

$$V_{PB} = \frac{V_{ZrO_2}}{V_{Zr}} = \frac{21.83}{14.01} = 1.56 \tag{2.15}$$

For tetragonal ZrO_2, lattice parameters are $a = b = 0.5141$ nm, $c = 0.52609$ nm, $\beta = 90^o$ and it has 12 atoms or 4 formula units in a unit cell.

$$V_{ZrO_{2_{cell}}} = abc = 0.139 \text{ nm}^3 \tag{2.16}$$

$$V_{ZrO2} = 20.93 \text{ cm}^3/\text{ mol} \tag{2.17}$$

The volumetric expansion from tetragonal to monoclinic is approximately 3 percent.

2.3.5.2 Growth strains and stresses

If the volumetric expansion during unrestrained growth is assumed to be isotropic, the resulting compressive strain within the oxide would be given by $((V_{PB})^{1/3} - 1) = 0.16$, implying in-plane compressive stresses within the oxide of around 57 GPa. It can be seen that substitution of such stress levels into Equation (2.8) results in huge plastic strain rates, implying a very rapid relaxation of stresses to more reasonable levels. Previous studies [24, 34] have assumed that the oxide forms at an in-plane compressive stress of about 2 GPa, but stresses as high as 4 GPa have been measured experimentally [4, 35], suggesting that the value 2 GPa is merely an arbitrary temporal point for a rapidly relaxing compressive stress. However, the precise details of how the stresses relax from the theoretical initial value is beyond the scope of this work.

2.4 Calculation of stresses

Superposing strains from the various mechanisms discussed in Section "Material behaviour", we obtain the in-plane strain rates

$$\begin{aligned}\dot{\varepsilon}_{\mathrm{m}}(t) &= \frac{\mathrm{sgn}(s_{\mathrm{m}}(t))}{2T}\left[AG\exp\left(-\frac{Q_p}{RT}\right)\left(\frac{|s_{\mathrm{m}}(t)|}{G}\right)^{5.1} + B\exp\left(-\frac{Q_d}{RT}\right)|s_{\mathrm{m}}(t)|\right] \\ &\quad + \frac{\dot{s}_{\mathrm{m}}(t)(1-\nu_{\mathrm{m}})}{E_{\mathrm{m}}} + \alpha_{\mathrm{m}}\dot{T} \qquad (2.18)\\ \dot{\varepsilon}_{\mathrm{ox}}(t) &= \frac{\mathrm{sgn}(s_{\mathrm{ox}}(y,t))\dot{\epsilon}_0}{2}\exp\left[-\frac{Q_g}{RT}\left(1-\frac{|s_{\mathrm{ox}}(y,t)|}{\sigma_g}\right)\right] \\ &\quad + \frac{\dot{s}_{\mathrm{ox}}(y,t)(1-\nu_{\mathrm{ox}})}{E_{\mathrm{ox}}} + \alpha_{\mathrm{ox}}\dot{T} \qquad (2.19)\end{aligned}$$

Notice that the in-plane strains and the stress in the metal substrate are functions of time only, but the stress in the oxide is a function of both the distance, y from the oxide-air/water interface, and time t, since oxidation at different spatial points starts at different times. The initial condition for newly formed oxide was taken to be a compressive stress of 57 GPa, but because initial creep is very rapid, the results are not sensitive to the precise value chosen.

To complete the problem statement, we use the compatibility condition that the lateral strain rates in the oxide and substrate be equal for all times t [i.e. $\dot{\varepsilon}_{\mathrm{ox}}(t) = \dot{\varepsilon}_{\mathrm{m}}(t) \equiv \dot{\varepsilon}(t)$], and the equilibrium condition (Equation (2.2)).

2.4.1 Estimation of $\dot{\epsilon}_0$

The values for the parameters required in this study were all taken directly from the experimental literature, as described in Section "Material behaviour", except for the pre-exponential coefficient $\dot{\epsilon}_0$ in (Equation (2.8)). To estimate this parameter, we performed a curve fit of the average stress in the oxide layer predicted by the model to *ex situ* measurements of residual stress reported by Polatidis *et al.* [5] for oxidation at a temperature of $T = 633$ K. The oxide growth law $h_{\mathrm{ox}}(t)$ for this case was obtained by fitting a smooth curve to the experimental data reported in [5].

The results are shown in Figure 2.2. The points show the experimental results from [5] and the shaded region defines the bounds of the predictions based on Equations (2.10, 2.11), with $\dot{\epsilon}_0 = 300$ s^{-1} and a thermal expansion coefficient of the oxide (α_{ox}) in the range $5 \pm 2 \times 10^{-6}$ K^{-1}.

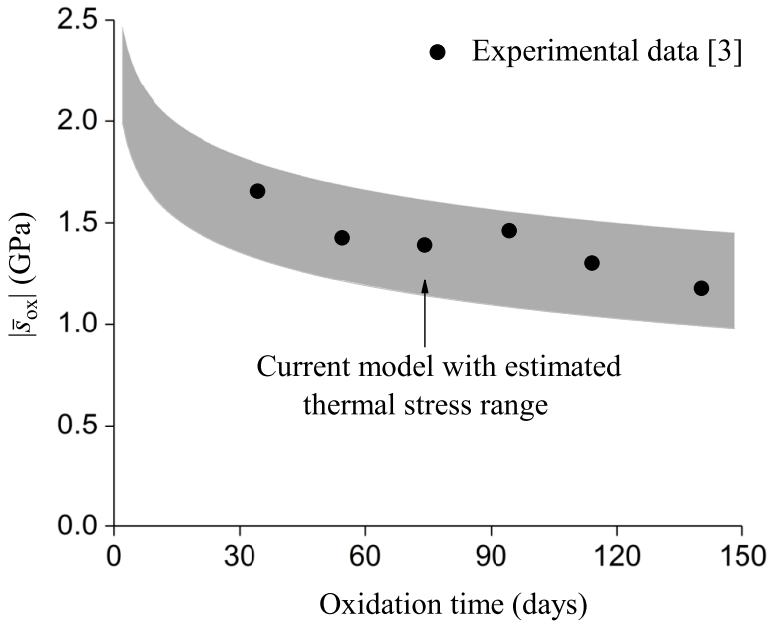

Figure 2.2: Estimation of the pre-exponential coefficient $\dot{\epsilon}_0$ in (Equation (2.8)), based on experimental data for the *ex situ* average in-plane compressive stress $|\bar{s}_{ox}|$ in the oxide [5] at $T = 633$ K. The shaded region represents predicted results for chosen range of oxide's thermal expansion coefficient, $\alpha_{ox} = 5 \pm 2 \times 10^{-6}$ K^{-1}.

The value of $\dot{\epsilon}_0 = 300$ s^{-1} is much lower than that generally quoted in the literature ($\dot{\epsilon}_0 = 10^6$ s^{-1}) for a large set of materials [29]. Such values of $\dot{\epsilon}_0$ could have been achieved if we had chosen a higher value of activation energy ($Q_g \sim 230$ kJ/mol instead of $Q_g = 173.5$ kJ/mol) while fitting our model to the experimental data of oxide stress in Figure 2.2. It is worth noting that Douglass [32] describes experiments showing that the hardness of cubic zirconia is significantly more temperature sensitive than is the monoclinic phase. This suggests that the activation energy for the oxide layer may be higher than that of cubic zirconia, used in this study. It is clear that further progress in understanding oxide stress relaxation at

elevated temperatures is contingent on more direct experimental investigations of the creep behaviour of the oxide.

2.4.1.1 An approximate solution

In many applications, the oxide layer is much thinner than the metal [$h_{\rm ox} \ll h_{\rm m}$], in which case the equilibrium condition (Equation (2.2)) implies that the in-plane stresses in the metal are low, even when those in the oxide are high. If the corresponding contributions to the in-plane strain rate $\dot{\varepsilon}_{\rm m}(t)$ are sufficiently small to be approximated as zero, (Equation 2.10, 2.11) and the compatibility condition then reduce to

$$\begin{aligned} \frac{\mathrm{sgn}(s_{\rm ox}(y,t))\dot{\epsilon}_0}{2} \exp\left[-\frac{Q_g}{RT}\left(1-\frac{|s_{\rm ox}(y,t)|}{\sigma_g}\right)\right] \\ +\frac{\dot{s}_{\rm ox}(y,t)(1-\nu_{\rm ox})}{E_{\rm ox}} + (\alpha_{\rm ox}-\alpha_{\rm m})\dot{T} &= 0 \end{aligned} \tag{2.20}$$

If the temperature T is constant and $s_{\rm ox}$ is always compressive, this equation can be solved in closed form giving

$$\exp\left(\frac{Q_g s_{\rm ox}}{RT\sigma_g}\right) = \exp\left(\frac{Q_g s_0}{RT\sigma_g}\right) + \frac{Q_g E_{\rm ox}\dot{\epsilon}_0\, t}{2RT\sigma_g(1-\nu_{\rm ox})} \exp\left(-\frac{Q_g}{RT}\right) \tag{2.21}$$

where $s_0 = -57$ GPa is the in-plane stress at the instant at which a given layer of oxide was formed, and time t is measured from that instant. Notice that because of the extremely rapid creep at small values of t, the predictions at practical time scales are quite insensitive to the value of s_0.

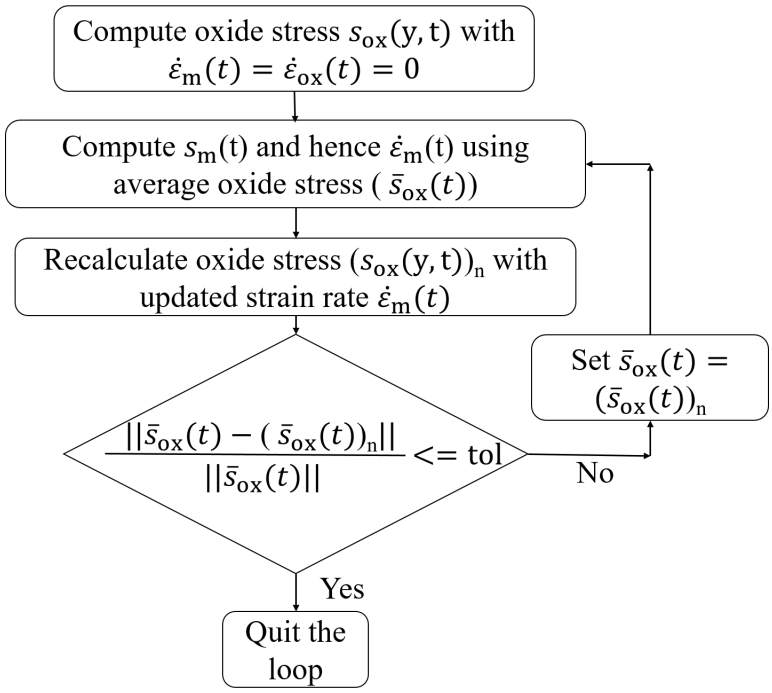

Figure 2.3: An iterative procedure for the simultaneous solution of Equations (2.10, 2.11).

If the strains in the substrate are small but not negligible, the solution of Section 2.4.1.1 can be used as the first step of an iterative procedure. Using the approximation for $s_{ox}(y,t)$ from that equation, we estimate $s_m(t)$ from (Equation (2.2)) and substitute this value into Equation 2.10 to obtain an improved estimate for the strain rate of the substrate, $\dot{\varepsilon}_m(t)$. Repetition of this procedure, as shown in the flowchart of Figure 2.3, allows results to be obtained to any desired degree of accuracy.

2.5 Results

In this section, we shall compare the predictions of the model with experimental results for oxide stresses from two previous studies.

Platt *et al.* [24] used synchrotron X-ray diffraction [S-XRD] to obtain the in-plane stress, s, *in situ* while samples were being oxidized at two different temperatures of 923 K and 983 K. The volume fractions, f_T and f_M, of the tetragonal and monoclinic phases, respectively,

and the corresponding stresses, s_T and s_M, were measured using S-XRD and these values were then used to determine the average oxide stress, defined as

$$s_{\text{ox}} = f_T s_T + f_M s_M \tag{2.22}$$

In these experiments, temperatures were reported to increase from an initial value of 563 K at a rate of $\sim$ 11.2 K/min, until the required temperature was achieved. Thus, conditions for both experiments were nominally identical until t = 32 min, after which the temperature continued to rise in the 983 K case only. The oxide growth law $h_{\text{ox}}(t)$ for each case was determined by interpolating smooth curves through the experimental values from [24], including an initial transient for the initial heating phase, for which no experimental values were reported.

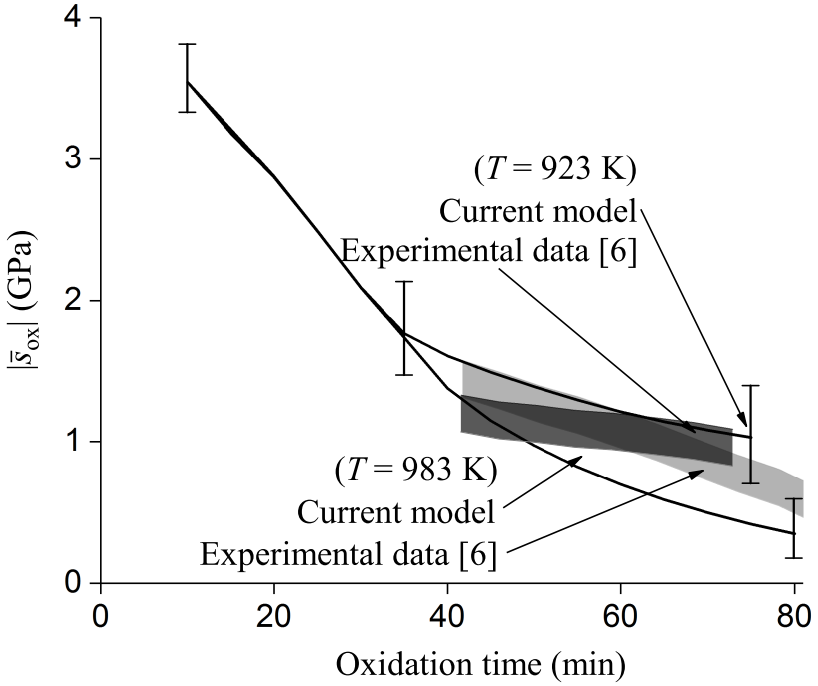

Figure 2.4: Comparison of predictions of average in-plane oxide compressive stress ($|\bar{s}_{\text{ox}}|$) at $T = 923$ K and $T = 983$ K with *in-situ* experimental data from [24]. Error bars show the effect of uncertainty in the model parameters.

Experimental oxide stress values are compared with predictions from the current model in Figure 2.4. Uncertainty in the power-law creep parameters of Zircaloy-4 and glide parameters for the oxide, quantified in previous sections, is represented by error bars in this figure.

Figure 2.4 shows that the model predictions agree well with the experimental data, in view of the range of uncertainty of the model parameters. In particular, the trend [slope] of the predictions is very close to the experimental data, indicating that the assumed creep laws and parameters describe the evolution of the system correctly.

The most significant discrepancy is the overprediction of the 'starting' value of stress at $t = 41$ min for $T = 923$ K. We recall that conditions for both experiments were nominally identical until $t = 32$ min, after which the temperature continued to rise in the 983 K case only. Since creep rate is a strong function of temperature, this suggests that the stresses at 983 K should if anything be lower than those at 923 K, but the opposite was reported in the earlier stages of measurement. We note however that similar experiments in the same study using ZIRLO specimens [24] did not replicate this behaviour. The low intensity of the diffracted X-ray beam from relatively thin oxide layers poses a significant constraint on the accurate measurement of the lattice strains during the early stages of oxidation, so this discrepancy should perhaps not be given undue weight.

2.5.1 Effect of substrate strain

As remarked in Section "An approximate solution", if the oxide layer is sufficiently thin [$h_{\mathrm{ox}} \ll h_{\mathrm{m}}$], a good approximation can be obtained by assuming $\dot{\varepsilon}_{\mathrm{m}} = 0$, which considerably simplifies the calculation. This approximation [dashed lines] is compared with the more precise calculation [solid lines] in Figure 2.5 for the same conditions as in [24] and Figure 2.4. The results show that the approximation of Section "An approximate solution" predicts stresses that are very close to those of the more exact calculation at $T = 923$ K, but that the approximation significantly overestimates the stress at $T = 983$ K.

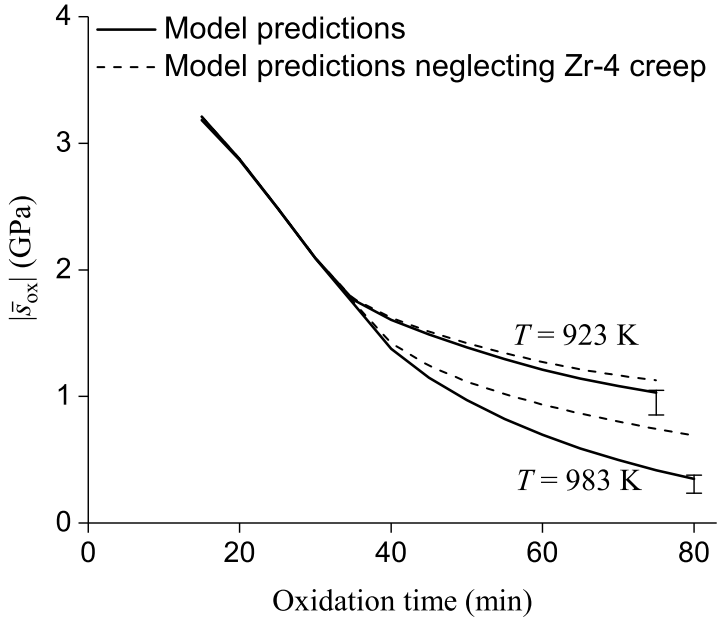

Figure 2.5: Comparison of predictions of the present model including substrate strains [solid line] and neglecting them [dashed line] at temperatures $T = 923$ K and $T = 983$ K. The dashed line is obtained from the approximation of Section "An approximate solution". Error bars represent the uncertainty in Zr-4 creep parameters.

The theoretical model of Platt *et al.* [24] attributes stress relaxation entirely to creep in the metal substrate. However, this leads to plausible predictions of oxide stresses only if (i) the initial stress in the oxide is assumed to be ~ 2 GPa, which is lower than the measured stress magnitudes of Ref. [4, 35] and (ii) the creep rate is assumed to be much more rapid than reported data [36, 37]. Platt *et al.* [24] estimated substrate creep parameters using oxide strain measurements from experiments at $T = 633$ K [5], but our simulations recognizing the role of plastic deformation in the oxide show that creep in the substrate has a negligible effect at this temperature for the entire range of possible power-law creep strain rates of Zr-4. This is consistent with oxidation strain measurements of Ref [36, 37] at $T = 633$ K, which are in a range where only elastic behaviour is to be anticipated in the substrate.

2.5.2 Stress distributions

Preuss *et al.* [26] measured the stresses *ex situ* at various depths within a 78 μm thick oxide layer that was formed on a ZIRLO sheet oxidized at 688 K for 600 days. Even though the stresses were measured only in the monoclinic phase (s_M), reported tetragonal content was less than 5% in the oxide layer, so these results can reasonably be compared with the current numerical model. In the absence of oxide growth data for intermediate points, a linear law (giving $h_{\text{ox}} = 78$ μm at $t = 600$ days) was assumed.

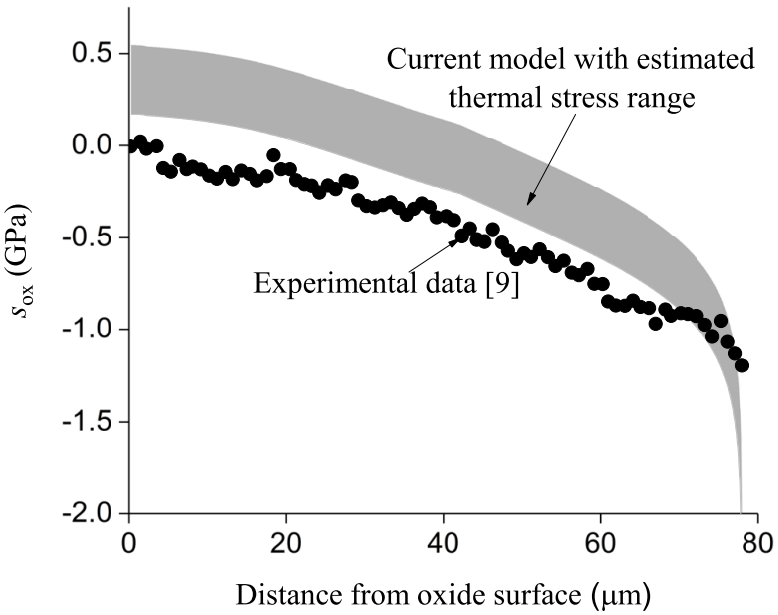

Figure 2.6: Comparison of predictions of in-plane oxide stress (s_{ox}) distribution across its thickness at $T = 688$ K with *ex-situ* experimental data for ZIRLO from [26]. The shaded region represents predicted results for the range $\alpha_{\text{ox}} = 5 \pm 2 \times 10^{-6}$ K^{-1}.

Figure 2.6 compares the predicted stress distribution with the experimental data from [26]. The shaded region defines the bounds of the predictions for α_{ox} in the range $5 \pm 2 \times 10^{-6}$ K^{-1} (see Section "Thermal strain"), and $\dot{\epsilon}_0 = 300$ s^{-1} and nominal values of the creep rates of Zr-4 were assumed, in the absence of suitable data for Zirlo. The predicted range of the *ex situ* oxide stress and the form of the distribution agree well with the experimental results.

2.5.2.1 Evolution of the stress distribution over time

In view of the good agreement in Figure 2.6, we performed additional simulations to track how the oxide stress distribution is predicted to evolve over time. Figure 2.7a shows the evolution of the in-plane compressive stress distribution in the oxide as oxidation proceeds at 633 K, for which we used oxide growth data from [5]. The vertical straight lines represent the location of the metal-oxide interface at that particular instant of time. In each case the oxide is formed at very high compressive stress, but this relaxes rapidly to a value in the range $2 \sim 3$ GPa. Subsequent stress relaxation at any given point is then comparatively slow.

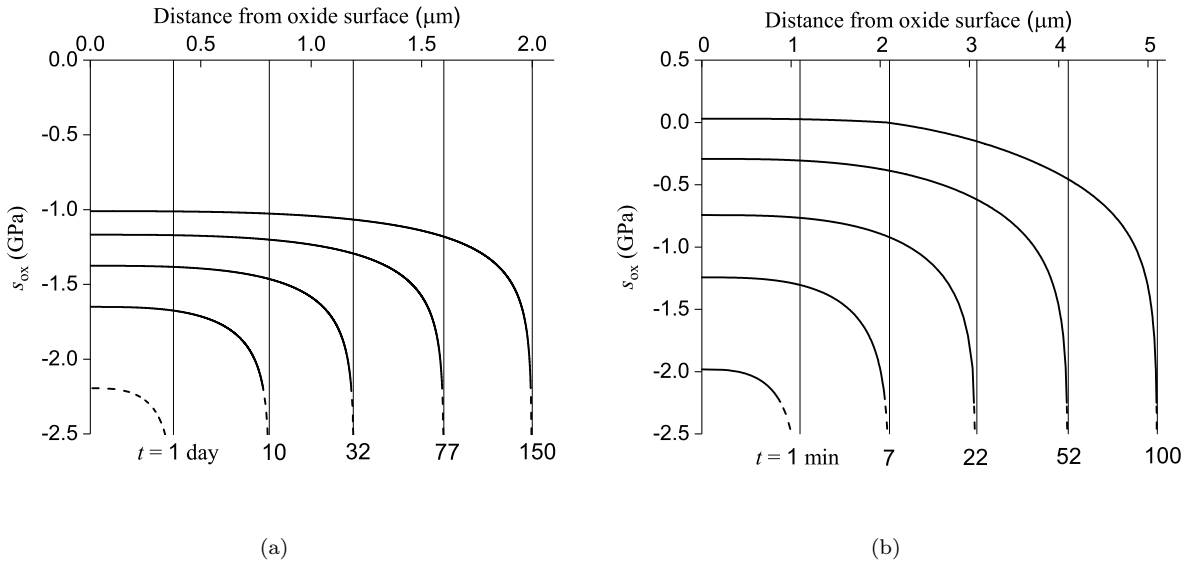

Figure 2.7: Predicted in-plane stress distribution in the oxide layer at various times t for (a) $T = 633$ K , and (b) $T = 973$ K. Vertical lines represent location of the metal-oxide interface at time t.

Figure 2.7(b) shows corresponding stress distributions at a temperature of 973 K, using oxide growth data from [38]. The higher temperature leads to faster rates of stress relaxation, resulting in larger stress gradients across the film. Note that XRD estimates of the average stress across the film may be weighted towards shallower depths in the oxide due to the partial absorption of rays coming from relatively deeper locations. With stress distributions of the form of Figure 2.7, this would lead to an underestimate of the average stress. XRD

penetration depends on tilt angle, incident angle and the respective phase of the oxide [39], but in the absence of such detailed data, the theoretical results discussed in this chapter were all plotted using an unweighted [uniform] average.

Figure 2.7 also shows that the stresses remain predominantly compressive up to the oxide-water interface for oxidation of 150 days at $T = 633$ K and 100 minutes at $T = 973$ K. These are approximately the times at which a transition in the oxidation kinetics is reported to occur at these temperatures [1, 5, 38]. Hence, there seems to be no possibility of formation of through-thickness vertical cracks that could provide a barrier-free path for oxidizing species to diffuse to the metal-oxide interface. This result is consistent with the SEM observations by Nakamura *et al.* [40], which show that no vertical cracks exist in the oxide film either before or immediately after the observed transition in the oxidation kinetics at $T = 773$ K.

2.6 Other geometries

The discussion so far has mainly centered around the symmetric plate geometry of Figure 2.1, but the constitutive behaviour for metal and oxide outlined in Section 2.3 could in principle be applied to any geometry, using a finite element implementation. Also, the solution of Section "An approximate solution" can be used in any situation where the oxide film thickness is sufficiently small compared with any other linear dimensions of the body.

The cladding tube used in PWRs is 570 μm thick and has a mean radius of 4.4 mm. It can therefore reasonably be treated as a thin-walled tube, implying (i) that hoop stresses will be approximately uniform through the substrate thickness, and (ii) that the mean hoop stress across substrate and oxide will be much larger than the pressures applied on the curved surfaces. Thus, conditions approximate quite closely to those in Figure 2.1 and based on Figure 2.5, (Equation (2.21)) provides a very convenient and quick estimate for the stress field provided the temperature is not too high.

2.7 Conclusions

In this chapter, we have developed a stress evolution model for the oxide layers formed on zirconium alloys. Dislocation glide in the oxide layer and power-law creep in the substrate are proposed as the most significant deformation mechanisms for the temperature range of $T = 600 - 1000$ K. Our thesis is that the oxide deforms primarily by dislocation glide for $T < 900$ K, while creep of the substrate only becomes significant at higher temperatures. This result is also consistent with the oxidation strain data reported in the literature [36, 37], which indicates that the substrate behaves elastically at $T = 633$ K.

All the model parameters were taken from the literature except the glide parameters (Q_g, σ_g), which were assumed to be the same as for for yttria-stabilized cubic zirconia. We used experimental data for *ex situ* oxide stresses to curve-fit for the pre-exponential glide constant, $\dot{\epsilon}_0$. Direct experimental investigations of creep parameters for monoclinic and tetragonal zirconia are needed to validate applicability of these parameters to the oxide film as well, as to predict the stresses for $T > 1000$ K.

If the oxide film thickness is small compared with that of the substrate, a simple approximation to the stress field can be quickly obtained by assuming the in-plane strain rate to be zero.

Chapter 3

Energetic Analysis of Constrained Tetragonal-to-Monoclinic Phase Transformation in Polycrystalline Zirconia Films

3.1 Introduction

The monoclinic phase of zirconia is thermodynamically stable at temperatures below 1400 K, above which the tetragonal phase is stable up to 2600 K, when the cubic phase becomes stable. However, in the oxide layers formed on zirconium alloys, the tetragonal phase is observed at temperatures that are well below 1000 K. In-plane compressive stress in the oxide film, and small grain size at the metal-oxide interface have been considered as the dominant contributing factors favoring the high-density tetragonal phase at such temperatures [25, 41]. This metastable tetragonal phase formed in polycrystalline oxide films is observed to undergo a transformation to the monoclinic phase as oxidation proceeds [5, 24, 7]. Some experimental studies [6, 5] show a smooth curve of the average fraction of the tetragonal phase in the oxide layer dropping over time throughout the oxidation process, while few others [8, 9] indicate a sudden increase in this drop rate near a transition in the oxidation kinetics. It should be noted that all the above mentioned studies use XRD technique, and measurements are carried out ex-situ except in [6] which is in-situ XRD in oxygen environment. Trends observed in the spatial distribution of the tetragonal phase across the oxide film also shows variability across different studies. Most of the XRD-studies [6, 26, 42] show a continuous decrease in tetragonal fraction from the metal-oxide interface to the oxide-water interface. However,

synchrotron X-ray diffraction (SXRD) study by Yilmazbayhan *et al.* [3] indicates a spatial periodicity in the variation of t-fraction (which is more prominent is Zirlo than Zy-4), with a period that is approximately the same as the transition thickness. However, the average tetragonal percentage content shows a drop away from the metal-oxide interface in this study as well. As SXRD technique provides better resolution, signal-to-noise ratio, and texture correction capabilities as compared to conventional XRD, we are inclined to assign more significance to the SXRD data for the purpose of this thesis.

Transformation of the tetragonal phase to the monoclinic phase has been proposed as a possible mechanism of reduced protectiveness in the oxide, in view of its ability to cause micro-cracks [10]. These defects are suggested to form due to the anisotropic nature of the expansion eigen-strains associated with this phase change (see Section 3.1.1 below). Therefore, a large body of experimental evidence has been developed to understand this phenomenon, as outlined in the first paragraph of this chapter [6, 24, 26, 42]. However, drawing general conclusions about the energetics of this phase transformation has remained a challenge due to an insufficient, physics-based, quantitative understanding of the process.

Since a mathematical understanding of the tetragonal-to-monoclinic phase transformation of the oxide is crucial in understanding the oxidation behavior of Zircaloys, in this chapter, we present a continuum-based analysis of a grain in the tetragonal phase transforming to the monoclinic phase in a matrix of the oxide film. We also present a supplementary atomistic analysis to analyze the effect of various crystal defects on the relative thermodynamic stability of the two phases.

3.1.1 Crystallography of tetragonal and monoclinic zirconia

Figure 3.1 shows a schematic of the tetragonal and the monoclinic lattice structures. In tetragonal crystal structure, two of the crystal axes are equal in length and all of the three axis are perpendicular to each other. In the lower-symmetry monoclinic crystal structure, all of the crystal axes are of different length ($a \neq b \neq c$) and only two of them are orthogonal

to each other ($\beta > 90^o$).

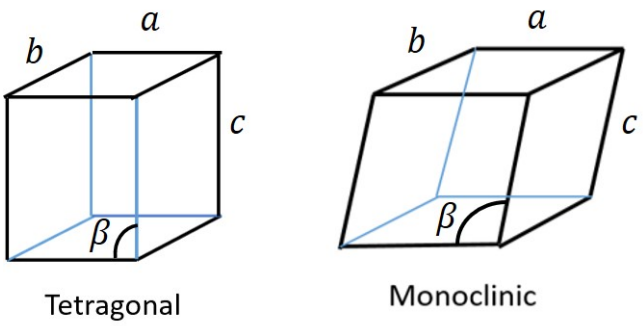

Figure 3.1: Crystal structures of the tetragonal and the monoclinic phases.

For the particular case of zirconium oxide (zirconia), the crystal parameters of Figure 3.1 are given in Table 3.1 [22]

Crystal parameter	a [Å]	b [Å]	c [Å]	β
Tetragonal	5.141	5.141	5.261	90^o
Monoclinic	5.184	5.207	5.37	98.8^o

Table 3.1: Crystal structure parameters for tetrgonal and monoclinic zirconia

Calculation of transformation eigen-trains

The eigen-strain for the phase transformation depends on the particular transformation variant considered [22]. For the purpose of this study, we consider the variant $(a_t, b_t, c_t) \rightarrow (a_m, b_m, c_m)$, chosen as to minimize the strain energy barrier during the transformation [43]. For this variant, crystal axis a of the tetragonal phase (a_t) transforms to the crystal axis a of the monoclinic phase (a_m), crystal axis b_t transforms to the crystal axis b_m and so on. Note that the variant $(a_t, b_t, c_t) \rightarrow (b_m, a_m, c_m)$ will also have the same strain energy barrier as $a_t = b_t$. Also, each variant has its self-accommodating variant (or twin) which is its mirror image.

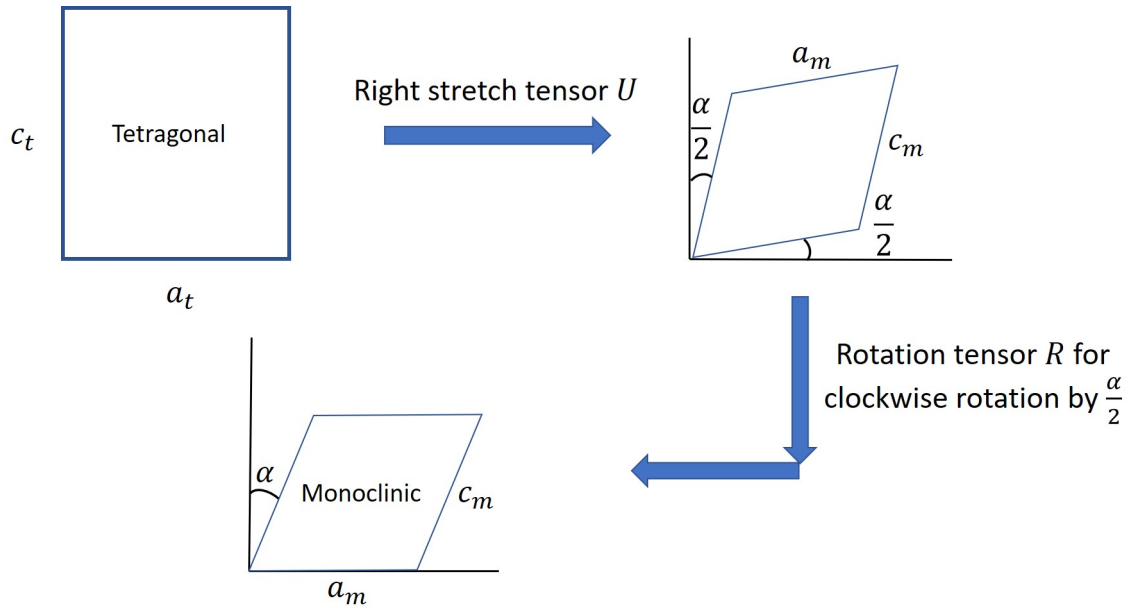

Figure 3.2: 2D representation of the deformation required for the tetragonal-to-monoclinic phase transformation, in the plane containing crystal axes a and c.

Figure 3.2 represents this variant formation in a plane containing crystal axes a and c. The deformation gradient F can be decomposed into a stretch tensor U and a rotation tensor R and can be written as

$$F = RU$$

Assuming x-direction along crystal axis a, y-direction along crystal axis c, we can write the rotation matrix R of Figure 3.2 as

$$R = \begin{bmatrix} \cos(\frac{\alpha}{2}) & \sin(\frac{\alpha}{2}) & 0 \\ -\sin(\frac{\alpha}{2}) & \cos(\frac{\alpha}{2}) & 0 \\ 0 & 0 & 1 \end{bmatrix}$$

where $\alpha = \beta - 90^{\circ}$. We can write the deformation gradient tensor as

$$F = \begin{bmatrix} \frac{a_m}{at} & \frac{c_m \sin(\alpha)}{c_t} & 0 \\ 0 & \frac{c_m \cos(\alpha)}{c_t} & 0 \\ 0 & 0 & \frac{b_m}{b_t} \end{bmatrix}$$

Using the crystal parameters of Table 3.1 and the relation $F = RU$, we can find the right stretch tensor U. Using a small strain approximation $\epsilon = U - I$, we obtain the transformation strain as

$$\epsilon^{T-M1} = \begin{bmatrix} 0.0054 & 0.07785 & 0 \\ 0.07785 & 0.0177 & 0 \\ 0 & 0 & 0.01284 \end{bmatrix}$$

where M1 refers to the first monoclinic variant. It should be noted that for negative shear strains, we get another variant of the monoclinic phase.

$$\epsilon^{T-M2} = \begin{bmatrix} 0.0054 & -0.07785 & 0 \\ -0.07785 & 0.0177 & 0 \\ 0 & 0 & 0.01284 \end{bmatrix}$$

which implies an engineering shear strain of $\sim 16\%$ (or $2\epsilon_{12}$), and an anisotropic volume expansion of 3.6% calculated as follows

$$\frac{\Delta V}{V} \times 100 = \{[(1+\epsilon_{11}) \times (1+\epsilon_{22}) \times (1+\epsilon_{33})] - 1\} \times 100 = 3.6\% \tag{3.1}$$

3.2 Free-energy continuum framework

Tetragonal-to-monoclinic phase change is generally assumed to be martensitic in nature. Energetics of a martensitic transformation can be analyzed using a free-energy criterion. A decrease in the free energy indicates favorability of the phase transformation. As this transformation is associated with $\approx 16\%$ engineering shear strain, and an anisotropic volume change of $\approx 3\%$ (refer Section 3.1.1), there is a strain energy barrier for a tetragonal oxide grain to transform to the monoclinic phase, as it is constrained by the surrounding oxide (matrix). Therefore, twinning is observed in polycrystalline oxide films [44] that helps to reduce this energy barrier by reducing the macroscopic shear strains.

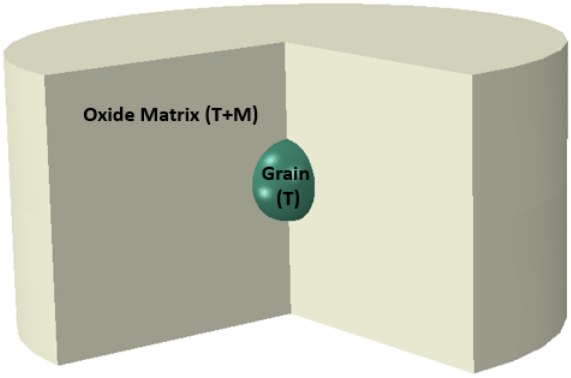

Figure 3.3: Geometric representation of the system analyzed in this phase transformation study, considering a tetragonal oxide grain transforming in homogeneous oxide.

In this study, we present a 3-dimensional analysis of a tetragonal grain transforming in a homogeneous and isotropic mixture of the tetragonal and monoclinic phases of zirconia Figure 3.3, in the temperature range of 600 K$< T <$ 1000 K. At these temperatures, tetragonal phase is meta-stabilized in the oxide films while the monoclinic is the thermodynamically stable phase. Free energy change during the process can then be expressed as

$$\Delta G_{T\rightarrow M} = -|\Delta G_{ch}| + \Delta U + \Delta G_{gb} + G_{tw} \tag{3.2}$$

$\Delta G_{T\rightarrow M}$ is the total change in the free energy per unit volume of the grain during the phase transformation, and its value should be negative in order for it to be favorable. $|\Delta G_{ch}|$ is the absolute change in the chemical free energy per unit volume (or the thermodynamic driving force). A negative sign preceding it implies that it reduces the overall change in free energy (i.e the monoclinic phase is thermodynamically favored at temperatures considered in this study). ΔU is the strain energy barrier per unit volume of the transforming grain for the transformation, corresponding to the eigen-strain obtained in Section 3.1.1. ΔG_{gb} is the contribution from the change in the grain boundary energy and G_{tw} is that from the formation of twin boundaries. Equation (3.2) can also be written as follows,

$$\Delta G_{T\to M} = -|\Delta G_{ch}| + \Delta U + \frac{\Delta\gamma_{gb}A_{gb}}{V_{grain}} + \frac{\gamma_{tw}A_{tw}}{V_{grain}} \tag{3.3}$$

where $\Delta\gamma_{gb}$ is the change in grain boundary energy per unit area during transformation and γ_{tw} is the twin boundary energy per unit area. A_{gb} and A_{tw} are grain boundary area and twin boundary area respectively. V_{grain} is the volume of the grain undergoing transformation.

From Equation (3.3), we note that the only term favoring transformation to the monoclinic phase is the chemical free energy term ΔG_{ch}. Therefore, its value should be large enough to overcome the strain and the surface energy barrier contributions obtained from the rest of the three terms in the equation.

3.2.1 Calculation of free-energy change ($\Delta G_{T\to M}$)

In this section, we will provide details of the finite element simulations, and published experimental data used to estimate each term in the free energy-criterion of Equation (3.3).

3.2.1.1 Strain energy barrier (ΔU)

Strain energy barrier is computed using 3D finite-element simulations with a geometry as shown in Figure 3.3 of a tetragonal grain transforming in a matrix of homogeneous oxide in ABAQUS. Transformation eigen-strains of Section 3.1.1 are applied as pseudo-thermal strains on the grain. Elastic properties of both the phases as well as the matrix is taken as $E = 200$ GPa, $\nu = 0.3$. In the following sections, we discuss various factors which affect the model geometry and input parameters.

3.2.1.2 Grain Morphology

The grain structure of the oxide layer formed on Zircaloy-4 at $T = 633$ K is fairly well known to be periodic, with a wavelength that is approximately equal to the transition thickness. Figure 3.4 shows the schematic of this grain structure. We define one oxidation cycle as the time period between two transitions in the oxidation kinetics. First oxidation

Grain type	Grain shape	Dimensions (nm $\times$ nm $\times$ nm)
Equiaxed grain	Ellipsoidal grain	$15 \times 15 \times 16$
Columnar grain	Hexagonal cross-section column	$40 \times 40 \times 200$

Table 3.2: Grain shapes and sizes analyzed in this study

cycle is from the beginning of the oxidation process up to the first transition. Equiaxed grains of diameter ≈ 30 nm are developed during the initial stages of each oxidation cycle (because of the higher oxidation rate), and larger columnar grains (diameter of $30 \sim 40$ nm, length of $100 \sim 200$ nm) during the later stages, possibly because of the in-plane compression in the oxide. Columnar grains at the metal-oxide interface appear to be longer than the ones formed previously during that cycle (as the oxidation rate slows down).

Equiaxed grains which form the outermost part of the oxide, as well as the columnar grains, are observed to undergo transformation [7]. In this study, we choose two representative grain types for analysis, outlined in Table 3.2. The selected cases correspond to the smallest equiaxed grain and the longest columnar grain observed in the oxide layer, and they present the two extremes of the least and the maximum energy barriers for the phase transformation respectively. We provide explanations for this in the next section.

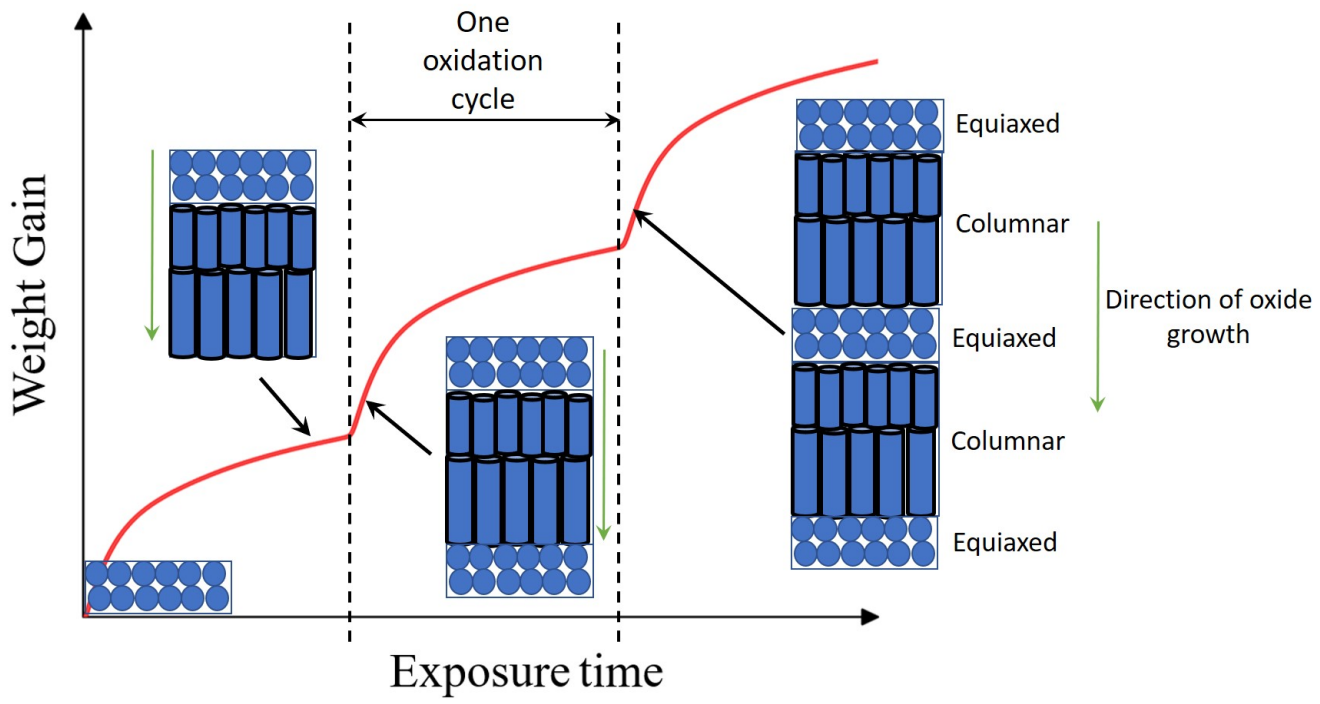

Figure 3.4: Schematic of the grain structure in the oxide film formed on zirconium alloys. Arrows indicate the oxidation stage at which that particular grain structure is observed.

Grain size data for temperatures above standard PWR operating temperatures could not be obtained from the literature. Increased oxidation rate at high temperatures should result in smaller grain size. However, higher temperatures also result in higher rate of grain growth. Therefore, no definite conclusion can be made even about the trend of grain sizes with temperature. In this study, therefore, we assume grain morphology to be the same for temperatures up to 1000 K.

Previous analytical calculation of energy barrier [45] is only valid for equiaxed grains and cannot capture the interaction of biaxial stress state with anisotropic volume expansion during the transformation.

3.2.1.3 Oxide texture

Tetragonal grains are observed to have a texture in oxide layers, where crystal axis c aligns with the direction of the oxide growth [44]. Note that crystal data of Table 3.1 indicates that

this orientation will provide the least area in the plane parallel to the metal-oxide interface. Therefore, it will minimize the strain energy in these oxide layers, which are under in-plane compression, and hence forms the preferred orientation. Other crystal directions (a and b) are observed to be randomly distributed in the two in-plane directions. Recall that this phase transformation is associated with a shear eigen-strain in the plane containing crystal axes a and c. Furthermore, for a particular transformation variant, there are two possible orientations with the same eigen-strain. Therefore, based on the observed texture, there are two possible transformation configurations for the variant described in Section 3.1.1, as shown in Figure 3.5. In case (a), crystal axis c of the transformed monoclinic phase remains parallel to the untransformed tetragonal phase, i.e $[001]_t//[001]_m$. For case (b), crystal axes a of both the phases remains parallel to each other $[100]_t//[100]_m$. However, from a mechanics point of view, we can say that with the given direction of the in-plane compression shown in the figure, configuration (a) will offer lower strain energy barrier and hence will be preferred over (b). Therefore, we perform finite element simulations only for case (a).

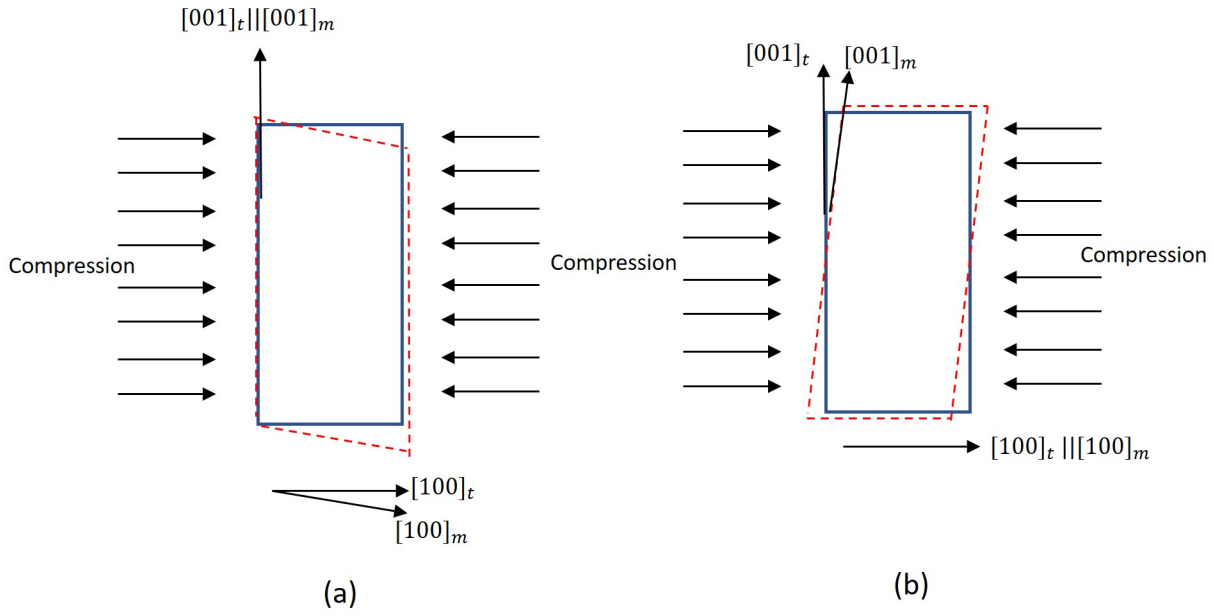

Figure 3.5: Two possible configurations for phase transformation in a plane perpendicular to the metal-oxide interface.

Transformation eigen-strain as well as the cross-section is anisotropic in the two in-

plane directions, therefore different orientations may have different strain energy barriers associated with it. While for equiaxed grain the strain energy barrier for each of these random distributions is the same due to symmetry, columnar grains with hexagonal cross-section exhibit a variation of energy barrier with respect to angle θ of Figure 3.6 that is periodic (with a period of 60°). Therefore, we need to analyze only the orientations between $0^o < \theta < 30^o$ to understand the complete picture.

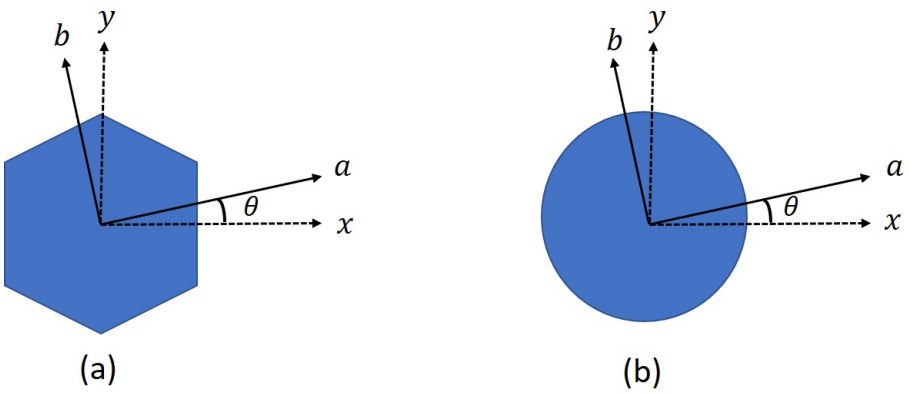

Figure 3.6: Crystal orientation in a plane parallel to the metal-oxide interface for (a) a hexagonal grain and (b) an equiaxed grain. Hexagonal grain shows a 60° symmetry with respect to the grain geometry while the equiaxed grain shows a 180° symmetry.

In the next section, we will describe how we select the optimum orientation from twinning-based simulations.

3.2.1.4 Optimized twinned structure

Twinning plays a crucial role in lowering the strain energy barriers by reducing the macroscopic deformation caused by shear eigen-strain. We model twinning by applying alternating nature of shear strains in adjacent twin bands perpendicular to the crystal axis a using USDFLD subroutine in ABAQUS. Twin density is number of alternating variant bands in one grain. Note that free energy $\Delta G_{T\rightarrow M}$ constitutes twin boundary energy as well as a strain energy contribution. While the former increases with increasing twin density, the latter drops because of decrease in macroscopic shear. Therefore, there exists an optimum

value of twin density that minimizes the free energy barrier for the transformation. This calculation for an equiaxed grain is shown in Figure 3.7 giving an optimum twin density of 4 or 6.

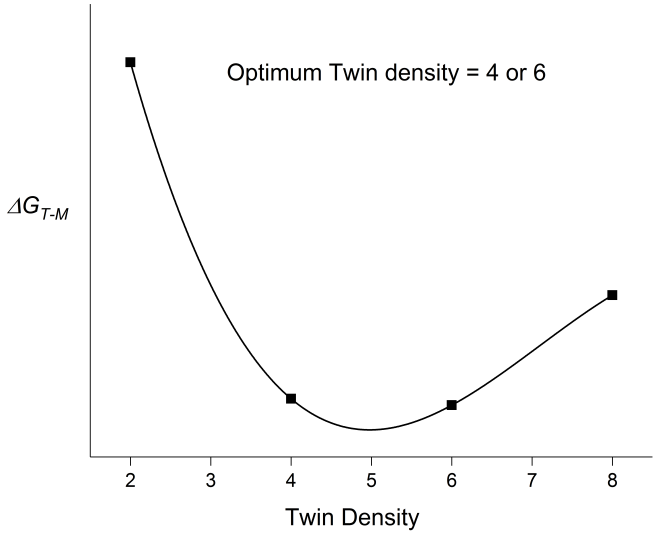

Figure 3.7: Variation of free energy with twin density for an equiaxed grain.

A similar calculation for columnar grains gave an optimum twin density of 6. As discussed in the previous section, the effect of crystal orientation was studied by analysing varying orientations of twin planes (normal to crystal axes a) with respect to any one of the longitudinal surface of the hexagonal grain, i.e cases corresponding to $0^o < \theta < 30^o$ (refer Figure 3.6 for the description of angle θ). Figure 3.8 shows the contours of shear strain obtained by the finite element simulations of the two limiting scenarios. Regions of positive shear (red/orange) are separated by the ones in negative shear (blue/green) by twin boundaries. In case (a), twin boundaries are parallel to the right face of the grain ($\theta = 0^o$), and in case (b), twin boundaries make an angle of $\theta = 30^o$ with the right face of the hexagonal grain. By analyzing various orientations between these two scenarios ($0^o < \theta < 30^o$ in Figure 3.6), we find orientation (a) to offer the minimum energy barrier, and orientation (b) to offer the maximum energy barrier against the phase transformation. We will only present the results

of case (a) in further analysis.

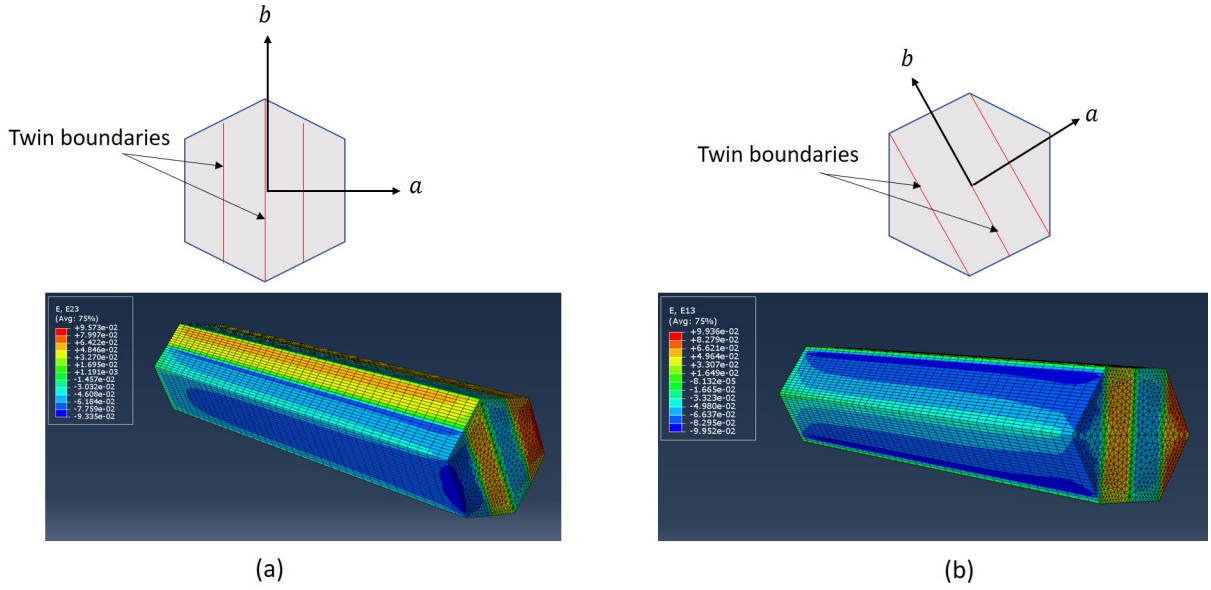

Figure 3.8: Finite element simulation of two specific orientations of the hexagonal grain. Case (a) is for $\theta = 0^{o}$ and case (b) is for $\theta = 30^{o}$. Refer Figure 3.6(a) for the description of angle θ.

3.2.1.5 Grain-matrix interface conditions

Garvie *et al.* [46] suggested that loss in coherency or cracking may increase the favorability of this transformation, by reducing the strain energy barrier associated with the shear component of the eigen-strain. As the oxide layer is in compression in the two in-plane directions and stress-free in the third (see chapter 2), we assume that macroscopic cracks cannot form within the oxide. Therefore, in this study, we instead explore the effect of loss in coherency on the energy barriers. As the exact coherency conditions are not known, we consider the idealized scenario of a completely frictionless interface between the grain and the oxide. Under these conditions, there will be no transfer of the shear strain across the interface, and hence it presents the case of least strain energy barrier, while a completely bonded interface presents the other extreme of the maximum strain energy barrier.

3.2.1.6 In-plane compressive stress

The oxide matrix is considered to be in a state of biaxial compression, as observed in the films formed on zirconium (see C:ch2). We apply this stress as a predefined uniform stress field at the beginning of the simulation. As the simulation proceeds, transformation eigenstrains alter the stress field within the grain and in the adjacent regions of the matrix. Based on the evolution of stress obtained in thesis for the temperatures of 600 K $< T <$ 1000 K (refer Figure 2.7), we consider this bulk oxide compressive stress to vary in the range of $0 < |s_{\text{ox}}| < 2000$ MPa.

3.2.1.7 Grain and twin boundary energy (ΔG_{gb}, G_{tw})

In the view of randomness in the crystal orientation in the two in-plane directions (refer Section 3.2.1.3), we assume that the average grain boundary energy between the transformed monoclinic grain and the surrounding grains is the same as that between the untransformed tetragonal grain and the surrounding grains, i.e $\Delta\gamma_{gb} = 0$.

Twin boundary energy value for zirconia, $\gamma_{tw} = 0.44$ J/m^2, is taken directly from published data [46].

3.2.1.8 Chemical energy difference (ΔG_{ch})

We use published data from caloriemetric studies to estimate the chemical energy difference term, ΔG_{ch}. Coughlin *et al.* report an enthalpy difference of, $\Delta H = 5941$ J/mol and an entropy difference of $\Delta S = 4$ J/mol-K between the two phases. Therefore, we can write

$$\Delta G_{ch} = \Delta H - T\Delta S \approx (6000 - 4T) \text{ J/mol.} \tag{3.4}$$

To calculate the contribution of this term per unit volume, we divide it by the molar volume of zirconia, which is 21.8 cm^3/mol. We can then write

$$\Delta G_{ch} = [45846 \times (6000 - 4T)] \text{ J/m}^3. \tag{3.5}$$

3.3 Results

Deformed equiaxed and columnar grains under optimized twinning conditions are shown in Figure 3.9. Twin planes are parallel to the direction of the oxide growth in this configuration.

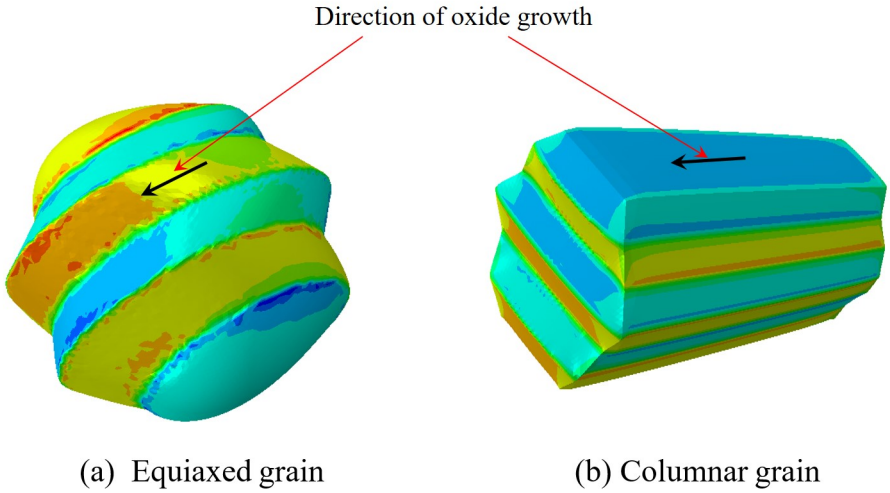

Figure 3.9: Deformed grain shapes post-transformation under optimized twinning conditions. Deformations are magnified by a factor of 10. Color contour indicates shear strain in the grain (red/yellow and blue regions have positive and negative shear strains respectively).

3.3.1 Effect of grain type and interface conditions

In this section, we show the effect of grain morphology and loss of coherency at the oxide-grain interface on the energy barrier to the phase transformation. Figure 3.10 shows the energy barrier for the phase transformation in grains at $T = 633$ K. This energy barrier has to be negative (i.e, free energy should reduce) in order to make this transformation favorable. We analyze the following three scenarios of interface conditions and twinning

1. Bonded grain-oxide interface+Twinning

2. Frictionless grain-oxide interface

3. Frictionless grain-oxide interface+Twinning

The results in Figure 3.10 show that the effect of twinning in reducing the energy barrier is more prominent in equiaxed grains than the columnar grains, while the effect of loss in coherency has similar effect on both the grain types. Furthermore, it shows that the columnar grains have a significantly lower strain energy as compared to the equiaxed grains. This is because grains with a larger aspect ratio, i.e the ones with a larger dimension along the direction of the oxide growth as compared to those along the in-plane directions, offer lower strain energy barriers due to a better accommodation of the shear eigen-strain. In the oxide layer, the width of different columnar grains does not show a significant variation. Therefore, among all columnar grain sizes, the longest one, with the highest aspect ratio shows the least energy barrier. Among all equiaxed grains, as the aspect ratio is the same and is ≈ 1, the smallest one offers the highest barrier due to a high value of twin boundary area per unit volume, the quantity A_{tw}/V_{grain} in Equation (3.3). All the other grain shapes and sizes observed within the oxide layer have energy barriers lying between these two extremes of Figure 3.4.

Values of the free energy barrier in Figure 3.10 indicates that loss in coherency can drive a martensitic phase transformation from tetragonal to monoclinic zirconia in the longest columnar grains of the oxide, however, such transformation is not feasible in equiaxed grains or relatively shorter columnar grains. In the next section, we will explore if elevated temperatures make it favorable for these grains to transform.

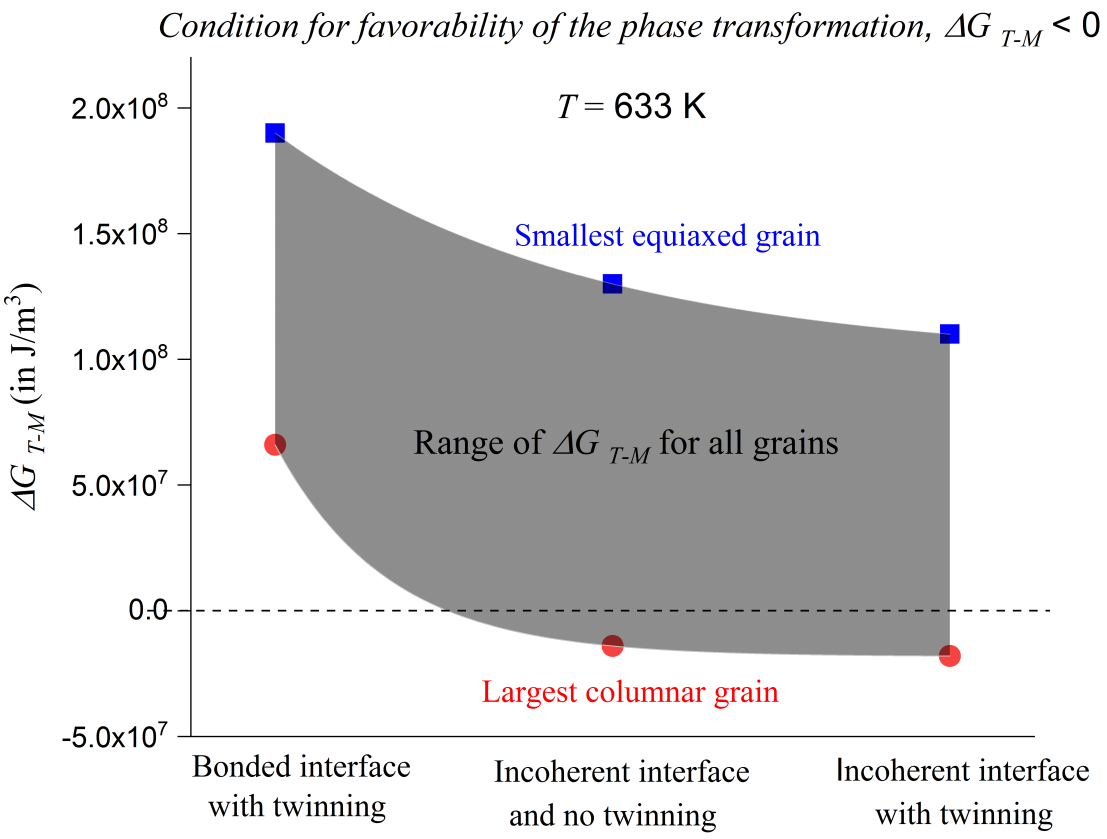

Figure 3.10: Free energy of transformation for all grains for different interface and grain twinning conditions at $T = 633$ K. Smallest equiaxed grain and largest columnar grains provide the maximum and minimum limits on the energy barrier respectively.

3.3.2 Effect of oxide stress and temperature

In this section, we show the effect of the stress-state within the oxide on the energetics of this phase transformation. We then use these results to analyze its favorability at elevated temperatures ($T > 633$ K).

The in-plane compressive state of stress within the oxide only influences the strain energy contribution in the free energy of Equation (3.3). Therefore, in Figure 3.11, we show the variation of the strain energy barrier ΔU with the magnitude of this stress, for an equiaxed grain with bonded interface undergoing twinning. The results show a rather weak dependence of the phase transformation energetics on the stress. Note that this behavior is replicated

for other grain structures and grain-oxide interface conditions as well. This behavior is in contradiction with the previous claims in the literature, of stress-relaxation within the oxide driving the phase transformation.

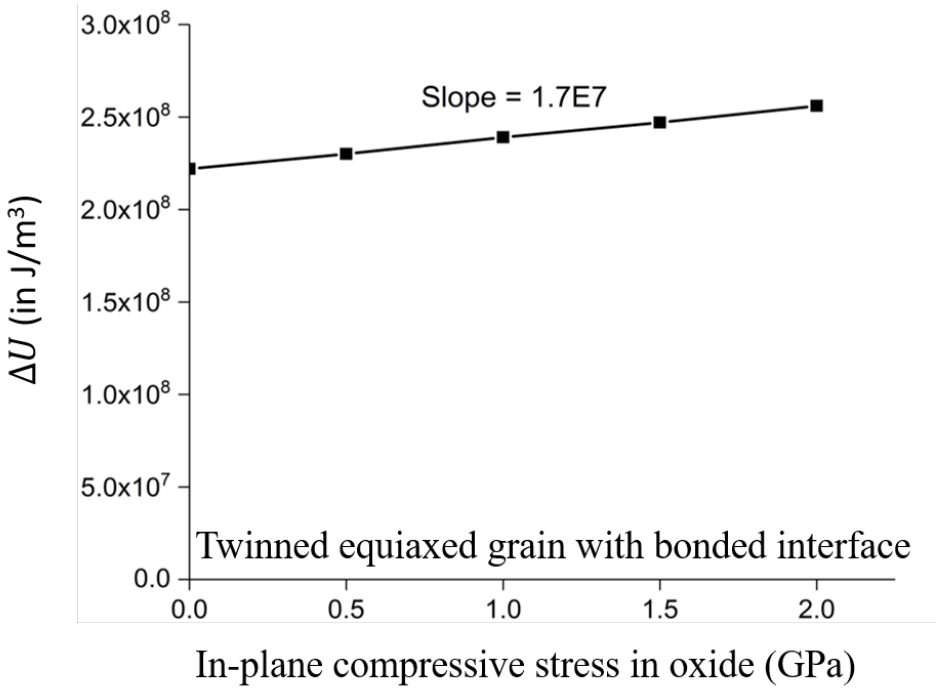

Figure 3.11: Effect of the in-plane compressive stress in the oxide on the strain energy barrier (ΔU) for the phase transformation. The results presented are for an equiaxed grain bonded with the oxide matrix and undergoing twinning.

In Figure 3.12, we show the effect of temperature on the energetics of the phase transformation in twinned grains forming a frictionless interface with the oxide. The drop in the strain energy barrier, ΔU, with increase in temperature is due to a lower average compressive stress within the oxide at high temperatures. The estimate of the stress near the first transition is used and its value is obtained using the analysis presented in C:ch2 of this thesis. This drop however is marginal in view of the results presented in Figure 3.11. The chemical driving force, ΔG_{ch} drops linearly as temperature rises (see Equation (3.5)). This is because tetragonal is the thermodynamically stable phase at higher temperatures. Therefore, the driving force for it to transform to monoclinic reduces as the temperature increases. The necessary condition for this phase transformation to occur is

$$|\Delta G_{ch}| > \Delta U. \tag{3.6}$$

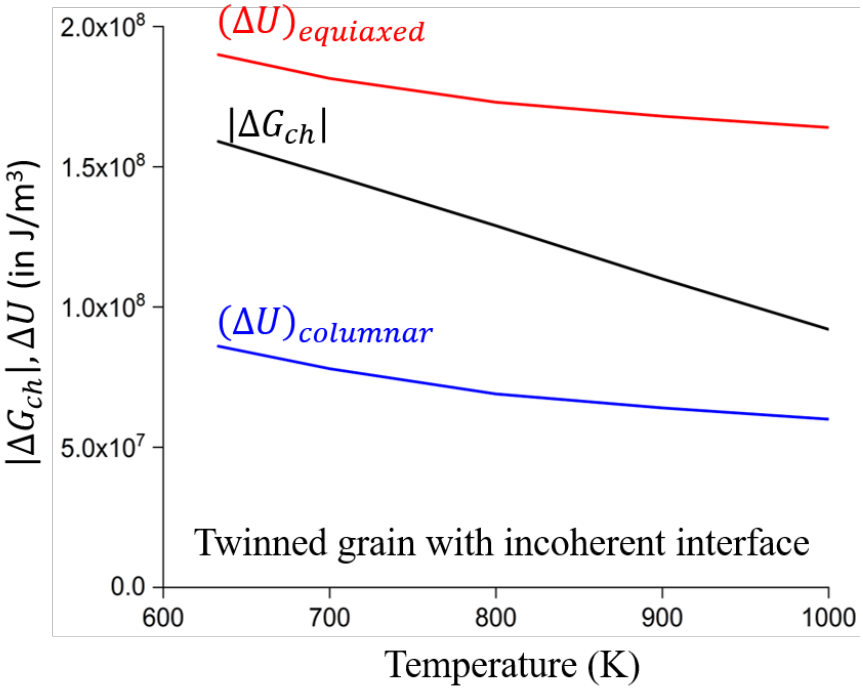

Figure 3.12: Variation of the chemical driving force $|\Delta G_{ch}|$ and the strain energy barrier ΔU with temperature for a frictionless (or completely incoherent) grain-oxide interface undergoing twinning.

The results in Figure 3.12 show that the drop in driving force is faster than the drop in the strain energy barrier. Therefore, for equiaxed grains, it remains infeasible to transform even at elevated temperatures of $T > 633$ K. For columnar grains, such a transformation can be shown as favorable for a certain range of variability in the value of twin boundary energy (γ_{tw}), as discussed in the next section.

3.3.3 Proposed range for twin boundary energy value (γ_{tw})

Figure 3.13 shows the free-energy change during transformation columnar grains transforming with twinning and a frictionless grain-oxide interface in the temperature range of 600 K $< T <$ 1000 K. The top curve is for twin boundary energy value proposed by Evans

et al. ($\gamma_{tw} = 0.44$ J/m^2). However, we find that its value should at least be reduced to $\gamma_{tw} = 0.24$ J/m^2 to reduce the energy barrier below 0 at these temperatures. Therefore, we need

$$\gamma_{tw} \leq 0.24 \text{ J/m}^2 \tag{3.7}$$

for columnar tetragonal grains to undergo transformation for temperatures up to 1000 K.

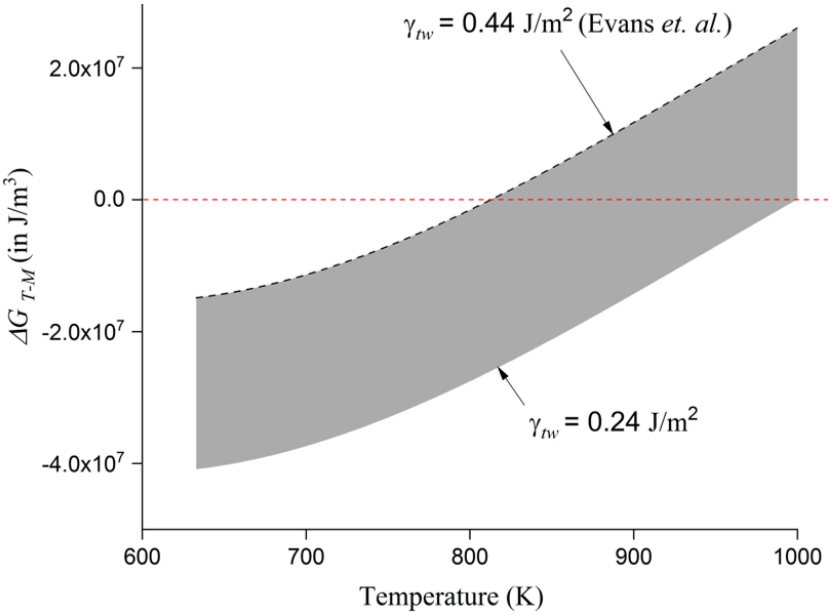

Figure 3.13: Free energy of transformation of columnar grains with incoherent interface, showing that a twin boundary energy value of $\gamma_{tw} < 0.24$ J/m^2 is required for it to be favorable in the temperature range of $T = 633 - 1000$ K.

3.4 Comparison with experimental observations

Most of the experimental studies only report the reduction in the average fraction of the tetragonal phase over time. For such cases, it is difficult to comment on which type of grains are undergoing transformation. However, Swan *et al.* [7] report the time evolution of tetragonal phase distribution across the oxide layer for oxidation temperature of $T = 623$ K. In these results, the tetragonal content at the oxide-water interface is observed to drop with time. Recall that the grains at this location are predominantly equiaxed (refer Figure 3.4). This is in contradiction with the results presented above in Figure 3.10 showing that it is

not feasible. This inconsistency is possibly a result of improper estimation of the chemical driving force (ΔG_{ch}) for the oxide layer formed on zirconium alloys. The value used in the continuum-analysis above [47] is obtained from caloriemetric studies on powdered zirconia. The oxide films will likely have a different chemical composition than these. However, to understand these effects, one needs to carry out atomistic simulations. In the next section, we present a preliminary molecular dynamics framework developed for that purpose.

3.5 Molecular dynamics analysis

In this section, we focus on understanding the effect of various crystallographic defects on the enthalpy difference between the two phases, the most significant component of the energy barrier, using molecular dynamics analysis. In our continuum-based model, we used a value of the enthalpy change during phase change from tetragonal to monoclinic to be $\Delta H = -6000$ J/mol [47]. However, experimental observation of transformation in equiaxed grains indicate towards a significantly larger drop in the enthalpy value during the transformation. Our aim is to analyze whether crystallographic defects present in the oxide film will likely cause this effect.

3.5.1 Modelling framework

LAMMPS Molecular Dynamics Simulator was used for the purpose of this study. Born-Mayer-Buckingham model of the following form was used to capture the interatomic interaction between various atoms of zirconia [48, 49]

$$E_{ij} = \frac{q_i q_j}{r_j} + A_{ij} exp\left(-\frac{r_{ij}}{\rho}\right) - \frac{C_{ij}}{r_{ij}^6}. \tag{3.8}$$

This model is a commonly used for ionic solids in which the interaction is broken down into short and long-range components. While the first term constitutes the long-range coulombic interaction, the last two terms capture the short-range interaction and hence have a much

stronger dependence on the interatomic distances (r_{ij}). We used the same model parameters as Zhang *et al.* [48] in their study of zirconia, in the view that these set of parameters more accurately reproduce the experimentally measured properties of elastic constants, lattice energy, and oxygen diffusion.

We specified Ewald summation method of computing long-range forces (e.g the electrostatic forces) in LAMMPS. This method computes the long-range forces in a Fourier space and the short-range forces in the real space leading to a faster convergence. We used the periodic boundary conditions in all three directions for both the tetragonal and monoclinic simulation cells. Energy minimization of the cells is then carried out at $T = 0$ K. As the free energy difference between the two phases can be written as

$$\Delta G = \Delta H - TS, \tag{3.9}$$

the value of energy difference computed from the molecular dynamics at $T = 0$ K will be equal to the enthalpy of the transformation (ΔH). We compute this value for the following crystal defects

1. Anion/oxygen-ion interstitial: The regions near the oxide-water interface can have a high concentration of oxygen ion interstitial during oxidation due to an abundant supply.

2. Cation/tin atom substitutional defect: Tin is a dopant atom used in zirconium alloys like Zircaloy-4, Zirlo etc. As it can exhibit an electrovalence of +4, same as that of zirconium, it can form a substitutional defect when incorporated in the oxide film during oxidation.

3.6 Preliminary results

In this section, we discuss the relative behavior of the tetragonal and monoclinic phases in the presence of various defects.

The relaxed monoclinic and tetragonal lattice structures are shown in Figure 3.14. As expected from the thermodynamics of these two phases, monoclinic was found to be significantly more stable than the tetragonal phase at $T = 0$ K. The difference in energy was computed giving transformation enthalpy as follows

$$\Delta H = E_m - E_t = -8881.6\,\mathrm{J/mol} \tag{3.10}$$

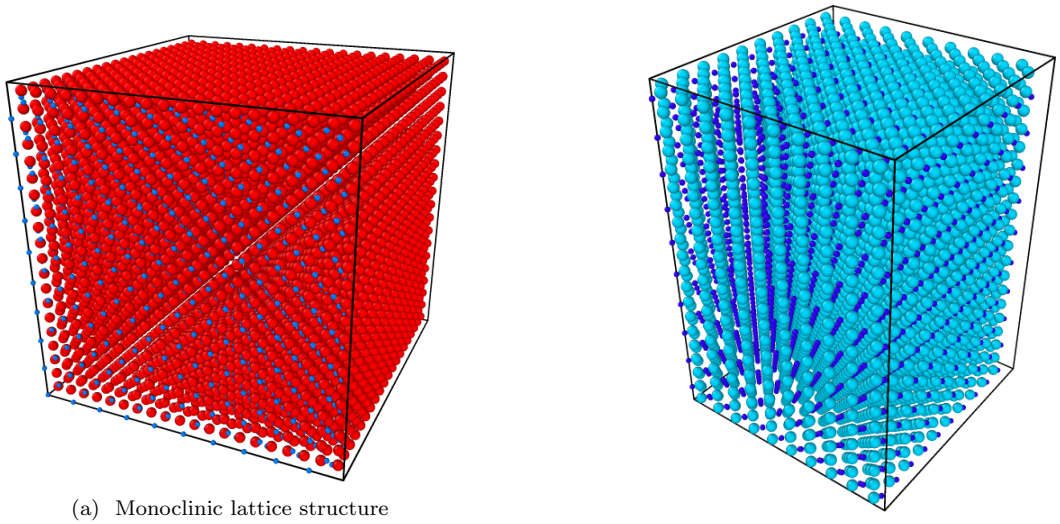

(a) Monoclinic lattice structure

(b) Tetragonal lattice structure

Figure 3.14: Relaxed lattice structures of the two phases of zirconia at $T = 0$ K in absence of any crystallographic defects. Bigger spheres represent the oxygen atoms and the smaller ones represent the zirconium atoms.

3.6.1 Effect of an anion interstitial

We introduce an oxygen interstitial into the two lattice structures and the relaxed structures are shown in Figure 3.15. The atoms are colored based on the coordination number, with blue being the lowest and red the highest. Tetragonal structure has approximately 3% lower volume than the monoclinic, implying that the atoms are more closely packed in the former. As a result, tetragonal shows a significantly higher distortion of surrounding atoms due to the oxygen interstitial. The interstitial formation energy are obtained as follows

$$(E_i^f)_m = 27.31 \text{ eV} \; ; \quad (E_i^f)_t = 28.18 \text{ eV} \tag{3.11}$$

Though energy needs to be provided to create an interstitial in both the phases, it favors the monoclinic phase significantly more than the tetragonal phase.

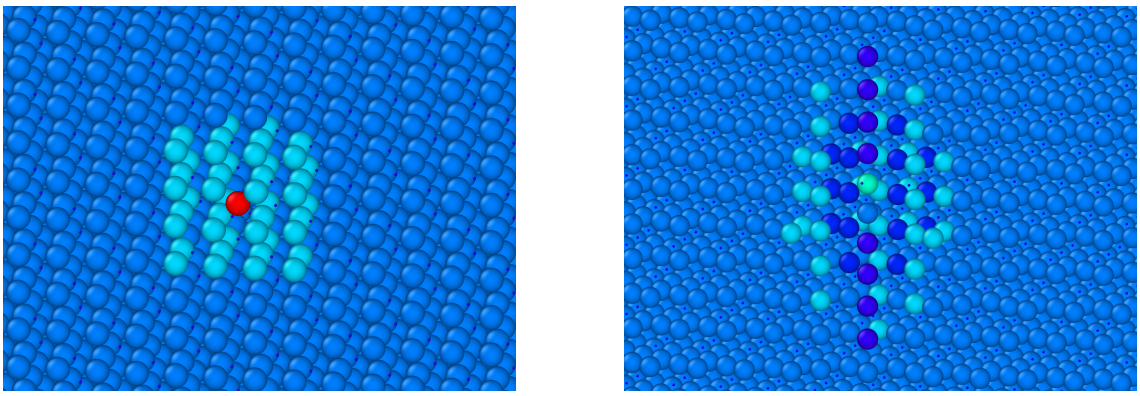

(a) Monoclinic lattice structure

(b) Tetragonal lattice structure

Figure 3.15: Relaxed lattice structures of the two phases of zirconia at $T = 0$ K in the presence of an oxygen interstitial. The atoms are colored based on the coordination number, with blue being the lowest and red the highest. Bigger spheres represent the oxygen atoms and the dots represent the zirconium atoms.

We also note that the system in not charge-neutral (net charge $= -2$) and the Ewald-summation method may not be very accurate for such cases. However, even though the energy values may not be very accurate with charged systems, the qualitative trends and comparisons between the two phases can still provide a useful insight into the inconsistencies between our continuum-based model and the experimental data.

3.6.2 Effect of a cation substitutional defect

Tin (Sn) is used as an alloying element in many commercial zirconium alloys. Therefore, we substituted a zirconium atom with a tin atom of the same valency (+4). This system is therefore charge neutral. The relaxed structures are shown in Figure 3.16. The energy change associated with this substitution are as follows

$$(E_s)_m = -8.45 \text{ eV} \; ; \quad (E_s)_t = -6.63 \text{ eV} \tag{3.12}$$

While replacement of Zr with tin reduces the system of the energy in both the phases. Some of the oxygen atoms (blue spheres) are observed to be displaced significantly from their perfect lattice position around the tin atom (pink) in tetragonal zirconia in Figure 3.16. It might be because of this that the substitution is not favored in this phase as much as the monoclinic zirconia.

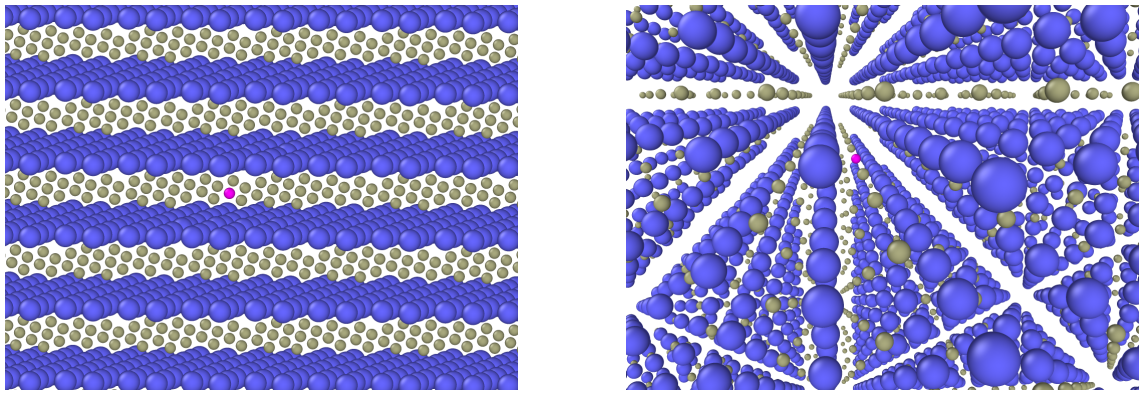

(a) Monoclinic lattice structure

(b) Tetragonal lattice structure

Figure 3.16: Relaxed lattice structures of the two phases of zirconia at $T = 0$ K with substitution of a zirconium atom (green) with tin atom (pink). The atoms are colored based on the their type. Blue spheres represent the oxygen atoms.

The table below summarizes the results of molecular dynamic analysis and compares the enthalpy difference between the two phases under individual defects, against the perfect lattice structure. Effect of an oxygen interstitial and a tin (Sn) substitutional defect was studied on the tetragonal and the monoclinic phase of zirconia. While both of these defects are found to favor monoclinic phase, effect of oxygen interstitial is relatively more significant.

	$\Delta H = (H_m - H_t)(J/mol)$
Perfect lattice	-8882
oxygen interstitial	-11354
Sn substitutional	-10538

Though the transformation enthalpy value obtained for the case of interstitial defect is sufficient to bridge the inconsistencies between the continuum-based model and the experimental data, the compromise on accuracy by using the ewald summation method for systems with a net charge (in the interstitial defect case) makes us give less importance to the actual numbers. The qualitative comparison still provides a useful insight into the qualitative effect of crystal defects on the energetics of this phase transformation.

3.7 Conclusions

In this chapter, we studied the energetics of the martensitic transformation of the metastable tetragonal phase of the oxide formed on zirconium alloys, to the thermodynamically stable monoclinic phase for temperatures of 600 K $< T <$ 1000 K. Loss in coherency at the grain-oxide interface is observed to play a crucial role in reducing the energy barrier for the phase transformation. Phase transformation is found to be significantly more favorable in columnar grains (i.e shapes with aspect ratio$>$ 1) as compared to the equiaxed grains. Based on the continuum-based analysis, previous claims in the literature of stress-relaxation driving a bulk phase transformation, and hence a transition in oxidation kinetics does not seem reasonable.

The continuum analysis results obtained in this study are found to be contradictory to the experimental observation of equiaxed grains undergoing phase transformation in the oxide film. To understand this inconsistency, we studied the effect of crystallographic defects on the transformation enthalpies using molecular dynamics analysis. This study indicated that some of the common defects present within the oxide layer, such as oxygen ion interstitial, and Tin dopant substitutional defect, can increase the driving force to the transformation and hence explain the above mentioned inconsistency in the continuum-based analysis.

Chapter 4

Application of Turing's Pattern Formation Theory to Oxidation-Type Systems

4.1 Introduction

Alan Turing proposed his pioneering theory for pattern formation in biological systems in 1952 [50]. It relies on the existence of a system of biochemical species he called morphogens (in view of their possible role in determining the structure of living organisms), reacting and diffusing within a tissue. He suggested that the development of patterns in an initially homogeneous embryo, e.g, leaves arranging periodically on a plant stem, can correspond to the stable stationary waves of the concentration of morphogens generated as the result of an instability of the homogeneous equilibrium state. The simplicity of the theory, and its capability to produce a wide range of distinctive patterns, has triggered significant efforts to find specific applications. Murray's [13] extension of this work, in a paper titled "How the leopard gets its spots", shows striking similarities between simulated Turing patterns and the stripes/spots observed on various mammalian coats. Kondo *et al.* [14] used this framework to simulate stripes on the marine angelfish, Pomacanthus, showing that it can explain the observation that the stripe spacing remains constant as the fish grows. Meinhardt *et al.* [15] proposed a reaction-diffusion model that accurately reproduces the diverse patterns observed on the shells of molluscs. A recent study [16] has indicated that the skin denticles on sharks, the structures that allow them to swim swiftly, could also be a result of an

underlying Turing mechanism. Though originally developed and applied extensively to the field of developmental biology, as discussed above [13, 14, 15, 16, 17, 18], the mathematical formalism of the theory has also been found to be applicable to a much broader range of scientific problems, including the study of geological and demographic patterns [51, 52].

4.1.1 Mathematical structure

A Turing system is typically characterized by the evolution of spatial patterns in the concentrations or values $u(x,t), v(x,t)$ of two interacting species, where x and t correspond to spatial and temporal coordinates respectively. Such a system with linear diffusion can be described by the differential equations

$$\begin{aligned} \frac{\partial u}{\partial t} &= D_u \frac{\partial^2 u}{\partial x^2} + f(u,v) \\ \frac{\partial v}{\partial t} &= D_v \frac{\partial^2 v}{\partial x^2} + g(u,v) \ , \end{aligned} \tag{4.1}$$

where D_u and D_v are the diffusion coefficients for u and v respectively. The functions $f(u,v)$ and $g(u,v)$ define the influence of each concentration on its own growth rate, and also the coupling between the two concentrations. Instabilities can occur, leading to pattern formation, if one species (the *activator*) has a promoting effect on itself, whilst the other suppresses itself. Here we shall take v to represent the activator, in which case the inequalities

$$\frac{\partial g(u,v)}{\partial v} > 0 \ ; \quad \frac{\partial f(u,v)}{\partial u} < 0 \ ; \quad \frac{\partial g(u,v)}{\partial u}\frac{\partial f(u,v)}{\partial v} < 0 \ ; \quad D_u > D_v \tag{4.2}$$

define a necessary but not sufficient condition for pattern formation. The inequality $D_u > D_v$ requires that the activator should be less mobile than u.

The third inequality in (Equation (4.2)) implies that u and v have opposite effects on each other and it can be satisfied in two different ways — i.e.

$$\frac{\partial g(u,v)}{\partial u} < 0 \quad \text{and} \quad \frac{\partial f(u,v)}{\partial v} > 0 \tag{4.3}$$

or

$$\frac{\partial g(u,v)}{\partial u} > 0 \quad \text{and} \quad \frac{\partial f(u,v)}{\partial v} < 0 \, . \tag{4.4}$$

The conditions (Section 4.2) define an *activator-inhibitor system*, since v activates both itself and u, whilst the *inhibitor* u suppresses both itself and v. By contrast, (Equation (4.4)) defines an *activator-substrate system*, in which u suppresses itself but promotes v, whilst v promotes itself and suppresses u. In this case u is called the *substrate*, since it is consumed whilst producing the activator v.

4.1.2 Moving boundary problems

Several forms have been proposed for the interaction functions $f(u,v), g(u,v)$, and have been shown to be capable of predicting the development of Turing patterns in appropriate parameter ranges [53, 54, 55]. Many of these studies have focussed on fixed spatial domains, but the results have proved useful in interpreting the experimentally observed behaviour of physical systems where the domain grows in time [56, 16]. Crampin *et al.* [57] developed a rigorous analytical framework for problems of this class, and demonstrated the significance of domain growth as a possible mechanism for reliability in pattern selection. In particular, the long-time pattern is then independent of the initial conditions, in contrast to results for fixed domains [57, 58]. This framework has been applied to systems where all elements of the spatial domain grow either at a prescribed growth rate [57, 58, 59, 60], or at a rate that is controlled by the species/reactants [61, 62]. Recently, the analysis of such systems was extended to include the effect of anisotropy in growth rates and the curvature of growing ellipsoidal surfaces [63]. This case of bulk growth is appropriate for a wide variety of biological systems, where each tissue within the domain grows in size. However, there is another class of spatially-patterned systems where the domain grows only locally, at a domain boundary or interface — for example, apically growing biological systems [64], oxide layers formed on certain alloys [1] and cloud patterns [65].

Crampin *et al.* [59] simulated Turing systems with a moving domain boundary, and

observed the development of a stationary periodic structure behind the moving front. Similar results were obtained by other authors [66, 67, 68], but all these investigations were restricted to systems in which the boundary was prescribed to move at a constant rate. However, we are interested in physical systems for which the boundary or interface motion is not prescribed by an external agent, but results from the physics within the domain, such as local concentrations of species. For example, pollen tubes, which exhibit localized growth at a tip [69], are observed to have oscillatory growth rates [70] and periodic depositions of certain pectins [71]. In oxide films formed on zirconium alloys, periodic increases from an approximately parabolic rate of the metal-oxide interface movement (which, like many other oxidation processes [72], is controlled by the local concentration of the oxygen ions) are observed [1]. Additionally, the oxide film exhibits a layered structure that is directly correlated with this periodicity [1]. To the best of our knowledge, there are no existing theories which provide a rigorous explanation of the phenomena discussed above.

In this chapter, we investigate the interaction between a pattern-causing Turing instability and the motion of a domain boundary for cases where the instantaneous boundary velocity is driven by a local concentration. In particular, we shall document the nature of this interaction in the context of Gierer-Meinhardt's activator-inhibitor model, and Schnakenberg's activator-substrate model, as shown in the next section.

4.2 Activator-inhibitor system

Gierer and Meinhardt [53] define their activator-inhibitor model through the equations

$$\frac{\partial u}{\partial t} = D_u \frac{\partial^2 u}{\partial x^2} + c_1 v^2 - c_2 u \; ; \quad \frac{\partial v}{\partial t} = D_v \frac{\partial^2 v}{\partial x^2} + \frac{c_3 v^2}{u} - c_4 v \; . \tag{4.5}$$

In this chapter, we consider the domain defined by $0 < x < h(t)$, where $x = 0$ is a fixed boundary, and $x = h(t)$ is a moving boundary whose motion is determined by local

concentrations. In particular, we assume

$$\frac{dh}{dt} = ku(h,t) \tag{4.6}$$

where k is a constant that might represent a reaction constant if the boundary motion is associated with a chemical reaction [72]. At the fixed boundary $x = 0$, we assume

$$u(0,t) = u_0 \; ; \quad \frac{\partial v}{\partial x}(0,t) = 0 \; ; \tag{4.7}$$

and at the moving boundary,

$$v(h,t) = v_h \; ; \quad -D_u \frac{\partial u}{\partial x}(h,t) = [u(h,t) + Q] \, \frac{dh}{dt} \; . \tag{4.8}$$

The last condition represents a flux balance for the species u, with the constant Q representing the amount of u consumed per unit area in moving the boundary through a unit distance. If the species u acts only as a catalyst for the process that drives the boundary motion, Q may be taken as zero.

Non-dimensionalization of equations

A dimensionless form of Equation (4.5)-Equation (4.8) can be obtained by defining

$$\tilde{u} = \frac{c_1 u}{c_2} \; ; \quad \tilde{v} = \frac{c_1 v}{c_2} \; ; \quad \tilde{x} = x\sqrt{\frac{c_2}{D_u}} \; ; \quad \tilde{t} = c_2 t \; ; \quad \tilde{h} = h\sqrt{\frac{c_2}{D_u}} \; . \tag{4.9}$$

Using these expressions in the governing (Equation (4.5)) and the boundary conditions (Equation (4.6)-Equation (4.8)) we obtain the following governing differential equations

$$\begin{aligned} \frac{\partial \tilde{u}}{\partial \tilde{t}} &= \frac{\partial^2 \tilde{u}}{\partial \tilde{x}^2} - \tilde{u} + \tilde{v}^2 \\ \frac{\partial \tilde{v}}{\partial \tilde{t}} &= R_D \frac{\partial^2 \tilde{v}}{\partial \tilde{x}^2} + \tilde{c}_3 \frac{\tilde{v}^2}{\tilde{u}} - \tilde{c}_4 \tilde{v} \end{aligned} \tag{4.10}$$

and the following boundary conditions

$$\frac{d\tilde{h}}{d\tilde{t}} = \tilde{k}\tilde{u}(\tilde{h},\tilde{t}) \ , \tag{4.11}$$

$$\tilde{u}(0,\tilde{t}) = \tilde{u}_0 \quad \text{and} \quad \frac{\partial\tilde{v}}{\partial\tilde{x}}(0,\tilde{t}) = 0 \ , \tag{4.12}$$

$$\tilde{v}(\tilde{h},\tilde{t}) = \tilde{v}_{\tilde{h}} \quad \text{and} \quad -\frac{\partial\tilde{u}}{\partial\tilde{x}}(\tilde{h},\tilde{t}) = \left[\tilde{u}(\tilde{h},\tilde{t}) + \tilde{Q}\right]\frac{d\tilde{h}}{d\tilde{t}} \ . \tag{4.13}$$

where

$$R_D = \frac{D_v}{D_u} \ ; \ \ \tilde{c}_3 = \frac{c_3}{c_2} \ ; \ \ \tilde{c}_4 = \frac{c_4}{c_2} \ ; \ \ \tilde{u}_0 = \frac{c_1 u_0}{c_2} \ ; \quad \tilde{v}_h = \frac{c_1 v_h}{c_2} \ ; \ \ \tilde{Q} = \frac{c_1 Q}{c_2} \ ; \ \ \tilde{k} = \frac{k}{c_1}\sqrt{\frac{c_2}{D_u}} \tag{4.14}$$

are the independent dimensionless parameters defining the system.

Stability in an infinite spatial domain

Section 5.2.1 have a homogeneous steady-state solution

$$\tilde{v} = \frac{\tilde{c}_3}{\tilde{c}_4} \ ; \quad \tilde{u} = \left(\frac{\tilde{c}_3}{\tilde{c}_4}\right)^2 \tag{4.15}$$

in an infinite spatial domain. Nesterenko *et al.* [71] derived the condition

$$\frac{D_u}{D_v} > \frac{c_2}{(3-2\sqrt{2})\,c_4} \tag{4.16}$$

for the homogeneous solution of (Equation (4.5)) to be unstable, leading to the formation of Turing patterns. Using the notation (Equation (4.14)), this can be expressed in the form

$$\frac{\tilde{c}_4}{R_D} > \frac{1}{(3-2\sqrt{2})} \approx 5.82 \ . \tag{4.17}$$

This instability results in the formation of the stationary, periodic concentration profiles in an infinite spatial domain, associated with Turing patterns [53]. In a finite fixed domain,

the periodicity may be modified near the boundaries, in order to adjust to the boundary conditions.

4.2.1 Numerical procedure

For the numerical solution of these equations, it is convenient to use the coordinate transformation $\tilde{x} = \zeta\tilde{h}(\tilde{t})$ to convert the problem to one on the fixed domain $0 < \zeta < 1$. The governing equations then take the form

$$\frac{\partial\tilde{u}}{\partial\tilde{t}} = \frac{\zeta}{\tilde{h}}\frac{d\tilde{h}}{d\tilde{t}}\frac{\partial\tilde{u}}{\partial\zeta} + \frac{1}{\tilde{h}^2}\frac{\partial^2\tilde{u}}{\partial\zeta^2} - \tilde{u} + \tilde{v}^2 \tag{4.18}$$

$$\frac{\partial\tilde{v}}{\partial\tilde{t}} = \frac{\zeta}{\tilde{h}}\frac{d\tilde{h}}{d\tilde{t}}\frac{\partial\tilde{v}}{\partial\zeta} + \frac{R_D}{\tilde{h}^2}\frac{\partial^2\tilde{v}}{\partial\zeta^2} + \tilde{c}_3\frac{\tilde{v}^2}{\tilde{u}} - \tilde{c}_4\tilde{v} \tag{4.19}$$

$$\frac{d\tilde{h}}{d\tilde{t}} = \tilde{k}\tilde{u}(1,\tilde{t}) \ , \tag{4.20}$$

with boundary conditions

$$\tilde{u}(0,\tilde{t}) = \tilde{u}_0 \ ; \ \ \frac{\partial\tilde{v}}{\partial\zeta}(0,\tilde{t}) = 0 \ ; \ \ \tilde{v}(1,\tilde{t}) = \tilde{v}_h \ ; \ \ -\frac{\partial\tilde{u}}{\partial\zeta}(1,\tilde{t}) = \tilde{h}\left[\tilde{u}(1,\tilde{t}) + \tilde{Q}\right]\frac{d\tilde{h}}{d\tilde{t}} \ . \tag{4.21}$$

This system of equations was solved using the finite-element-based software package FlexPDE Professional version 7.15.

To start the solution procedure, we needed to define a finite initial domain size $\tilde{h}(0) \equiv \tilde{h}_0$ and the corresponding initial spatial distributions $\tilde{u}(\zeta,0), \tilde{v}(\zeta,0)$. Here we used $\tilde{h}_0 = 1$ and simple linear distributions, with parameters chosen to satisfy (Equation (4.20), Equation (4.21)). In general, the numerical results were found to be insensitive to initial conditions once the domain size was large compared with $\tilde{h}_0$.

4.2.2 Characterization of the model response

The response of the model can be periodic or non-periodic depending on the values of the dimensionless parameters $\tilde{c}_3, \tilde{c}_4, R_D, \tilde{k}, \tilde{Q}$ and the boundary values $\tilde{u}_0$ and $\tilde{v}_{\tilde{h}}$. In this

section, we shall give illustrations of several kinds of behaviour, and some indication of the parameter ranges in which they are to be expected.

The simplest class of behaviour is that where the inequality (Equation (4.17)) is not satisfied, so that the homogeneous solution is stable. In this case, the moving boundary may advance at a constant rate, or it may show periodic variations depending on parameter values, but the distributions of $\tilde{u}, \tilde{v}$ eventually converge on the homogeneous solution (Equation (4.15)), except in regions adjacent to the instantaneous domain boundaries.

If the homogeneous solution is unstable, the distributions far from the moving front should be unaffected by it, and hence must converge on a steady state that is stable in an infinite domain. In Appendix 4.A, we determine both stable and unstable periodic steady-state solutions of Section 5.2.1, using the MATLAB package pde2path [73, 74]. For given parameter values satisfying (Equation (4.17)), stable periodic solutions exist in a finite range of wavelengths, the upper bound of which is significantly higher than that obtained by linear perturbation of the homogeneous solution. For systems not satisfying (Equation (4.17)), no periodic solutions are obtained.

4.2.2.1 Periodic behavior

Figure 4.1 shows (a) Contours of $\tilde{u}$ and the motion of the domain boundary $\tilde{h}(\tilde{t})$, and (b) the spatiotemporal distributions of $\tilde{u}$ (following the work of Crampin *et al.* [57]), for the parameter values $\tilde{c}_3 = 1, \tilde{c}_4 = 0.6, R_D = 3/40, \tilde{k} = 1, \tilde{Q} = 1$ and boundary values $\tilde{u}_0 = 1, \tilde{v}_h = 0.3$. In Figure 4.1(a), segments of 'convex-upward' boundary kinetics are separated by rapid changes of velocity, which we refer to as 'transitions'. Each transition corresponds to the formation of a peak in the concentrations of both $\tilde{u}$ (as shown in Figure 4.1(b)), and $\tilde{v}$. After the passage of the moving boundary, the spatial distributions rapidly converge on a stationary periodic pattern [except near the fixed boundary] in which the peaks of $\tilde{u}$ and $\tilde{v}$ coincide.

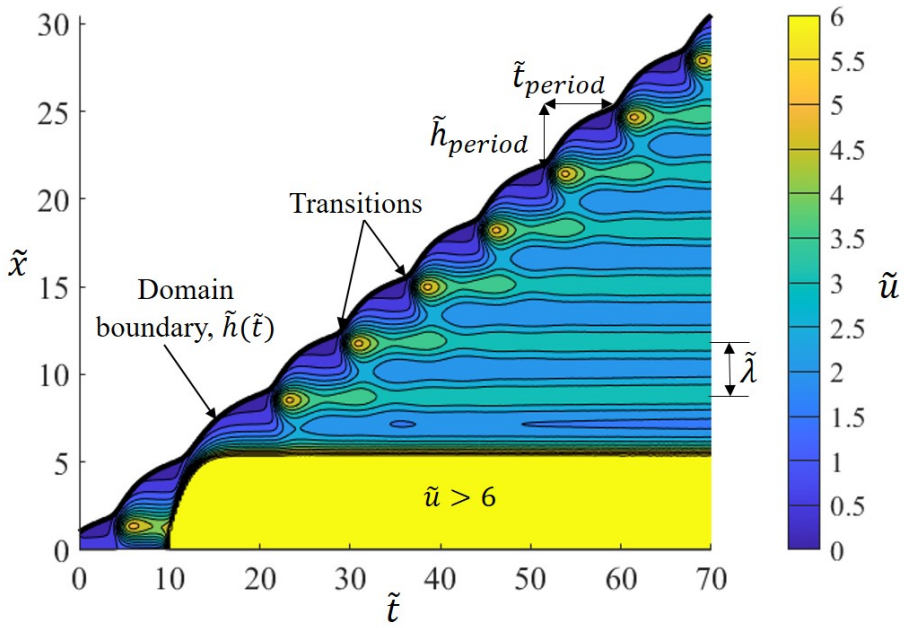

(a)

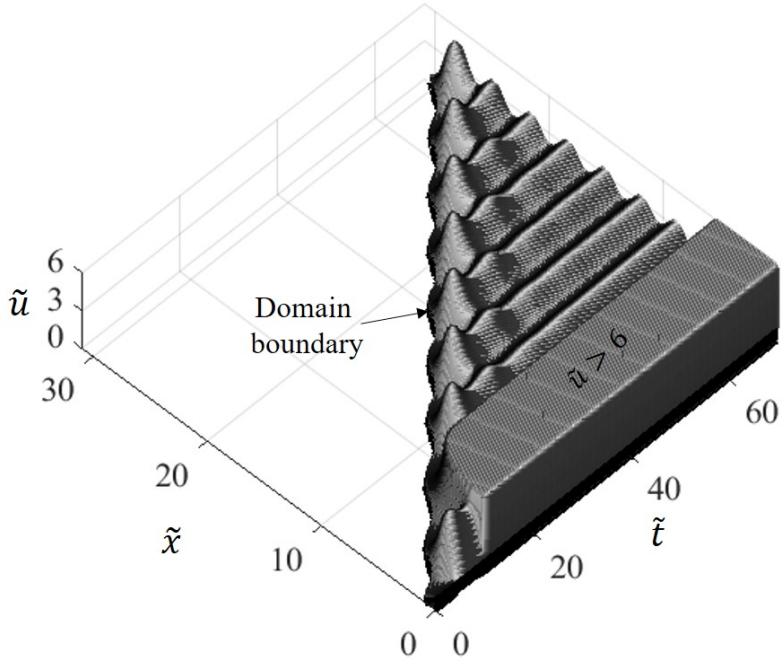

(b)

Figure 4.1: Periodic Behaviour : (a) Contours of $\tilde{u}$ showing periodic transitions between convex-upward segments of the boundary kinetics, each caused by a peak in $\tilde{u}$ at the moving front. The distance traversed between two transitions, $\tilde{h}_{\text{period}}$, is equal to the wavelength ($\tilde{\lambda}$) of the stationary pattern left behind the moving front. (b) Spatiotemporal concentration profile for the species $\tilde{u}$ showing development of peaks at the moving front. $\tilde{x}$ is the distance from the fixed surface. Results are obtained using Gierer-Meinhardt activator (v)-inhibitor (u) kinetics with $\tilde{c}_4 = 0.6$, $R_D = 3/40$, $\tilde{c}_3 = 1$, $\tilde{u}_0 = 1$, $\tilde{v}_{\tilde{h}} = 0.3$, $\tilde{Q} = 1$ and $\tilde{k} = 1$.

In Figure 4.1, each transition corresponds to a peak at the moving boundary and these peaks persist so that the resulting stationary pattern has dimensionless wavelength, $\tilde{\lambda}$, equal to the advance, $\tilde{h}_{\text{period}}$, of the moving front between successive transitions. However, if $\tilde{c}_4$ is increased to 1.4, keeping the other parameters unchanged, the function $\tilde{h}(\tilde{t})$ has a periodic form similar to that in Figure 4.1(a), but behind the moving front every second peak starts to decay, and the pattern eventually evolves to one with a wavelength $\tilde{\lambda} = 2\tilde{h}_{\text{period}}$.

Fixed-domain simulations (see Appendix 4.A) using these parameter values show that steady-state periodic solutions do exist with a wavelength $\tilde{\lambda} = \tilde{h}_{\text{period}}$, but they are unstable. Thus, the moving front imposes a certain periodicity on the pattern, but its persistence as a steady state or its subsequent evolution depend on features of the equation system that are independent of the domain size or its evolution in time.

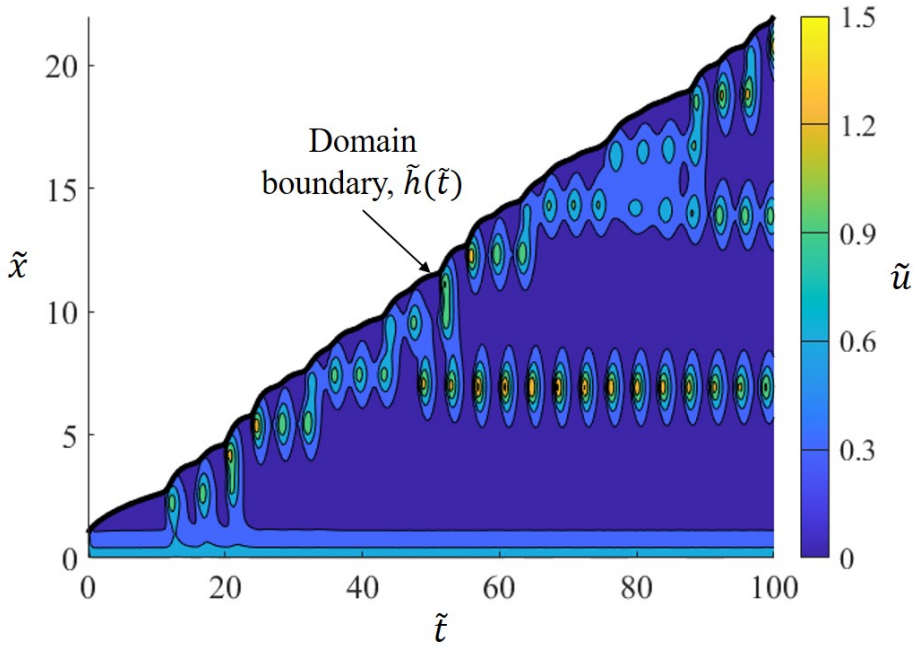

(a)

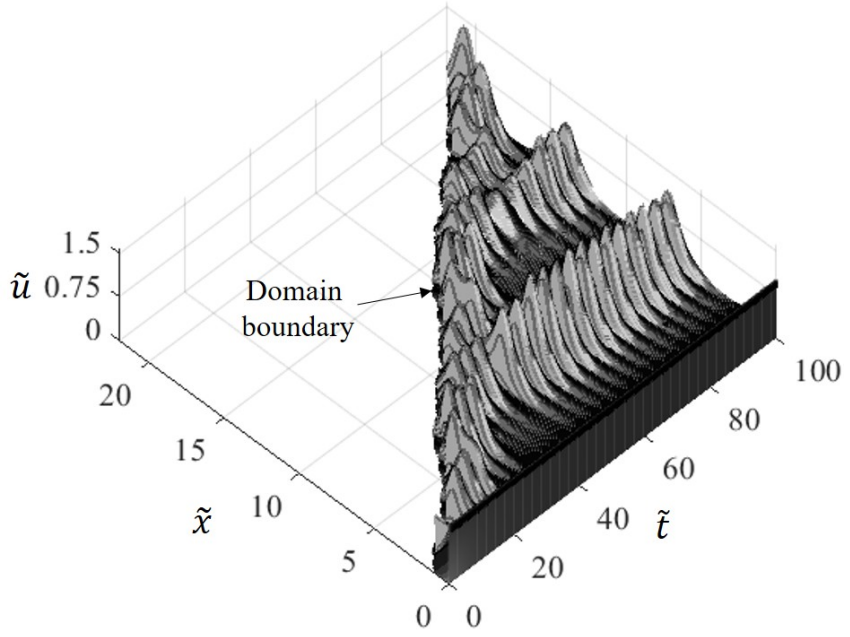

(b)

Figure 4.2: Random behaviour: (a) Contours of $\tilde{u}$ showing erratic boundary kinetics. (b) Spatiotemporal evolution of the species $\tilde{u}$ showing random development of peaks at the moving boundary, and the following erratic fluctuations in the amplitude for Gierer-Meinhardt activator (v)-inhibitor (u) kinetics with $\tilde{c}_4 = 1.8$, $R_D = 3/40$, $\tilde{c}_3 = 1$, $\tilde{u}_0 = 1$, $\tilde{v}_{\tilde{h}} = 0.3$, $\tilde{Q} = 1$ and $\tilde{k} = 1$. Homogeneous initial conditions consistent with the boundary conditions are used.

4.2.2.2 Random behaviour

If $\tilde{c}_4$ is increased further to 1.8 whilst keeping the other parameters unchanged from those used in Figure 4.1, the boundary velocity exhibits essentially random perturbations from an otherwise linear trend as shown in Figure 4.2(a). The corresponding concentrations of $\tilde{u}$ at the moving boundary also fluctuate randomly, but as the boundary recedes, the distributions evolve into relatively isolated peaks as shown in Figure 4.2(b). The amplitudes of these peaks fluctuate erratically, with some decaying eventually to zero. The others stabilize at a more or less reproducible maximum value, which for these parameter values is $\tilde{u}_{\max} \approx 0.64, \tilde{v}_{\max} \approx 1.56$. Throughout this transient process, peaks in $\tilde{u}$ and $\tilde{v}$ remain spatially coincident.

4.2.2.3 Periodic boundary motion without patterns

If $\tilde{c}_4$ in the above case is increased beyond about 1.9, the boundary motion reverts to a convex-upward periodic form like that in Figure 4.1(a), but the distributions of $\tilde{u}$ and $\tilde{v}$ then decay asymptotically to zero, so that regions away from the boundaries eventually become completely devoid of both species. At first sight, this appears to be inconsistent with the presence of the term $\tilde{c}_4\tilde{v}^2/\tilde{u}$ in (Section 5.2.1). However, if we assume that $\tilde{u}, \tilde{v}$ are spatially homogeneous and that $\tilde{v} \ll \tilde{u}$, these equations can be approximated as

$$\frac{d\tilde{u}}{d\tilde{t}} + \tilde{u} = 0 \; ; \quad \frac{d\tilde{v}}{d\tilde{t}} + \tilde{c}_4\tilde{v} = 0 \; , \tag{4.22}$$

with solution $\tilde{u} = C\exp(-\tilde{t}),\ \tilde{v} = D\exp(-\tilde{c}_4\tilde{t})$ where C, D are constants. The condition $\tilde{v} \ll \tilde{u}$ then reduces to

$$\frac{D}{C}\exp\left[(1-\tilde{c}_4)\tilde{t}\right] \ll 1 \; , \tag{4.23}$$

which will be satisfied for all $\tilde{t}$ if $\tilde{c}_4 > 1$ and the initial conditions are chosen such that $D/C \ll 1$. Thus $\tilde{c}_4 > 1$ is a necessary but not sufficient condition for $\tilde{u}$ and $\tilde{v}$ to decay towards zero, as is shown by the results described above for $\tilde{c}_4 = 1.4$ and 1.8.

4.2.3 Dependence of Turing-pattern wavelength on boundary kinetics

For the Gierer-Meinhardt model, Turing patterns correspond to stable time-invariant periodic solutions of (Section 5.2.1). The results described above show that boundary kinetics have a significant effect on the distributions generated immediately behind the moving front, but the resulting patterns persist only if they lie in the appropriate stable wavelength range (see Appendix 4.A), or if they can evolve to such a wavelength.

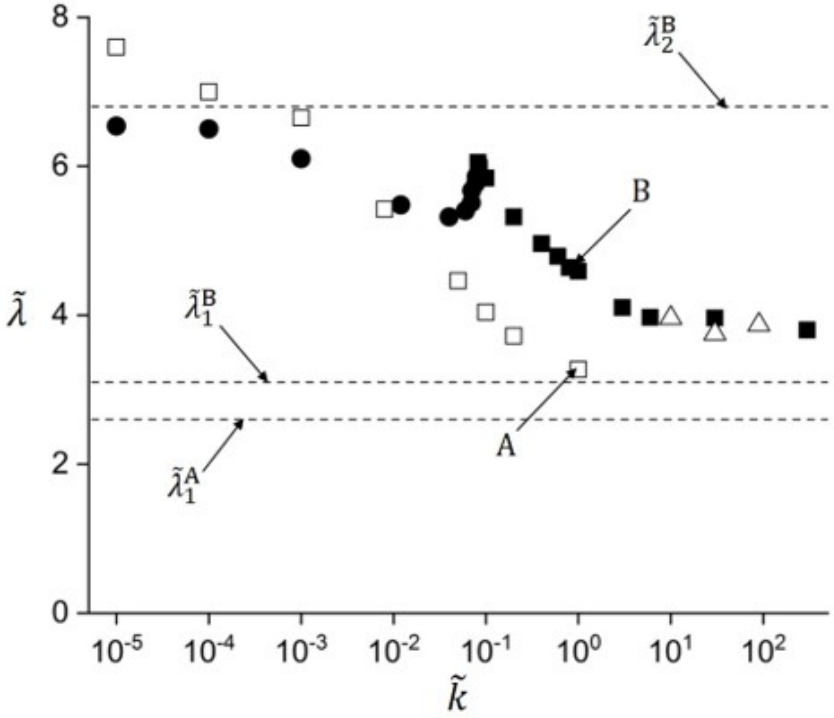

Figure 4.3: Turing pattern wavelength as a function of the growth-rate parameter $\tilde{k}$ in (Equation (4.11)). Hollow symbols [A] are for $R_D = 1/16$, $\tilde{c}_3 = 0.83$, $\tilde{v}_h = 0.3$ and solid symbols [B] are for $R_D = 3/40$, $\tilde{c}_3 = 1.0$, $\tilde{v}_h = 0.1$. In both cases, $\tilde{c}_4 = 0.5$, $\tilde{u}_0 = 1$ and $\tilde{Q} = 1$. Triangles identify cases leading to peak decay, whilst circles identify cases of peak splitting. Dashed lines represent bounds on wavelengths of stable patterns (see Appendix 4.A).

Figure 4.3 shows the wavelength of the resulting steady-state pattern as a function of the growth-rate parameter $\tilde{k}$ in (Equation (4.11)) for two sets of parameter values, A: [$R_D = 1/16$, $\tilde{c}_3 = 0.83$, $\tilde{v}_h = 0.3$] and B: [$R_D = 3/40$, $\tilde{c}_3 = 1.0$, $\tilde{v}_h = 0.1$]. The remaining parameters $\tilde{c}_4 = 0.5$, $\tilde{u}_0 = 1$ and $\tilde{Q} = 1$ are common to both cases. The dashed lines in Figure 4.3 represent the lower ($\tilde{\lambda}_1$) and upper ($\tilde{\lambda}_2$) bounds of the range of wavelengths of stable periodic

patterns obtained numerically, as discussed in Appendix 4.A. Notice that the upper bound for case [A] is approximately $\tilde{\lambda}_2^{\mathrm{A}} \approx 21$ so does not appear in Figure 4.3.

Case [A] corresponds to the ratio $\tilde{c}_4/R_D = 8$, which is well above the boundary for instability defined in (Equation (4.17)). At lower values of $\tilde{k}$, the wavelength generated at the moving front is retained in the steady state, and it decreases monotonically as $\tilde{k}$ is increased over five orders of magnitude. However, for $\tilde{k} > 1$ some of the peaks generated decay, leading to a larger steady-state wavelength, as discussed in Section 4.2.2.1 above. These results are indicated by triangles in Figure 4.3.

Case [B] corresponds to $\tilde{c}_4/R_D = 6.7$, for which a narrower range of wavelengths is stable in the steady state. The actual wavelength increases with decreasing $\tilde{k}$ down to $\tilde{k} \approx 0.1$, below which some of the generated peaks split into two through a transient process that we describe in more detail in Section 4.2.3.1, below. Steady-state patterns generated by peak splitting are indicated by circles in Figure 4.3. Notice that peak splitting occurs before $\tilde{h}_{\mathrm{period}}$ reaches values for which steady-state patterns are unstable. To elucidate this behaviour, we performed numerical simulations on a large fixed domain with periodic initial conditions of wavelength close to the upper boundary in Figure 4.3. Results show that the pattern converges on the steady state only if the initial distributions are very close to those in the steady state. With all other initial conditions, the system preferentially evolves towards a pattern with a different wavelength.

4.2.3.1 Peak-splitting

In the previous section, we noted that peak splitting causes the wavelength of the final pattern for case [B] to differ from that generated at the moving front as this wavelength approaches the upper boundary of the range of stable Turing patterns for certain parameter values. Figure 4.4 shows this evolutionary process for $\tilde{u}(\tilde{x}, \tilde{t})$ with $\tilde{k} = 1$. For instance, Figure 4.4(a) shows that at $\tilde{t} \approx 1475$, a peak develops rapidly near $\tilde{x} = 41$. The shape of this peak changes relatively slowly until $\tilde{t} \approx 1620$, at which time it starts to split into two

peaks. As these new peaks develop, they also move apart. The right peak moves to the right, and eventually stabilizes at $\tilde{x} \approx 40$, whilst the left peak moves a larger distance to the left, reaching the location $\tilde{x} \approx 47.5$. Such an event is observed to occur periodically. The corresponding influence on the motion of the boundary is shown in Figure 4.4(b). The initial peak development is associated with a large increase in boundary velocity $\dot{\tilde{h}}$ labelled 'strong transition' whilst the peak-splitting event gives only a minor perturbation in the velocity. Strong transitions are separated by a distance $2\tilde{\lambda}$, where $\tilde{\lambda}$ is the wavelength of resulting Turing pattern.

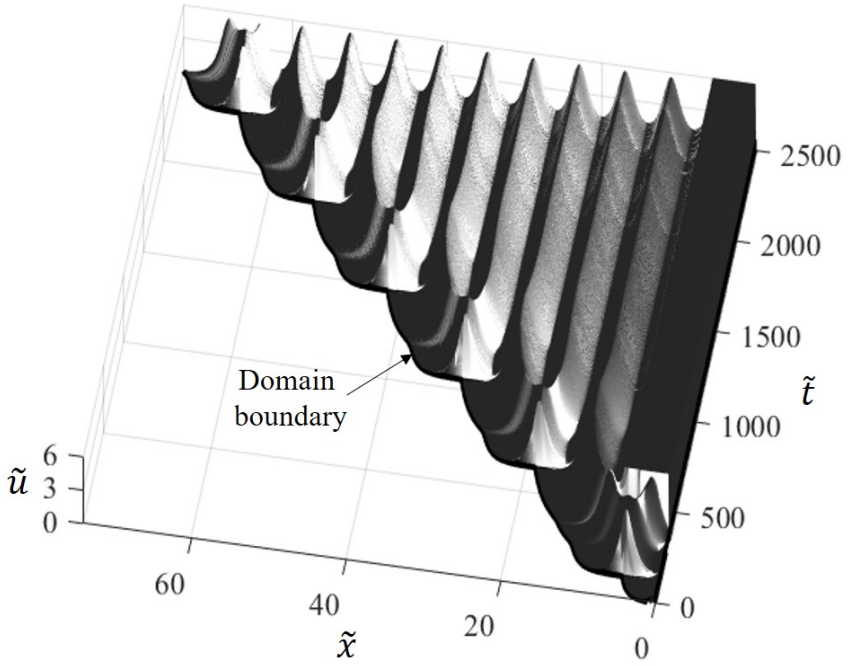

(a)

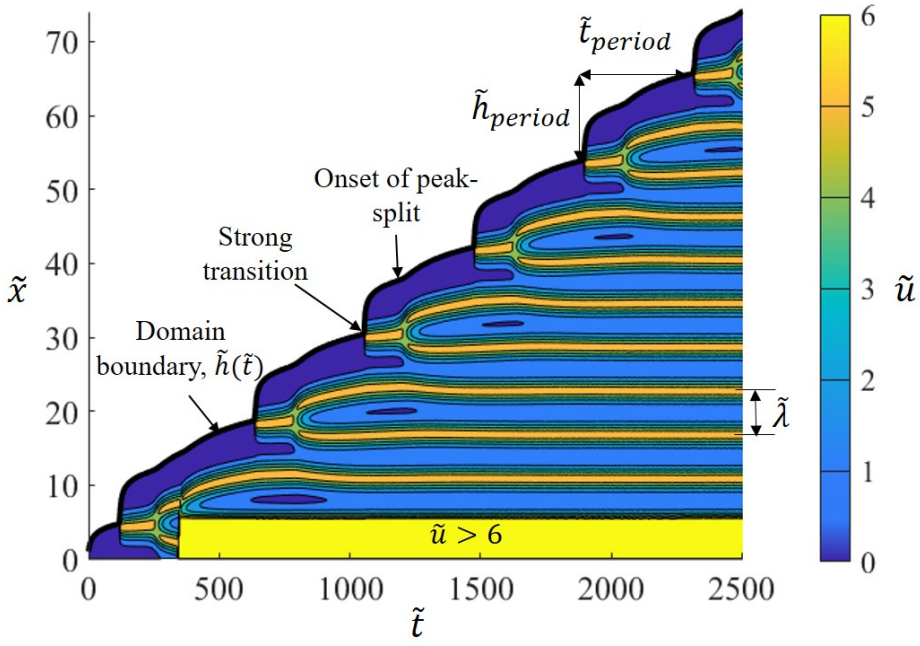

(b)

Figure 4.4: Periodic behaviour with peak-splitting: (a) Spatiotemporal evolution of the species $\tilde{u}$ showing each peak formed at the boundary splitting once. (b) Contours of $\tilde{u}$ showing a strong transition in the boundary kinetics for each peak formed at the boundary. The peaks farther away from the moving front are observed to be stationary with a wavelength of $\tilde{\lambda}$. Strong transitions are separated by a distance $\tilde{h}_{\text{period}} = 2\tilde{\lambda}$. Results are obtained using Gierer-Meinhardt activator (v)-inhibitor (u) kinetics with $\tilde{c}_4 = 0.5$, $R_D = 3/40$, $\tilde{c}_3 = 1$, $\tilde{u}_0 = 1$, $\tilde{v}_{\tilde{h}} = 0.01$, $\tilde{Q} = 1$ and $\tilde{k} = 1$.

The number of peaks that split in case [B] depends on the value of $\tilde{k}$ and appears to self-select a value that results in a wavelength well within the steady-state bounds. For example, the points shown in Figure 4.3 for case [B] as $\tilde{k}$ is decreased in the range $0.01 < \tilde{k} < 0.05$ include cases where (i) one out of four, or (ii) two out of every five peaks split, or (iii) each newly generated peak splits four times. In each case, the resulting pattern then adjusts as in Figure 4.4 to give a uniform spacing in the steady state.

At even lower values of $\tilde{k}$, a single peak is generated at the moving boundary when the process starts; thereafter, all subsequent peaks are generated by splitting the peak nearest the moving boundary. In this case, there are no strong transitions of the form shown in Figure 4.4(b), and the boundary kinetics are only slightly perturbed from linear.

These results are obtained using numerical simulations, and, hence, we can only investigate cases with particular parameter values. However, to give a broader picture of the system behaviour, Figure 4.5 presents a map in showing the dependence of qualitative features of the behaviour as functions of $\tilde{v}_h$ and $\tilde{c}_4$.

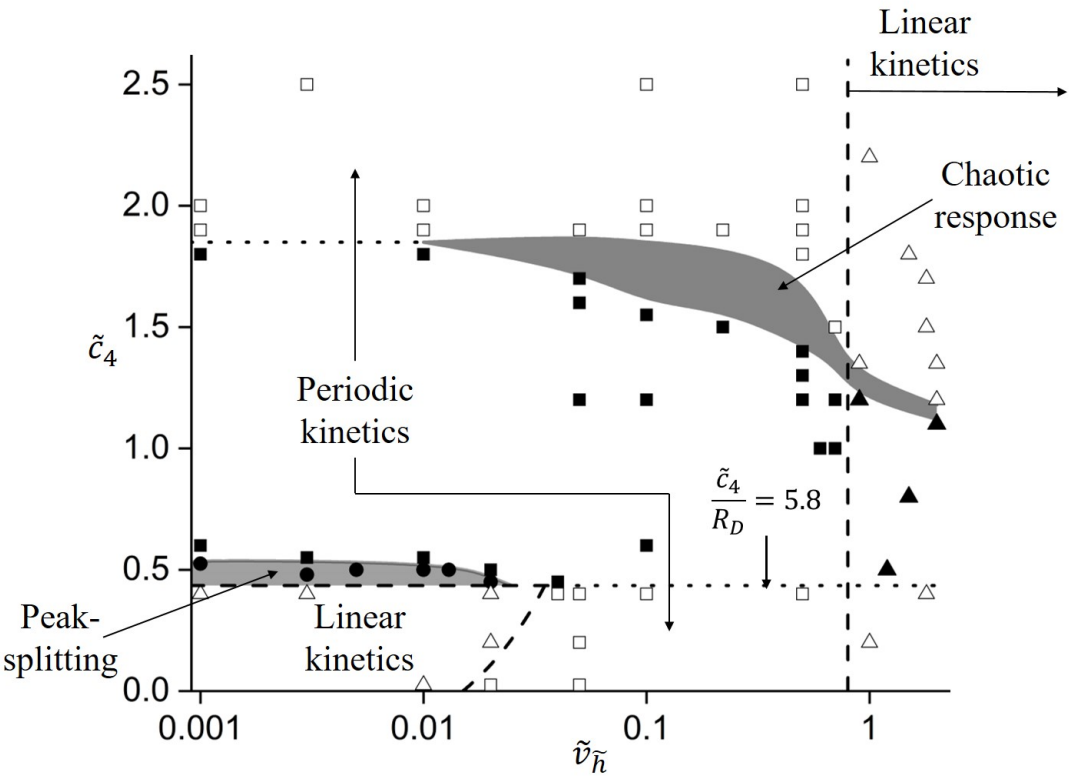

Figure 4.5: The solid symbols in this map indicate numerical simulations that resulted in pattern formation, and the open symbols indicate numerical simulations that did not result in pattern formation. The triangular symbols indicate conditions under which the boundary moved in a linear fashion, rather than in a periodic fashion. The lower shaded area, and the corresponding circular points, represent a region in which peak-splitting was observed. The upper shaded region represents where chaotic, random behavior was observed that was very sensitive with respect to small changes in the values of input parameters. The lower dotted line corresponds to the condition $\tilde{c}_4 = 5.8R_D$, which is the instability condition of (Equation (4.17)). These results were obtained using Gierer-Meinhardt activator (v)-inhibitor (u) kinetics with $R_D = 0.075$, $\tilde{c}_3 = 1$, $\tilde{u}_0 = 1$, $\tilde{Q} = 1$ and $\tilde{k} = 1$.

Figure 4.5 shows that while non-linear boundary kinetics of convex-up segments (as shown in Figure 4.1a) are observed for lower values of the activator concentration $\tilde{v}_{\tilde{h}}$, increasing it beyond ~ 1 results in a local build-up of the inhibitor concentration ($\tilde{u}$) at the moving front, which then moves linearly in response. For regions not satisfying the instability condition of (Equation (4.17)), i.e for $\tilde{c}_4 < 5.8R_D$, no patterns are observed. However, boundary kinetics still shows a periodicity for some of such cases. As we move away from this region by increasing $\tilde{c}_4$, a general trend of pattern formation, chaotic concentration

distribution, followed by no pattern formation, is observed. Notice that as the solution is numerical, this map does not provide any general conclusions for all parameter ranges, as opposed to a linear stability analysis [75, 76, 77]. However, as shown in Appendix 4.A, a linear stability analysis only provides a subset of wavelengths which form stable patterns in reaction-diffusion systems of Section 5.2.1 and Equation (4.26).

4.3 Activator-substrate system

We next consider Schnakenberg's activator-substrate the governing differential equations for which are as follows [54]

$$\frac{\partial u}{\partial t} = D_u \frac{\partial^2 u}{\partial x^2} - c_1 v^2 u + a \; ; \quad \frac{\partial v}{\partial t} = D_v \frac{\partial^2 v}{\partial x^2} + c_1 v^2 u - c_2 v + b \; . \tag{4.24}$$

We use the same boundary conditions and growth law (Equation (4.6)) as in the Geirer-Meinhardt model. A dimensionless formulation can then be obtained by defining

$$\tilde{u} = \mu u \; ; \;\; \tilde{v} = \mu v \; ; \;\; \tilde{x} = x\sqrt{\frac{c_2}{D_u}} \; ; \;\; \tilde{h} = h\sqrt{\frac{c_2}{D_u}} \; ; \;\; \tilde{t} = c_2 t \tag{4.25}$$

[59], where $\mu = \sqrt{c_1/c_2}$. Substituting these relations in (Equation (4.24)), we obtain the dimensionless governing (Equation (4.26)). [54], which can be described in the following dimensionless form

$$\begin{aligned} \frac{\partial \tilde{u}}{\partial \tilde{t}} &= \frac{\partial^2 \tilde{u}}{\partial \tilde{x}^2} + \tilde{a} - \tilde{v}^2 \tilde{u} \\ \frac{\partial \tilde{v}}{\partial \tilde{t}} &= R_D \frac{\partial^2 \tilde{v}}{\partial \tilde{x}^2} + \tilde{b} + \tilde{v}^2 \tilde{u} - \tilde{v} \; , \end{aligned} \tag{4.26}$$

where $\tilde{u}, \tilde{v}$ act as substrate and activator respectively, and $R_D \ll 1$. As in Section 2, we assume that the velocity of the moving front is determined by (Equation (4.11)), and the remaining boundary conditions by (Equation (4.12), Equation (4.13)). In this case, the

independent dimensionless parameters defining the system comprise

$$R_D = \frac{D_v}{D_u} \; ; \;\; \tilde{a} = \frac{\mu a}{c_2} \; ; \;\; \tilde{b} = \frac{\mu b}{c_2} \; ; \;\; \tilde{u}_0 = \mu u_0 \; ; \;\; \tilde{v}_h = \mu v_h \; ; \;\; \tilde{Q} = \mu Q \; ; \;\; \tilde{k} = \frac{k}{\sqrt{D_u c_1}} \; . \quad (4.27)$$

Figure 4.6 shows the response of the system for parameter values $R_D = 3/400, \tilde{a} = 0.9, \tilde{b} = 0.1, \tilde{u}_0 = 1, \tilde{v}_h = 0.1, \tilde{Q} = 1$ and $\tilde{k} = 0.05$. Troughs in the substrate concentration $\tilde{u}$ (Figure 4.6(a)), and simultaneous peaks in the activator concentration $\tilde{v}$ (Figure 4.6(b)), are developed periodically at the moving boundary. These events are associated with a transient reduction in domain growth rate, leading to the concave-upwards boundary kinetics, in contrast to the convex-upwards kinetics of the Gierer-Meinhardt model in Figure 4.1(a).

Figure 4.6 also shows that for these set of parameters, every second peak generated at the moving boundary splits. Also, the splitting process initiates when this peak is two peaks away from the boundary. The distribution, therefore, eventually converges on a stationary periodic pattern, with $\tilde{\lambda} = (2/3)\tilde{h}_{\text{period}}$.

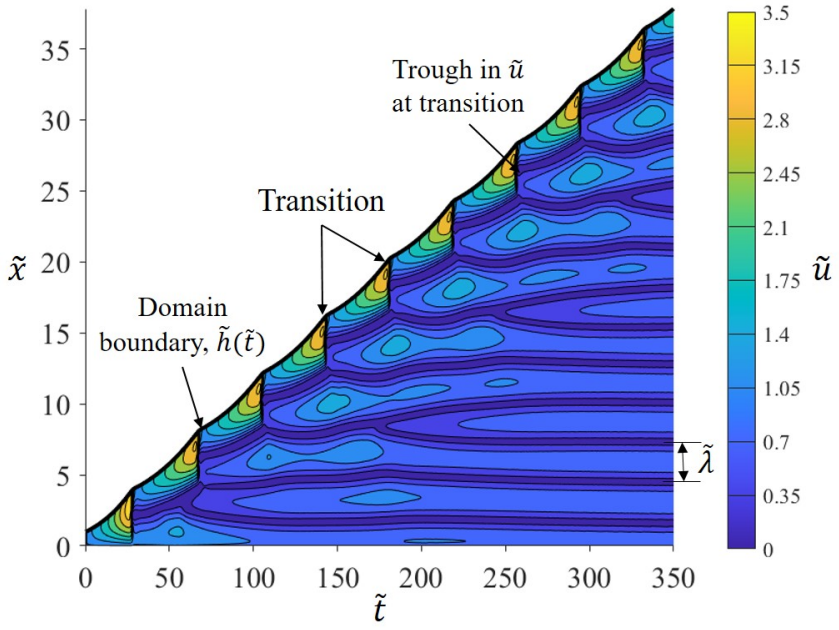

(a)

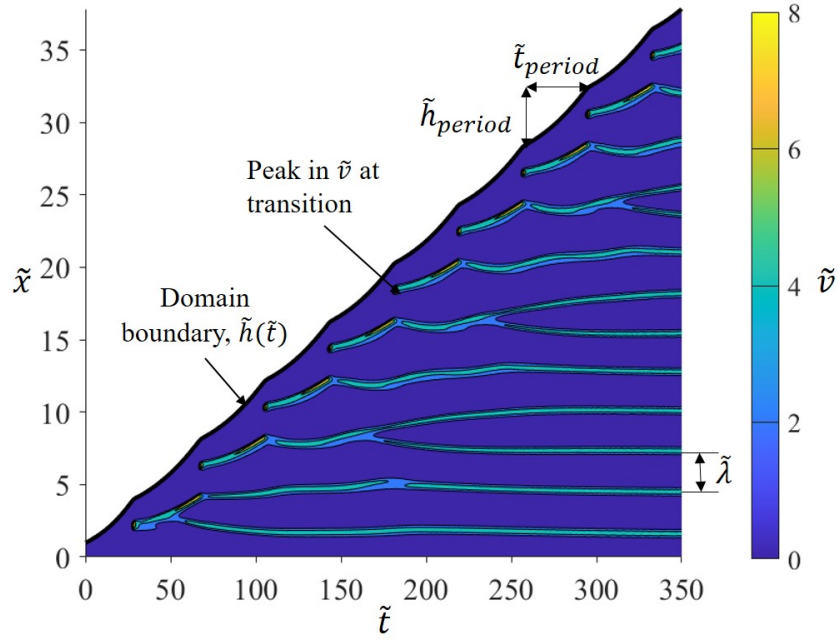

(b)

Figure 4.6: Behavior of Schnakenberg's activator-substrate model for $R_D = 3/400$, $\tilde{a} = 0.9$, $\tilde{b} = 0.1$, $\tilde{u}_0 = 1$, $\tilde{v}_h = 0.1$, $\tilde{Q} = 1$ and $\tilde{k} = 0.05$: (a) Contours of $\tilde{u}$ showing troughs developed at the boundary causing periodic transitions between concave-upward segments, in contrast with the convex-upwards behaviour in Fig. 1(b). (b) Contours of $\tilde{v}$ show every second peak formed at the boundary splitting. The peaks farther away from the moving front are observed to be stationary. Peaks in $\tilde{v}$ coincide with troughs in $\tilde{u}$. Transitions are separated by a distance $\tilde{h}_{\text{period}} = (3/2)\tilde{\lambda}$. $\tilde{x}$ is the distance from the fixed surface.

4.4 Conclusions

In this chapter, we have examined the interaction between pattern-forming Turing instabilities and a domain boundary whose motion is governed by the local concentration of one of the species. Results for both the Gierer-Meinhardt activator-inhibitor model [53] and the Schnakenberg activator-substrate model [54] show parameter ranges in which the velocity of the boundary is periodic, with the former exhibiting convex-upward segments and the latter concave-upward segments, in each case separated by rapid changes in velocity [transitions]. Both convex-upward [1, 70] and concave-upward kinetics [21] have been observed in experimental systems.

Periodic boundary motion leaves behind a spatially-periodic pattern, whose wavelength is determined by the mean velocity and the frequency of transitions. If this wavelength is one for which stable Turing patterns can exist in an infinite domain, the pattern will generally persist, but in other cases it may evolve through peak decay or peak splitting to a different [and stable] wavelength, or it may decay to a homogeneous state.

Appendix

4.A: Stationary solutions of the Gierer-Meinhardt model in fixed-domains

In this appendix, we discuss the numerical procedure for determining stable and unstable steady-states of the Gierer-Meinhardt model of Section 5.2.1 in a fixed domain. We achieve this using MATLAB's continuation and bifurcation package - pde2path [73, 74].

We use $\tilde{h}$ as the bifurcation parameter for analyzing the PDEs in Section 4.2.1 and Section 4.2.1, while neglecting the advection terms containing $d\tilde{h}/d\tilde{t}$ (i.e in a fixed domain $0 < \zeta < 1$ where $\zeta = \tilde{x}/\tilde{h}$). Zero-flux boundary conditions are used. For the purpose of demonstration, we show results for parameters of case [B] of Section 4.2.3 ($R_D = 3/40$, $\tilde{c}_3 = 1.0$, $\tilde{c}_4 = 0.5$) in Figure 4.7.

The trajectory of concentration of species $\tilde{u}$ is represented by its maximum absolute value,

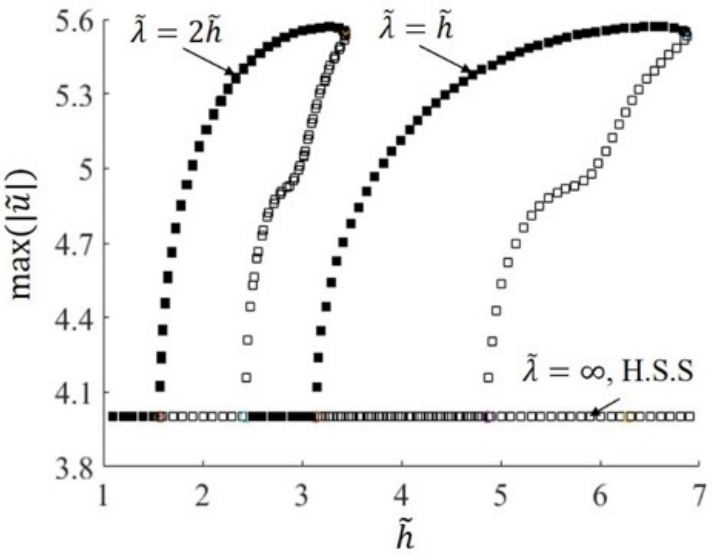

Figure 4.7: Bifurcation diagram for Gierer-Meinhardt activator (v)-inhibitor (u) kinetics with $R_D = 3/40$, $\tilde{c}_3 = 1.0$, $\tilde{c}_4 = 0.5$ (case [B] in Figure 4.3), assuming the domain to be fixed. Solid squares represent the stable steady-states while hollow squares mark the unstable steady-states, obtained under zero-flux boundary conditions. Stable patterns are obtained in the wavelength range of $3.1 < \tilde{\lambda} < 6.8$ (bounds $\tilde{\lambda}_1^{\mathrm{B}}, \tilde{\lambda}_2^{\mathrm{B}}$). H.S.S stands for the homogeneous-steady-state solution of Equation (4.15).

$\max(|\tilde{u}|)$. Solid and hollow squares represent the stable and unstable solutions, respectively. The horizontal branch at $\max(|\tilde{u}|) = 4$ corresponds to the homogeneous steady-state of Equation (4.15). The other two branches, $\tilde{\lambda} = 2\tilde{h}$ and $\tilde{\lambda} = \tilde{h}$, correspond to stationary periodic solutions, found to be stable in the range $3.1 < \tilde{\lambda} < 6.8$. Notice that the boundary conditions support solutions with an integer number of half-waves in the domain. Note that for this case, the homogeneous-steady-state is unstable to small perturbations with wavelengths in a significantly smaller range of $3.1 < \tilde{\lambda} < 4.8$. This shows that a linear stability analysis about the homogeneous solution gives only an imperfect guide to the range of wavelengths to be expected in a transient simulation.

For case [A] of Section 4.2.3, stable patterns in the range $2.6 < \tilde{\lambda} < 21$ were obtained using a similar procedure. Note that pde2path permits fairly general dependence of the coefficients on $\tilde{u}$, $\tilde{v}$ and ζ but not on time $\tilde{t}$, so it cannot be applied to the moving-boundary problem of Section 4.2.1,Section 4.2.1, even if the domain growth $\tilde{h}(\tilde{t})$ were specified or approximated.

Chapter 5

Candidate Mathematical Models for Zircaloy Oxidation

5.1 Introduction

Oxidation behavior of adherent oxides formed on majority of material systems is observed to follow an approximately parabolic oxidation kinetics. The oxidation rate drops continuously with time as the thickness of the protective oxide increases. Mathematical models for understanding this behavior are fairly well established and are discussed in the following sections.

5.1.1 Diffusion model of oxide growth

In this section, we present the classical understanding of the oxide growth based on Fickian diffusion. There are generally two types of oxidation systems, one in which the diffusivity of the metal ion is significantly larger than that of the oxidizing species (oxygen ion, hydroxide ion etc.) and therefore the new oxide forms primarily at the oxide-oxygen environment interface. In the second category, the oxidizing species diffuses faster and hence the new oxide is predominantly formed at the metal-oxide interface. Zirconium oxidation belongs to the second type, and therefore, we will only discuss this category in this chapter.

Figure 5.1 shows the schematic of an oxidation process, where the oxidizing species c diffuses from the oxygen environment side of the oxide to the metal side. Let us assume that the surface area of the metal-oxide interface is A. c_0, c_s is the concentration of the oxidizing

species on the oxide-oxygen environment interface and the metal-oxide interface respectively. c_0 is assumed to be constant. Also, constant B is the concentration of the oxidizing species in the metal oxide. h is the thickness of the oxide at time t. If the oxide grows by an amount dh in time dt, mass conservation at the moving metal-oxide interface is then given as

$$-D\frac{\partial c}{\partial x}Adt = (c_s + B)Adh \tag{5.1}$$

where $c_s Adh$ is the advection term. This can be simplified to

$$-D\frac{\partial c}{\partial x} = (c_s + B)\frac{dh}{dt} \tag{5.2}$$

Also, the rate of formation of the oxide is proportional to the rate of reaction between the oxidizing species and metal at the metal-oxide interface. At this location, the concentration of the metal is constant, we have

$$\frac{dh}{dt} = kc_s \tag{5.3}$$

where k is a constant. Equations (5.2) and (5.3) can be solved simultaneously for unknowns h and c_s. In the next section, we will discuss the approximations which lead to the Deal-Grove model of oxidation [72].

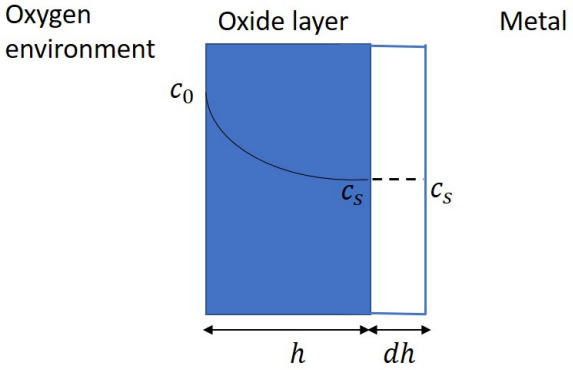

Figure 5.1: Growth of an oxide layer via diffusion of the oxidizing species (c) from the oxide-oxygen environment interface to the metal-oxide interface. The metal-oxide interface moves by an amount dh in time dt due to the formation of new oxide at the metal-oxide interface.

5.1.1.1 Deal-Grove model of oxidation

In the model proposed by Deal and Grove for oxidation of silicon [72], there are two main assumptions of (i) steady-state within the oxide and (ii) a negligible value of the advection term in Equation (5.2). These approximations simplify this equation to

$$D\frac{c_0 - c_s}{h} = B\frac{dh}{dt} \tag{5.4}$$

Substituting Equation (5.3) into the above equation, we get

$$c_s = \frac{c_0}{1 + \frac{Bkh}{D}} \tag{5.5}$$

We can solve for the oxide thickness by substituting this expression in Equation (5.3) to get

$$\left(1 + \frac{Bkh}{D}\right) dh = kc_0 dt \tag{5.6}$$

Integrating this equation and assuming 0 oxide thickness at time $t = 0$, we have

$$h = -\frac{D}{Bk}\left[-1 + \sqrt{1 + \frac{2Bk^2c_0}{D}t}\right] \tag{5.7}$$

If we non-dimensionalize h and t as follows

$$\tilde{h} = \frac{Bkh}{D}; \tilde{t} = \frac{2Bk^2c_0}{D}t, \tag{5.8}$$

the growth kinetics can be written as

$$\tilde{h} = (1 + \tilde{t})^{\frac{1}{2}} - 1 \tag{5.9}$$

and is plotted in Figure 5.2. We observe two regimes of kinetics for the Deal-Grove model. For shorter times, $\tilde{t} << 1$, we have the following approximation

$$\tilde{h} = \tilde{t}/2 \tag{5.10}$$

which corresponds to a linear growth kinetics. For significantly larger times, $\tilde{t} >> 1$, we get

$$\tilde{h} = \tilde{t}^{1/2} \tag{5.11}$$

which is the parabolic rate of growth. Therefore, the growth kinetics is initially linear, controlled by the reaction kinetics, and transitions to a diffusion-limited parabolic regime which is its limiting behavior. From the non-dimensionalization in Equation (5.8), it follows that higher the value of the reaction constant k is with respect to the diffusion coefficient D, the sooner this transition occurs on actual time scale.

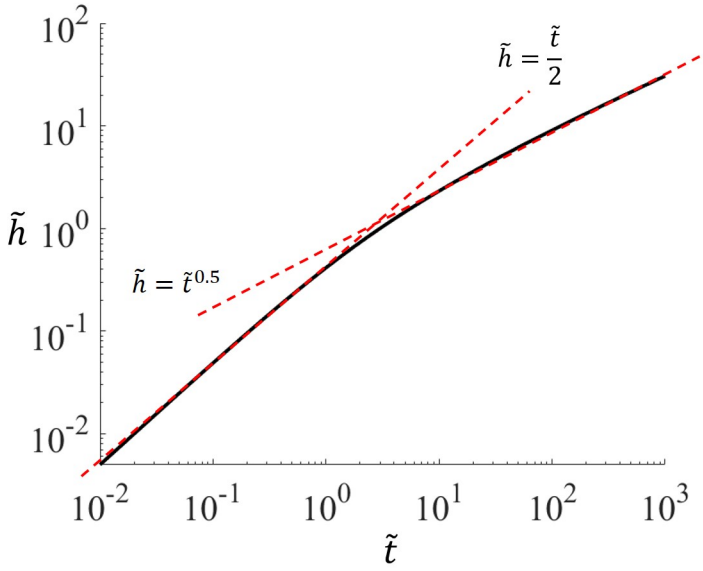

Figure 5.2: Deal-Grove model of oxidation. Oxidation kinetics is limited by the reaction kinetics in the initial stages of oxidation $\tilde{t} << 1$. As the oxide layer thickens, the process becomes limited by diffusion, leading to a parabolic behavior.

5.1.2 Wagner's electrochemical-migration model of oxide growth

In Wagner's theory, the oxidation process is considered to be controlled by the migration of charged species through the oxide layer, under the effect of concentration gradients and an electric field. The oxide layer formed on Zircaloys is generally considered to be anion-deficient [1], with diffusion of oxygen controlled by the diffusion of anion (oxygen) vacancies. Figure 5.3 shows the schematic of interface reactions and the diffusion of charged species through the oxide. At the metal-oxide interface, zr metal reacts with the lattice oxygen of the sub-stoichiometric zirconia to form new oxide, positively charged oxygen vacancies and electrons. The doubly-charged vacancies and electrons then diffuse to the other side of the oxide, where they react with free oxygen to form neutral lattice oxygen ($O_o^{\times\times}$).

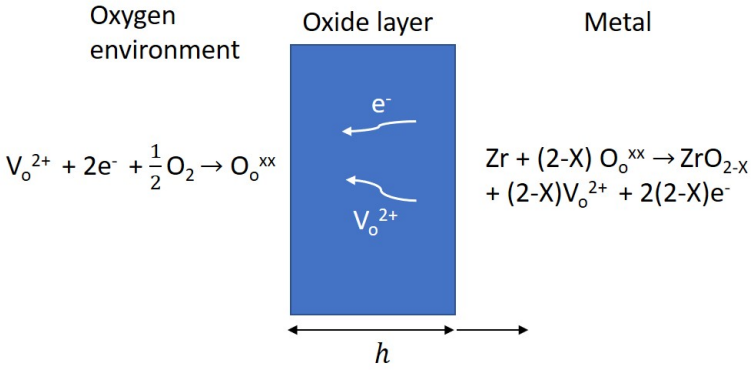

Figure 5.3: Growth of an anion-deficient oxide layer by reaction with the lattice oxygen at the metal-oxide interface. Positively charged anion-vacancies and electrons diffuse to the free surface of the oxide.

Governing differential equations for oxygen-vacancy concentration (v) and electron density (n) can be written as

$$\frac{\partial v}{\partial t} = D_v \frac{\partial^2 v}{\partial x^2} - \mu_v \frac{\partial}{\partial x}(vE)\ ; \quad \frac{\partial n}{\partial t} = D_n \frac{\partial^2 n}{\partial x^2} - \mu_n \frac{\partial}{\partial x}(nE)\ . \tag{5.12}$$

where E is the electric field, μ_v, μ_n is the electric mobility of the vacancies and the electrons respectively, while D_v, D_n are the corresponding diffusivity values. Coupled-current

condition requires the net current to be 0 at every point within the film, i.e

$$2\frac{\partial v}{\partial t} - \frac{\partial n}{\partial t} = 0 \tag{5.13}$$

Substituting Equation (5.12) into this equations and integrating it, we can obtain an expression for the electric field as

$$E = \frac{2D_v \frac{\partial v}{\partial x} - D_n \frac{\partial n}{\partial x}}{2\mu_v v - \mu_n n} \tag{5.14}$$

If we assume local electroneutrality, i.e, $n = 2v$, the system can be reduced to one independent governing equation

$$\frac{\partial v}{\partial t} = D_v \frac{\partial^2 v}{\partial x^2} - \frac{D_v(D_v - D_n)}{D_v + \frac{D_n}{2}} \frac{\partial^2 v}{\partial x^2} \tag{5.15}$$

which is equivalent to Fick's second law of diffusion with a modified diffusion coefficient of

$$D_v^{ecm} = D_v - \frac{D_v(D_v - D_n)}{D_v + \frac{D_n}{2}} \tag{5.16}$$

for electrochemical migration of oxygen vacancies in an electroneutral oxide film. A consequence of reducing to a Fickian form is that it results in an oxidation kinetics that has a parabolic limiting behavior (same as in the classical diffusion model of previous section). Also notice that if $D_n = D_v$, the electric field $E = 0$ and the model reduces to the classical diffusion model of Section 5.1.1. A numerical simulation with a less restrictive condition of only the interfaces specified to be charge-neutral also results in a local state of electroneutrality in its limiting behavior.

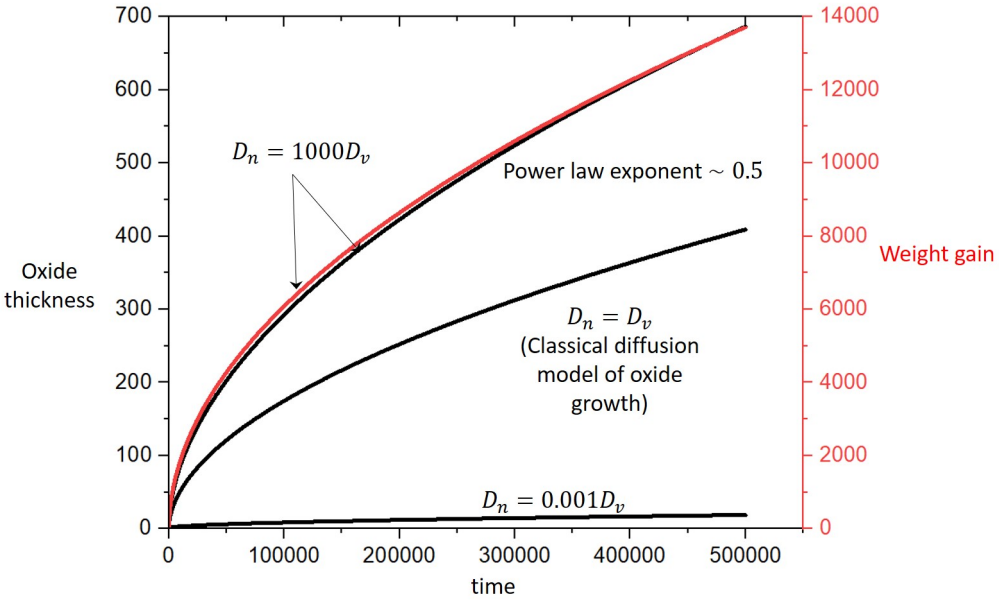

Figure 5.4: Growth kinetics of a locally-electroneutral oxide film obtained from Wagner's theory of electrochemical migration. Limiting behavior is observed to be approximately parabolic. For the case of equal diffusivity of electrons and oxygen vacancies, $D_n = D_v$, electric field contribution is 0 (Equation (5.16)), reducing it to the classical diffusion model of Section 5.1.1. Weight-gain kinetics is only shown for the case $D_n = 1000D_v$.

5.1.3 Zircaloy oxidation: Departing from classical models

For oxidation in zirconium alloys, the initial growth kinetics follows the classical behavior of an approximately parabolic oxidation kinetics outlined in previous sections. However, as the oxide layer reaches a critical thickness, the weight-gain kinetics shows a sudden acceleration (a transition) as shown in Figure 5.5, while the oxide layer remains adherent and no through-thickness cracking is observed. Transition in the oxidation kinetics is also associated with the formation of void-like structures at the metal-oxide interface. After a transition, oxidation rate starts dropping again following an approximately parabolic kinetics, until another transition occurs when oxide layer reaches double of the critical thickness. This process is observed to repeat itself a few times. The microscopic analysis of thick oxide layers shows a periodic structure of the oxide, wherein each sub-layer is of the size that is equal to the critical thickness for transition. These sub-layers are observed to be separated by void-like

structures.

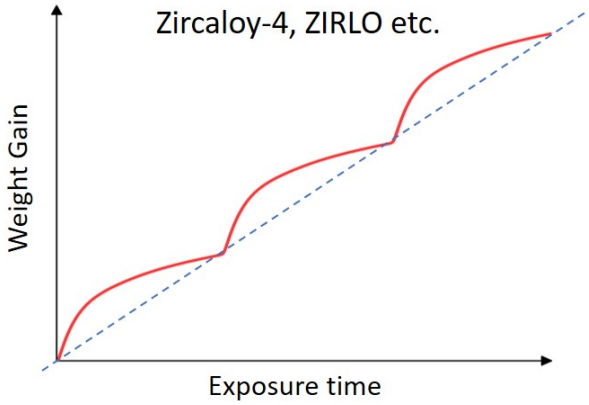

Figure 5.5: Schematic of periodic weight-gain kinetics observed during oxidation of Zr alloys such as Zircaloy-4 and ZIRLO (reproduced from [1]).

The peculiarity observed in the behavior of zirconium alloys is a significant departure from the predictions of classical oxidation models outlined in the previous sections. Therefore, in this chapter, we aim to present mathematical models which can further our understanding of mechanisms which cause this anomaly.

5.2 Turing models for periodic oxidation behavior

Detailed studies of observed periodicity in the grain structure of oxide formed on Zircaloys indicate that the boundary kinetics should replicate the behavior simulated in Figure 4.1 of chapter C:ch4. Furthermore, there is some literature on direct thickness measurement in zirconium alloys, showing periodicity in the oxidation kinetics during the initial stages of the oxidation [11]. However, there is a large set of studies in the literature for alloys oxidation (including zirconium, Ni-Cr and titanium alloys), which only monitor the weight of the sample during oxidation and report at least a few initial periodic occurrences of transitions (rapid acceleration) in the weight-gain kinetics [19, 20, 21]. Furthermore, transitions observed in the weight-gain [at least for the case of Zircaloys] exhibit a strong correlation with the ones observed in the boundary kinetics, as well as with the periodicity in the grain structure.

Turing models presented in the previous chapter exhibited a periodicity only in the rate of

the boundary movement, but not in the weight-gain kinetics. This is because the activator-inhibitor and the activator-substrate models considered there do not ensure conservation of either of the species involved in forming patterns. Therefore, in this section, we propose two modifications of these models, which exhibit transitions in the weight-gain kinetics as well as the boundary kinetics. In the first class of proposed systems, transitions in the weight-gain kinetics are due to a reaction that occurs at the metal-oxide interface, while in the second category, it is due to a reaction that takes place at the free surface (or the oxide-oxygen environment interface). These models also ensure conservation of the species that controls the rate of boundary movement.

5.2.1 Weight-gain controlled by metal-oxide interface reaction

For this category of systems, we modify the activator-inhibitor model of eqns. G-M to include a third diffusing species p which corresponds to the concentration of the species responsible for oxidation (e.g oxygen ion). The system is then governed by the following dimensionless equations

$$\begin{aligned} \frac{\partial \tilde{p}}{\partial \tilde{t}} &= R2_D \frac{\partial^2 \tilde{p}}{\partial \tilde{x}^2} && (5.17) \\ \frac{\partial \tilde{u}}{\partial \tilde{t}} &= \frac{\partial^2 \tilde{u}}{\partial \tilde{x}^2} - \tilde{u} + \tilde{v}^2 \\ \frac{\partial \tilde{v}}{\partial \tilde{t}} &= R_D \frac{\partial^2 \tilde{v}}{\partial \tilde{x}^2} + \tilde{c}_3 \frac{\tilde{v}^2}{\tilde{u}} - \tilde{c}_4 \tilde{v} && (5.18) \end{aligned}$$

where $R2_D = D_p/D_u$. D_p is the diffusion coefficient of the species p. u and v are the species which form Turing patterns same as in C:ch4. Species u is assumed to act as a catalytic substance for the chemical reaction that occurs between the corrosive species p and the underlying metal at the metal-oxide interface. For example, there is some evidence of interface crystal defects causing an improved reactivity in the oxide films [78]. The rate of

movement of this interface can then be written as

$$\frac{d\tilde{h}}{d\tilde{t}} = \tilde{k}\tilde{u}(1,\tilde{t})\tilde{p}(1,\tilde{t}) \ . \tag{5.19}$$

Boundary conditions for species u and v are taken as

$$\frac{\partial\tilde{u}}{\partial\zeta}(0,\tilde{t}) = 0 \ ; \ \ \frac{\partial\tilde{v}}{\partial\zeta}(0,\tilde{t}) = 0 \ ; \ \ \tilde{v}(1,\tilde{t}) = \tilde{v}_h \ ; \quad -\frac{\partial\tilde{u}}{\partial\zeta}(1,\tilde{t}) = \tilde{h}\left[\tilde{u}(1,\tilde{t})\right]\frac{d\tilde{h}}{d\tilde{t}} \ . \tag{5.20}$$

and the corrosive species p has the following boundary conditions

$$\tilde{p}(0,\tilde{t}) = p_0 \ ; \ \ -\frac{\partial\tilde{p}}{\partial\zeta}(1,\tilde{t}) = \tilde{h}\left[\tilde{p}(1,\tilde{t}) + \tilde{Q}\right]\frac{d\tilde{h}}{d\tilde{t}} \ . \tag{5.21}$$

Here, we have assumed that the flux of species u and v is zero at the free surface of the oxide, i.e, these species neither enter nor leave the system. $\tilde{Q}$ represents the amount of $\tilde{p}$ consumed per unit area in moving the boundary through a unit distance. Notice that the species $\tilde{u}$ acts only as a catalyst for the process that drives the boundary motion and hence does not get consumed in this process. Also, we assume that the weight-gain in the system is only because of the influx of the corrosive species p at the free surface, i.e

$$\Delta\widetilde{W} = \int_0^{\tilde{t}} -\frac{1}{\tilde{h}}\frac{\partial\tilde{p}}{\partial\zeta}(0,\tilde{t})d\tilde{t}, \tag{5.22}$$

where

$$\Delta\widetilde{W} = \frac{D_p}{c_1}\sqrt{\frac{c_2}{D_u}}\Delta W. \tag{5.23}$$

If p is assumed to be the mass of the oxidizing species per unit volume of the oxide, ΔW will be the weight gain per unit area of the oxidation surface. Figure 5.6 shows the boundary movement and weight-gain kinetics of this model for two values of the reaction constant $\tilde{k} = 0.01$ for case (a) and $\tilde{k} = 1$ for case (b), keeping all the other parameters the same and equal to $\tilde{c}_4 = 0.5$, $R_D = 3/40$, $\tilde{c}_3 = 1$, $\tilde{u}_0 = 1$, $\tilde{v}_{\tilde{h}} = 0.1$, $\tilde{Q} = 1$ and $\tilde{k} = 1$, $R2_D =$

100. Peaks in the concentration of u develop periodically, in a similar way as discussed in Section 4.2.2.1. This results in periodic acceleration of the rate of boundary movement (refer Equation (5.19)). Consequently, there are periodic increases in the consumption of species p (see Equation (5.21)). If the diffusivity of p is significantly higher as compared to the reactivity constant (k), this will lead to almost immediate corresponding transitions in the weight-gain kinetics as well, as shown in Figure 5.6(a). For relatively smaller diffusivity values, transitions in the weight-gain kinetics will follow the transitions in the boundary kinetics with a larger time delay, as shown in Figure 5.6(b). The underlying kinetics follows the physics of the Deal-Grove model of oxidation [72], wherein the initial kinetics is linear (reaction-limited) and the long-term kinetics is parabolic (diffusion-limited). Higher values of the reaction constant $\tilde{k}$ will make the transition from the linear to parabolic regime to occur on a relatively shorter timescale, as observed in Figure 5.6. Species u and v will form stationary patterns as shown in Section 4.2.2.1.

5.2.1.1 Comparison with Zircaloy oxidation behavior

For oxidation in zirconium alloys, the weight-gain kinetics has been observed to exhibit only $2-3$ initial transitions, whereas the structure of the oxide has been found to be periodic even up to ≈ 20 sublayers [3] (or ≈ 20 transitions in the boundary kinetics given that the new oxide forms at the metal-oxide interface). In that view, behavior shown in Figure 5.6(b) seems more appropriate for this particular application. Notably, the weight-gain kinetics is never observed to become parabolic in the experiments, and is rather observed to remain linear, unlike the behavior shown in Figure 5.6(b). However, this might just be a consequence of significantly high diffusivity of oxygen ions through the oxide layer keeping the oxidation kinetics in the linear regime for an extended duration of time. As the oxide layer formed on zirconium alloys remains intact, devoid of any through-thickness cracks, the kinetics is expected to be limited by diffusion or parabolic in nature for a large enough oxide thickness.

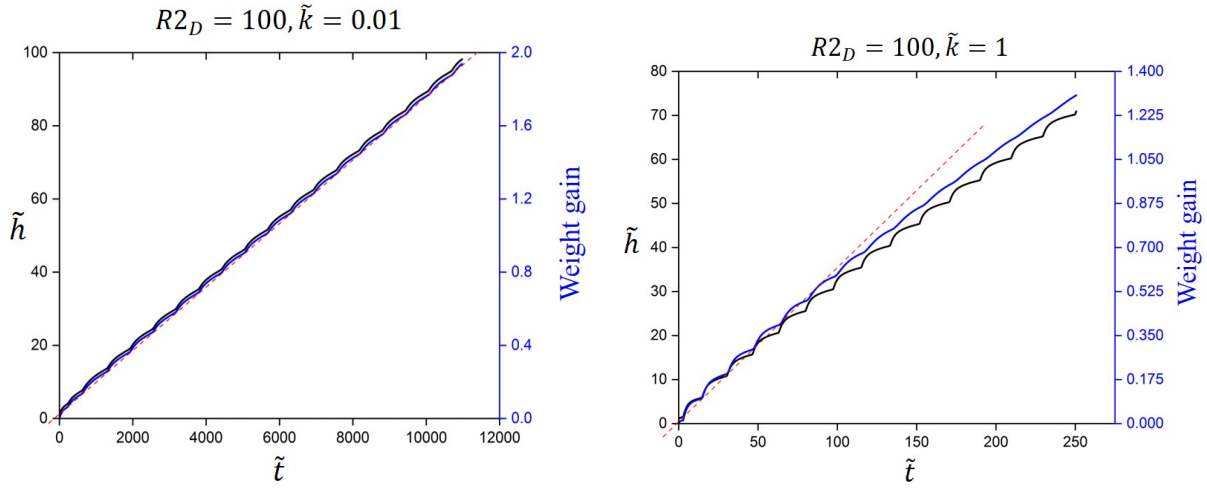

(a) (b)

Figure 5.6: Behavior of the modified Turing model outlined in Section 5.2.1 showing transitions in the weight-gain kinetics, as well as in the boundary motion kinetics, for (a) $\tilde{k} = 0.01$ and (b) $\tilde{k} = 1$ (refer Equation (5.19) for the description of this constant). Other parameter values are $\tilde{c}_4 = 0.5$, $R_D = 3/40$, $\tilde{c}_3 = 1$, $\tilde{u}_0 = 1$, $\tilde{v}_{\tilde{h}} = 0.1$, $\tilde{Q} = 1$ and $\tilde{k} = 1$, $R2_D = 100$.

5.2.2 Weight-gain controlled by oxide-oxygen environment interface reaction

For this category of models, species u, v, and the oxidation species p are assumed to be governed by the same differential equations as in Section 5.2.1. Boundary conditions for species $\tilde{u}$ and $\tilde{v}$ are

$$\frac{\partial \tilde{u}}{\partial \zeta}(0,\tilde{t}) = hA \; ; \quad \tilde{v}(0,\tilde{t}) = \tilde{v}_0 \; ; \quad \frac{\partial \tilde{v}}{\partial \zeta}(1,\tilde{t}) = \tilde{h}\left[\tilde{v}(1,\tilde{t})\right]\frac{d\tilde{h}}{d\tilde{t}} \; ; \quad \tilde{u}(1,\tilde{t}) = \tilde{u}_h \; . \tag{5.24}$$

and the corrosive species p has the following boundary conditions

$$-\frac{\partial \tilde{p}}{\partial \zeta}(0,\tilde{t}) = k_2\tilde{u} \; ; \quad -\frac{\partial \tilde{p}}{\partial \zeta}(1,\tilde{t}) = \tilde{h}\left[\tilde{p}(1,\tilde{t}) + \tilde{Q}\right]\frac{d\tilde{h}}{d\tilde{t}} \; . \tag{5.25}$$

where k_2 is a reaction constant. Species $\tilde{u}$ affects the rate of reaction that controls the influx of oxygen ion at the oxide-environment interface. This species also has a sink of constant strength A at the oxide-oxygen environment interface. If the oxide layer is anion-deficient,

the influx of oxygen at this location will likely be controlled by the following chemical reaction (see Figure 5.3)

$$\mathrm{V_O}^{2+} + 2\mathrm{e}^- + 1/2\mathrm{O}_2 \rightarrow O_{\mathrm{O}}{}^{\times\times}$$

where $\mathrm{V_O}^{2+}$ is positively charged oxygen vacancies and $\mathrm{O_O}^{\times\times}$ is the lattice oxygen in zirconia. Therefore, species $\tilde{u}$ can be oxygen vacancies, electrons, or other interface defects [78]. We assume the form of rate of boundary movement as follows

$$\frac{d\tilde{h}}{d\tilde{t}} = \tilde{k}\tilde{v}(1,\tilde{t})\tilde{p}(1,\tilde{t}) \ , \tag{5.26}$$

where species $\tilde{v}$ catalyzes the reaction responsible for the movement of the metal-oxide interface. Weight-gain is calculated same as in Equation (5.22).

The results for this model for parameter values of $\tilde{c}_4 = 0.5$, $R_D = 0.009$, $\tilde{c}_3 = 1$, $A = 0.1$, $\tilde{v}_0 = 2$, $\tilde{u}_h = 4$, $\tilde{Q} = 1$ $\tilde{k} = 0.1$, $\tilde{k_2} = 2$, $R2_D = 1$ are shown in Figure 5.7. In this system, peaks in $\tilde{u}$ and $\tilde{v}$ develop at the oxide-water interface, causing a strong transition in the weight-gain kinetics as shown in Figure 5.7(a) and a weak transition in the boundary kinetics Figure 5.7(b). This is because transition in the boundary kinetics requires diffusion of $\tilde{v}$ from this newly formed peak. This is shortly followed by the formation of peak in $\tilde{v}$ and $\tilde{u}$ at the moving front, causing a strong transition in the boundary kinetics and a slight deceleration of the weight-gain rate. However, it is only the peaks formed at the metal-oxide interface which persist. Therefore, transitions in the weight-gain kinetics are not equally spaced in time.

5.2.2.1 Comparison with Zircaloy oxidation behavior

For the model presented above, the time interval between two successive transitions in the weight-gain kinetics does not remain constant, instead it increases as the time proceeds. The underlying kinetics remains linear though, as observed during oxidation of Zircaloys. Consequently, the weight gain between two successive transitions remains proportional to

the time between two transitions. Notably, unlike the behavior observed for this model, only a few initial transitions are observed in the weight-gain kinetics of zirconium oxidation. The boundary kinetics shows an underlying parabolic kinetics, where each transition is successively delayed, but the distance traversed between two transitions remains approximately the same. Therefore, it can still result in a spatially periodic grain structure within the oxide.

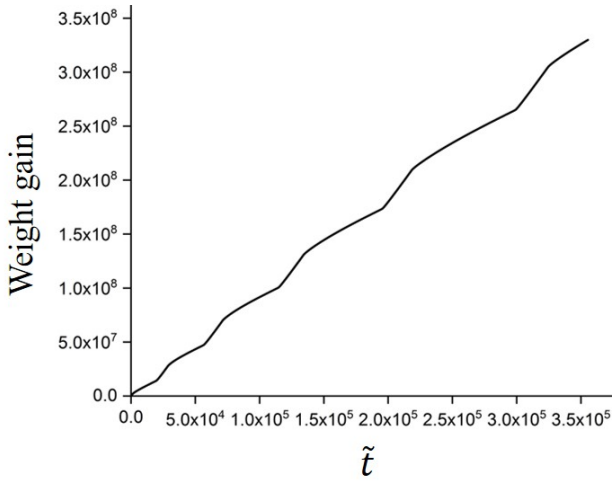

(a)

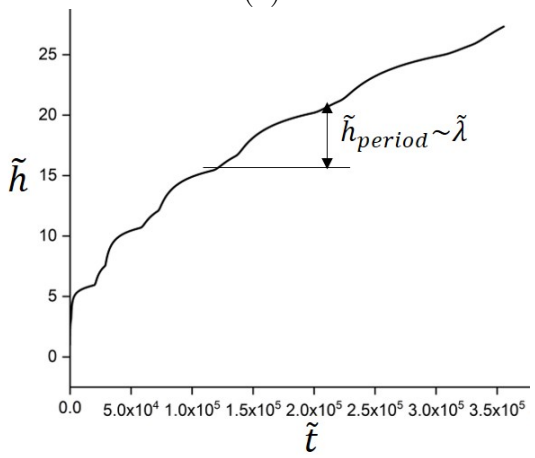

(b)

Figure 5.7: Behavior of the modified Turing model of Section 5.2.2 for parameter values of $\tilde{c}_4 = 0.5$, $R_D = 0.009$, $\tilde{c}_3 = 1$, $A = 0.1$, $\tilde{v}_0 = 2$, $\tilde{u}_h = 4$, $\tilde{Q} = 1$ $\tilde{k} = 0.1$, $\tilde{k_2} = 2$, $R2_D = 1$, showing transitions in the (a) weight-gain kinetics, as well as in the (b) boundary motion kinetics.

5.2.3 Proposed activator-inhibitor species in oxide films

Notice that species $\tilde{v}$ is a self-activator or an auto-catalytic substance. Dislocations form one of the obvious candidate for this species, due to their capability for self-multiplication (through Frank-read sources). However, presence of dislocations in the oxide layers is not unique to zirconium alloys, and is hence unlikely to be the cause of the peculiar oxidation behavior of these materials. Notably, martenstic phase transformations are postulated to be auto-catalytic in nature when they occur via an isothermal mode [79]. This is because the shear strain induced by a transforming cell reduces the strain-energy barrier for the transformation in the adjacent regions. In the oxide films formed on zirconium, tetragonal phase of the oxide undergoes a transformation to the monoclinic phase. Though this transformation is generally assumed to be athermal (independent of thermal motion) in nature, it is difficult to make a definitive claim about the effect of temperature in driving this phase transformation in the zirconium oxide layers. Therefore, in this section we will assume the phase transformation to occur via thermal nucleation and explore the auto-catalytic features of the corresponding system.

5.2.3.1 Thermal nucleation of monoclinic oxide

In this section, we will assume that nuclei of the monoclinic oxide develop in the tetragonal grains of the oxide due to thermal fluctuations. The shape of these nuclei is assumed to be an oblate-spheroid, with one of the dimensions equal to the length of the grain in the direction of the oxide-growth. The in-plane dimension is a, as shown in Figure 5.8. The choice of the shape of the nuclei is motivated by the strain-energy barrier analysis of this transformation in C:ch3, i.e shapes with their larger dimension across the direction of oxide growth offer an energetic advantage by reducing the macroscopic deformation due to the shear eigen-strain.

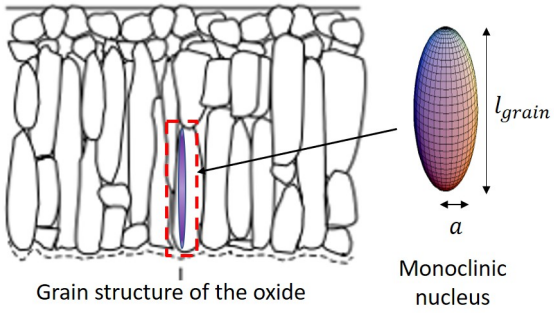

Figure 5.8: Assumed shape of a thermally-nucleated monoclinic oxide in a grain of the tetragonal oxide.

Critical size of the nuclei can be obtained by minimizing the total change in free energy with respect to this parameter by setting

$$\frac{d\Delta G}{da} = \frac{d(\Delta G_{T\rightarrow M} V_{nucleus})}{da} = 0 \tag{5.27}$$

where term $\Delta G_{T\rightarrow M}$ is the free energy change per unit volume of Equation (3.3). $V_{nucleus}$ is the volume of the nucleus. The critical size of nuclei hence obtained is referred to as a_c. The number of nuclei formed per unit time, per unit volume of the parent (tetragonal) phase is then given as

$$I = K(T) \exp - \frac{\Delta G^* + \Delta G_m}{kT} \tag{5.28}$$

where ΔG^* is the net change in free energy for a critical size nuclei, as shown in Figure 5.9. ΔG_m is the migration barrier.

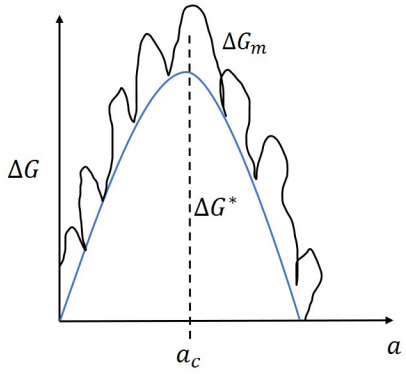

Figure 5.9: Energy landscape with respect to the size of the nucleus.

The rate of formation of new nuclei with this energy barrier is then given as

$$\frac{dn}{dt} = K(T)V_{grain}(1-f)\exp -\frac{\Delta G^* + \Delta G_m}{kT} \tag{5.29}$$

where f is the current volume fraction of the already transformed material. However, this expression is only valid for the case when the energy barrier of all the nuclei forming at a given time is the same. For tetragonal-to-monoclinic phase transformation in zirconia, the shear deformation associated with the formation of one nuclei will reduce the strain energy barrier for new nuclei forming in its immediate vicinity. Therefore, we assume a scenario outlined in Figure 5.10.

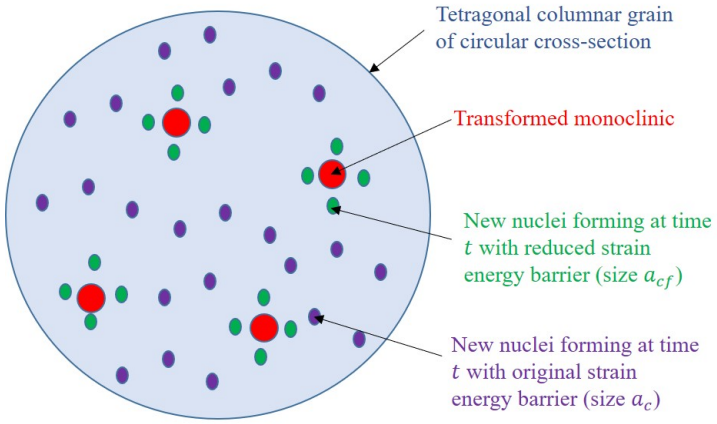

Figure 5.10: 2D view of a tetragonal grain in a plane parallel to the metal-oxide interface.

Figure 5.10 shows a planar view of a tetragonal grain parallel to the metal-oxide interface, with a length of l_{grain} into the plane of the paper. Inner smaller circles represent the transformed monoclinic. Red circles are the already transformed monoclinic up to time t. Green circles are the nuclei forming at time t in the immediate vicinity of the transformed monoclinic, and thus have a reduced strain energy barrier (and their critical nuclei size is a_{cf}). The nuclei forming far away (purple circles) form at the original energy barrier of $(\Delta G^* + \Delta G_m)$. Assuming that the already transformed monoclinic will reduce the energy barrier in the f fraction of the parent phase volume, and that the contribution of growth is negligible in increasing the monoclinic phase fraction, its rate of increase can be written as

$$\frac{df}{dt} = \frac{V_o \frac{dn_o}{dt} + V_r \frac{dn_r}{dt}}{V_{grain}} \tag{5.30}$$

where V_o is the volume of the critical nuclei forming far away from the existing monoclinic and n_o is their number. V_r is the volume of the critical nuclei forming in the vicinity and n_r is their number. This can also be written as

$$\frac{df}{dt} = \frac{2}{3}\pi l_{grain} K(T) \left[(1-f)a_c^2 + f a_{cf}^2 \exp\frac{\Delta G_r}{kT}\right] \exp -\frac{\Delta G^* + \Delta G_m}{kT} \tag{5.31}$$

ΔG_r is the reduction in the transformation barrier for the green nuclei of Figure 5.10 as compared to the purple nuclei. Note that $a_{cf} < a_c$ due to the reduced energy barrier for the former. Therefore, the auto-catalytic effect is present if

$$\exp\frac{\Delta G_r}{kT} > \left(\frac{a_c}{a_{cf}}\right)^2 \tag{5.32}$$

Therefore, based on Equation (5.31)-Equation (5.32), we can say that the monoclinic phase is a reasonable candidate for an auto-catalytic species. Oxygen vacancies tend to favor the tetragonal phase and will naturally provide the effect of cross-inhibition on the monoclinic phase by increasing the energy barrier for the transformation (ΔG^*). They can also self-

inhibit by reacting with the oxygen ions. However, we cannot make any definitive claims on the presence of a cross-activation effect, i.e, an increase in the monoclinic phase fraction accelerating the rate of production of vacancies. Also, application of the above Turing models to Zircaloy oxidation requires that an increase in at least one of these species (monoclinic phase content or vacancy concentration) to cause an increase in the rate of the reactions which occur at the two interfaces of the oxide layer. Identifying such mechanisms requires a detailed understanding of the chemistry of the oxide layers and is beyond the scope of this thesis.

5.3 An alternative model for Zircaloy oxidation

Turing models proposed in the previous section are fairly restrictive, requiring a long list of criterion to be satisfied (refer Equation (4.2)). In this section, we will discuss an alternative mathematical model which requires only a subset of the Turing conditions to be satisfied in order to reproduce a periodic oxidation behavior. However, there are certain limitations of this model which we will discuss later.

5.3.1 Mathematical structure

We consider a system of three variables corresponding to the concentration of the sub-stoichiometric tetragonal phase (u, moles of tetragonal zirconia per unit volume of the oxide), pore density (v, number of pores per unit volume of the oxide), and grain boundary oxygen ions (p, moles of oxygen ions present in the grain boundaries per unit volume of the oxide). Note that the remaining matter in the oxide is assumed to be comprised of monoclinic zirconia and dopant/impurity atoms. $0 < x < h(t)$ and t correspond to spatial and temporal coordinates respectively. $h(t)$ is the thickness of the oxide layer at time t, and $x = 0$ is the free surface (oxide/oxygen environment interface). Their evolution is assumed to be

governed by the following differential equations

$$\frac{du}{dt} = f(u,v) = \sigma(aC_O - k_1 v) \tag{5.33}$$

$$\frac{dv}{dt} = g(u,v) = \sigma k_2 (u - u_0) \tag{5.34}$$

$$\frac{\partial p}{\partial t} = D_p \frac{\partial^2 p}{\partial x^2} + \omega(u,v) = D_p \frac{\partial^2 p}{\partial x^2} - \sigma k_3 p \tag{5.35}$$

$$\sigma = \exp\left[-st\left(1 - \left(\frac{x}{h}\right)^n\right)\right] \tag{5.36}$$

D_p is the diffusion coefficient for the grain boundary oxygen ions. Parameters a, k_1, k_2, k_3, s, u_0 and $(n > 1)$ are system constants. C_O is the concentration of oxygen that reacts with zr. Though the physics requires the diffusion coefficients of u (tetragonal oxide) and v (pores) to be 0, a negligibly small value of these needs to be specified during simulations for numerical stability. Parameters a, k_1, k_2, k_3, A, u_0 and $(n > 1)$ are system constants. σ represents the normalized compressive stress which has a maximum value of 1 at the metal-oxide interface (corresponding to the theoretical Pilling-Bedworth stress of 56 GPa). It quickly reduces away from the interface and replicates the stress-relaxation behavior observed in the oxide layers C:ch2. This quantity is used as a simple mathematical multiplier as an approximation to capture the physical effects of compressive stress promoting the lower volume tetragonal phase (refer Equation (5.33)), as well as the formation of pores (refer Equation (5.34)). Its presence in Equation (5.35) ensures an oxygen consumption (or formation of new oxide) primarily in the high-stress regions near the metal-oxide interface. Nature of interaction between the tetragonal phase of the oxide (u) and the pores (v) results in a time-oscillatory behavior in their concentrations near the metal-oxide interface. In the next section, we will present a mathematical analysis of Equations (5.33) and (5.34) understand this process.

5.3.1.1 Simplified analysis

In Equations (5.33) and (5.34), spatial dependence is introduced by the stress multiplier σ. For simplicity, we will assume it to be uniform to understand the behavior of these equations with respect to time. These equation then reduce to

$$\frac{du}{dt} = (c_1 - c_2 v) \tag{5.37}$$

$$\frac{dv}{dt} = c_3(u - u_0) \tag{5.38}$$

where c_1, c_2, c_3 are constants. Note that these equations require the species to satisfy the criterion of cross-activation and cross-inhibition, which is only a subset of the Turing instability conditions listed in Equation (4.2). Taking time derivative of Equation (5.37) and substituting Equation (5.38) in it, we get

$$\frac{d^2u}{dt^2} = -c_2 c_3 (u - u_0) \tag{5.39}$$

We then have

$$u = B\sin(\omega t) + u_0 \tag{5.40}$$

$$v = \frac{c_1 - B\omega\cos(\omega t)}{c_2} \tag{5.41}$$

where

$$\omega = \sqrt{c_2 c_3}\ ; \quad u_0 = u_{t=0} \tag{5.42}$$

u and v are therefore oscillate periodically in time with the same frequency (ω). Notice that Equations (5.33) and (5.34) indicate that the time-derivatives in u and v are significantly more dominant in the regions adjacent to the metal-oxide interface. As a result, the oscillatory behavior is also limited to this region. If the rate of formation of the oxide is dependent on either u or v, it will also show a time-periodic behavior. Furthermore, as u, v

do not diffuse, a moving metal-oxide interface causes a time-periodic behavior to result in a spatially periodic distribution of these species.

5.3.2 Model details

Details of the model physics are discussed in this section.

The metal-oxide front is assumed to move at a rate that is proportional to the lattice oxygen (within the already formed oxide grains) as well as the oxygen that arrives diffusing through grain boundaries (see Figure 5.11). As the lattice structure of the tetragonal phase favors the presence of vacancies in it, we assume that the vacancy concentration in the oxide is proportional to concentration of this phase (u). Therefore, the rate of reaction or the rate of increase of oxide thickness can be written as

$$\frac{dh}{dt} = k((A - bu) + p) \tag{5.43}$$

where A is a constant corresponding to the concentration of oxygen lattice sites in stoichiometric zirconia. The term $[bu]$ represents the vacancy concentration (b is a proportionality constant). p is the concentration of the grain boundary oxygen ions.

Next, we would discuss the physics of the form of function $f(u, v)$ in Equation (5.33). First term in the bracket (aC_o) represents the increase in tetragonal concentration due to the formation of the new oxide upon reaction of zr with oxygen. The second term ($-k_1 v$) represents the transformation of tetragonal to the monoclinic phase with pores (v) acting as a sink for tetragonal stabilizing vacancies. As both of these effects are enhanced by compressive stress, we use that as a multiplier here. Also, we approximate the oxygen concentration as

$$C_O = (A - bu) + p \approx p \tag{5.44}$$

Keeping the first term in the above expression leads to a behavior with only a few initial transitions in the oxidation kinetics, followed by a constant rate of motion. Notably, such

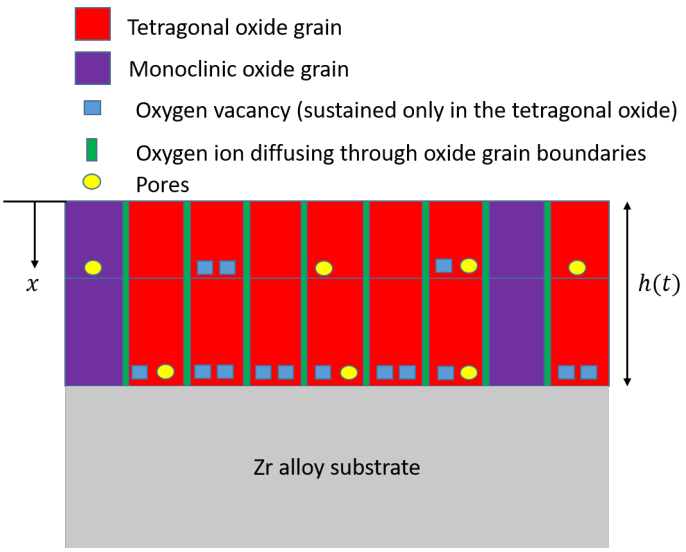

Figure 5.11: Oxide structure considered for the mathematical model outlined in Section 5.3.

behavior has been reported in certain zirconium oxidation experimental studies. However, in this study, we focus on cases exhibiting with a periodic oxidation kinetics for $t \to \infty$ for the purpose of demonstrating the key physics of the transitions. The argument for including grain boundary oxygen in this model is also the same, i.e, if we consider only the first term $[A - bu]$, the system does not exhibit a periodicity.

Now, we would discuss the physics of form of function $g(u, v)$ in Equation (5.34). As the tetragonal concentration (u) [or the vacancy concentration in the oxide which is assumed to be proportional to u] increases beyond a certain value, it results in pore formation by vacancy condensation, and destruction of pores below it. Condensation of vacancies is promoted by the compressive stress, and hence the use of multiplier σ.

In Equation (5.35), the function $\omega(u, v)$ represents consumption of grain boundary oxygen in forming the new oxide. Recall that formation of new oxide in zr results in a theoretical stress of 56 GPa at the metal-oxide interface which quickly relaxes away from it. Furthermore, due to significantly low diffusivity of zr ions, the oxidation happens primarily near the metal-oxide interface. σ is therefore used as a multiplier to capture this effect. Evolution of stress-multiplier σ is shown in Figure 5.12. Sharp gradients at the metal-oxide interface

correspond to a quick stress-relaxation from the Pilling-Bedworth stress of 56 GPa, via plastic deformation (dislocation glide). The rate of stress-relaxation decreases with time. Note that we could have directly used the creep-based equations outlined in C:ch2 to model the effect of the oxide stress. However, using an expression such as in Equation (5.36) allows for a relatively simple framework while capturing the basic characteristics of stress-relaxation observed in the oxide films.

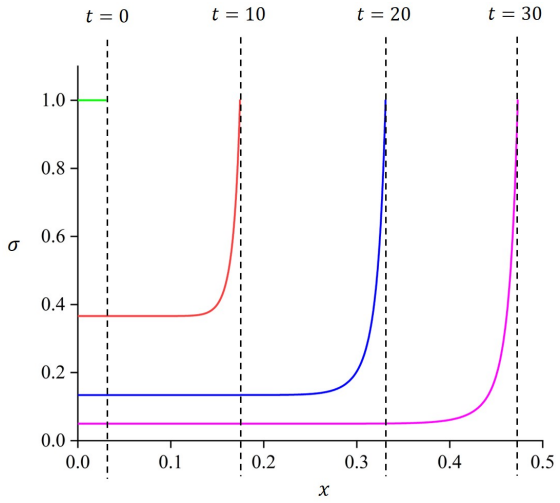

Figure 5.12: Evolution of stress-multiplier σ used in Equations (5.33), (5.34) and (5.36)

The boundary conditions are as follows

$$\frac{\partial u}{\partial x}(0,t) = 0 \; ; \quad \frac{\partial v}{\partial x}(0,t) = 0 \; ; \quad p(0,t) = p_0 \tag{5.45}$$

and

$$\frac{\partial u}{\partial x}(h(t),t) = 0 \; ; \quad \frac{\partial v}{\partial x}(h(t),t) = 0 \; ; \quad \frac{\partial p}{\partial x}(h(t),t) = 0. \tag{5.46}$$

5.3.3 Model predictions

In this section, we will discuss the predictions of the oxidation model for zirconium alloys presented above. We will also draw comparisons with experimental observations wherever relevant.

5.3.3.1 Pore distribution and oxidation kinetics

Figure 5.13 shows a periodic behavior in the oxidation kinetics for the parameter values of $a = 0.5$, $k_1 = 1$, $k_2 = 1$, $u_0 = 1$, $D_p = 1$, $k_3 = 1$, $s = 1$, $n = 6$, $A = 2$, $b = 1$ and $k = 0.005$ in Equations (5.33)–(5.36), (5.43), (5.45) and (5.46). Also, each transition in the boundary kinetics is observed to approximately correlate with a peak in the pore density. This feature is observed in the microscopic images of the oxide layers formed in zirconium alloys as well. In these observations, the void-like structures tend to dominate in regions where the grain structure changes from columnar to equiaxed. This implies an increased pore density overlaps with transitions in the boundary kinetics (faster rate leads to smaller grain size). If the diffusivity of the grain boundary oxygen p is significantly high, transitions in boundary kinetics will result in a few transitions in the weight-gain kinetics as well. It will however, exhibit a parabolic limiting behavior.

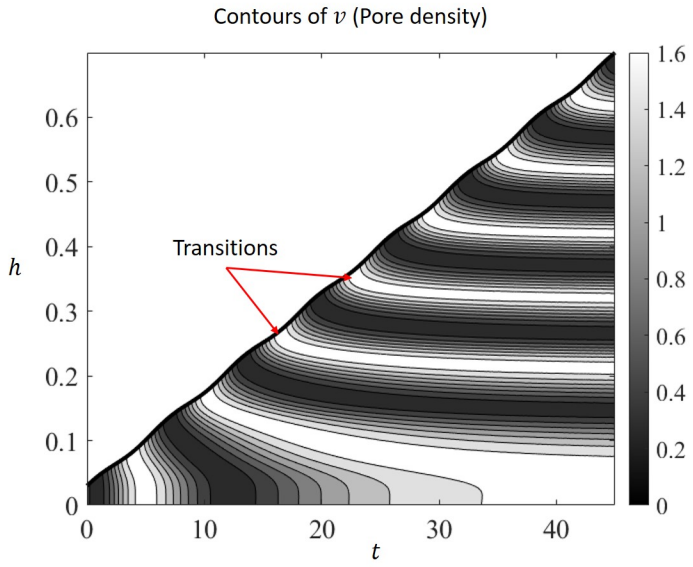

Figure 5.13: Contours of pore density (v) obtained from the model of section Section 5.3. Parameter values of $a = 0.5$, $k_1 = 1$, $k_2 = 1$, $u_0 = 1$, $D_p = 1$, $k_3 = 1$, $s = 1$, $n = 6$, $A = 2$, $b = 1$ and $k = 0.005$ are used in Equations (5.33)–(5.36), (5.43), (5.45) and (5.46). The results show a spatial periodicity in pore distribution correlated with the transitions in the boundary kinetics (as observed experimentally in zr oxide layers)

5.3.3.2 Phase distribution and oxidation kinetics

Figure 5.14 shows the contours of the tetragonal phase distribution (u). Note that a negative peak in u increases the rate of boundary movement by reducing the vacancy concentration. This also agrees well with the experimental observation of a drop in the tetragonal content near a transition.

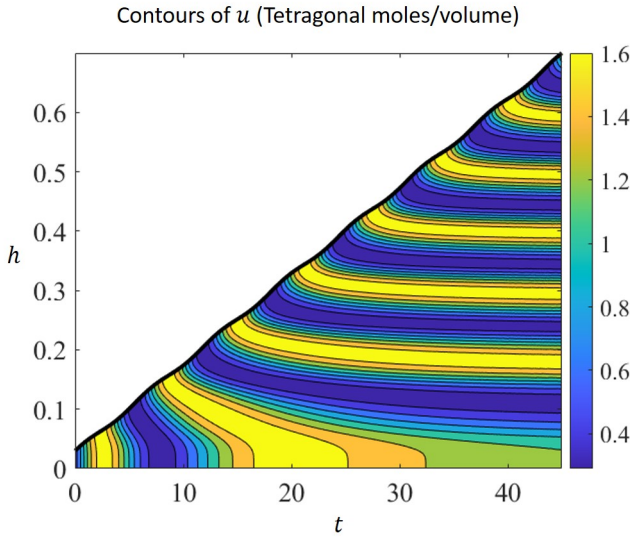

Figure 5.14: Phase distribution obtained from the model of section Section 5.3. Parameter values of $a = 0.5$, $k_1 = 1$, $k_2 = 1$, $u_0 = 1$, $D_p = 1$, $k_3 = 1$, $s = 1$, $n = 6$, $A = 2$, $b = 1$ and $k = 0.005$ are used in Equations (5.33)–(5.36), (5.43), (5.45) and (5.46). It shows a spatial periodicity that is approximately correlated with the transitions in the boundary kinetics (as observed experimentally in Zr oxide layers). Also, after initial transients, the phase content does not change away from the interface.

5.3.4 Limitations

Model presented in this section is less restrictive as compared to the Turing models, in terms of the criterion which need to be satisfied in order to reproduce the periodic oxidation behavior of zirconium alloys. That allowed us to identify underlying the physical processes which could lead to the mathematical structure that produces the desired behavior. However, there are some limitations to this model. The choice of boundary conditions used in the model for vacancies and the grain-boundary oxygen are not particularly applicable for an oxidation system. Our attempts to reproduce this behavior with more reasonable boundary

conditions were not successful. Also, the power-law exponent for each oxidation cycle is super-parabolic in this model whereas experiments indicate it to be slightly sub-parabolic (approximately cubic). The weight-gain kinetics for this model will be limited by diffusion and hence will show a parabolic behavior for long enough time duration. However, weight measurements have only shown it to remain linear and never transitioning to a parabolic kinetics. This could also just be a consequence of significantly large diffusivity and not running the experiments long enough. Lastly, though the physical mechanisms identified here may qualitatively satisfy the main characteristics of Equations (5.33) and (5.34), the exact mathematical forms may be different.

5.4 Conclusions

In this chapter, we proposed several candidate mathematical models which reproduce the oxidation behavior of zirconium alloys. One set of such models is obtained by extending the Turing framework of C:ch4 to three-species models which exhibit transitions not only in the boundary kinetics, but also in the weight-gain kinetics, as observed experimentally for oxidation of several material systems including Zircaloys [19, 20, 21]. We proposed a simplified mathematical model that only requires a subset of Turing conditions to be satisfied. Underlying physical mechanisms could thus be identified for this model with reasonable confidence, unlike the Turing models. We also discussed the limitations of this model in its physical arguments as well as its agreement with the experimental observations in Zircaloys.

Chapter 6

Conclusions and Future Work

We started this work with the aim of developing a mathematical understanding of the physical mechanisms which govern the oxidation behavior of zr alloys. The peculiar observations of periodic accelerations in the oxidation kinetics (transitions) and a correlated layered appearance of the oxide formed on these alloys is well documented in the literature. Mode-I (or through-thickness) cracking and micro-porosity caused by the martensitic phase transformation of the tetragonal phase of the oxide to the monoclinic phase are postulated to be the primary causes of this behavior. In chapter 2 of this thesis, we developed a creep-based mechanistic model to understand the evolution of stresses within the oxide for a given time versus temperature profile. The aim was to predict if the stress-state within the oxide can allow for through-thickness cracks to form near an observed transition in the oxidation kinetics. We use experimental data in the literature to estimate the elastic, thermal, oxide-growth, and creep components of the strain and the model predictions were compared against a different set of experimental data for the purpose of validation. Dislocation glide in the oxide and power-law creep in the Zircaloy substrate are shown to be the most significant creep-mechanisms. Further analysis shows that the creep of the oxide remains the dominant factor in driving the stress-relaxation for temperatures up to $\sim$ 900 K, while the creep of the substrate becomes significant only at higher temperatures. Stress-distribution across the oxide layer was also studied. For a temperature of 633 K, the model predicts the oxide to be under large in-plane compressive stress near the first observed transition, ruling out any

possibility of formation of through-thickness crack within the oxide which could have allowed an unrestricted access to the metal-oxide interface by the oxidizing species.

In chapter 3 of thesis, we developed a free-energy framework to understand the energetics of the martensitic transformation of the tetragonal phase of the oxide to the monoclinic phase. Using 3D finite-element simulations to obtain the strain energy barrier, we show that loss in coherency at the interface between the transforming grain and the oxide matrix plays a significant role in reducing the transformation energy barrier. We also observed that the columnar grains offered a lower energy barrier for transformation than equiaxed grains due to a better accommodation of the shear eigen-strain. Stress-relaxation is shown to have a negligible influence on the strain-energy barrier, presenting a contradiction with previous claims in the literature that reduction of the stress to a critical value drives a bulk-transformation that results in a transition in the oxidation kinetics. However, we cannot rule out the possibility of a bulk-phase-transformation due to a sudden change in the concentration of a chemical species based on a continuum-based analysis. The free-energy change for transformation obtained from the continuum analysis for equiaxed grains was highly positive, indicating that it is unfavorable. However, experimental data indicates to the contrary. Therefore, we carry out molecular-dynamics simulations to analyze the effect of crystal defects present in the oxide layer on the relative stability of these phases. We show that oxygen ion interstitial and tin substitutional defect significantly increase the driving force for transformation to the monoclinic phase. As tin is one of the primary alloying element in Zircaloys and also that the probability of having oxygen interstitials defects near the free surface of the oxide (where equiaxed grains are located) is high, these atomistic level simulations can explain the inconsistency between the continuum-analysis and the experimental observation mentioned above.

As a periodic structure of the oxide is a dominant feature of Zircaloy oxidation, in Chapter 4 of this thesis, we focused on the interaction between pattern-forming Turing instability and a moving boundary. We assume that the rate of boundary movement is controlled by

the species involved in forming patterns. The results show behavioral regimes where the boundary-kinetics is observed to be periodic. The transitions observed in the boundary kinetics are found to be a result of periodic development of peaks in concentration of the species at the moving boundary. These peaks leave a transient pattern in the wake which may settle into a stationary pattern of the same wavelength, or it may evolve to a different and stable wavelength through peak-splitting or peak-decay, or settle to a stable homogeneous state. It is in the first scenario that we get a correlated periodicity between the boundary-kinetics and the pattern left behind the moving front, a behavior experimentally observed for the oxidation in zr alloys. Furthermore, two kinds of periodic boundary kinetics behaviors are obtained for the two mathematical models considered in this study. One shows convex-up segments of the boundary kinetics separated by transitions (as observed in Zr, Ti alloys), while the second category shows periodic concave-up segments (as observed in some Ni-Cr alloys). Therefore, this work has potential applications to oxidation behavior in other materials as well.

Chapter 5 of this thesis concentrated on the mathematical modelling of periodic oxidation behavior in Zircaloys. We proposed modifications of Turing models proposed in C:ch4 which exhibit a periodicity in the weight-gain kinetics along with the boundary kinetics. The primary oxidizing species (e.g oxygen ion) was considered to be independent of the pattern forming process. However, by assuming a dependence of rate of reaction at the interfaces to be controlled by the activator (v), inhibitor species (u), transitions are observed in the oxidation kinetics, while u, v form stationary periodic concentration distributions. We also proposed an alternative oxidation model which gives transitions in the boundary kinetics, due to the transients in the tetragonal phase of the oxide and pores producing oscillations in the local vacancy concentration at the metal-oxide interface. A high diffusivity of the oxidizing species will then result in a few transitions in the weight-gain kinetics as well. These transients scale with the magnitude of the in-plane compressive stress within the oxide, and hence the oscillations are also localized near the highly-stressed metal-oxide interface region.

Also, because both the tetragonal oxide and the pores can't diffuse, the local oscillations at the M-O interface then settle into stationary periodic spatial distributions of the tetragonal phase content and pores. This is in agreement with the experimental observations in Zr alloys.

In summary, the work presented in this thesis furthers a largely experimental literature of oxidation in Zr alloys with a detailed quantitative understanding of the underlying physical mechanisms. The models proposed for stress-relaxation and phase transformation can be easily incorporated in large-scale simulations of the pressurized-water-reactors. Previous studies modelled the transitions in the oxidation kinetics using through-thickness cracking, which we show to be a non-reasonable assumption in C:ch2 of this thesis. To the best of our knowledge, this is the first time rigorous mathematical models for periodic oxidation behavior of Zr alloys have been proposed without making the assumption of oxide cracking.

Due to the lack of appropriate experimental data, we had to use creep properties of commercially manufactured zirconia (yttria-stabilized-cubic zirconia) to obtain certain parameters in the stress-relaxation model presented in this thesis. Validation of these model parameters requires direct experimental investigation to obtain the creep data for the oxide layers formed on zr alloys. Furthermore, understanding the chemistry of oxide layer, e.g, interaction between various crystal defects, oxide phases, ions, and electrons, both in the bulk and interface is critical to modelling of oxidation in zr alloys. Certain experimental studies indicate that the bulk of the oxide layer may be stoichiometric to slightly super-stoichiometric in oxygen, in contrary to the general assumption of an anion-deficient oxide. To understand such systems, one needs a clear understanding of the behavior of interstitial oxygen in zirconia, corresponding solubility limit, and the form it exists in after it reaches saturation. This region of the phase diagram of zirconium-oxygen is not well explored. However, it can play a significant role in understanding the physical mechanisms which drive transitions in the oxidation kinetics. Atomistic calculations or experimental studies of diffussivity of various sub-oxides of zr can be useful in understanding the role of the metal-oxide

interface in controlling the oxidation behavior of these alloys. Elemental composition profiling of the void-like regions that are observed to form in the oxide layer near every transition can improve our understanding on their possible connection with the observed acceleration in the oxidation kinetics.

BIBLIOGRAPHY

[1] A. T. Motta, A. Couet, and R. J. Comstock, "Corrosion of zirconium alloys used for nuclear fuel cladding," *Annu. Rev. Mater. Res.*, vol. 45, pp. 311–343, 2015.

[2] A. Yilmazbayhan, E. Breval, A. T. Motta, and R. J. Comstock, "Transmission electron microscopy examination of oxide layers formed on zr alloys," *Journal of Nuclear Materials*, vol. 349, no. 3, pp. 265–281, 2006.

[3] A. Yilmazbayhan, A. T. Motta, R. J. Comstock, G. P. Sabol, B. Lai, and Z. Cai, "Structure of zirconium alloy oxides formed in pure water studied with synchrotron radiation and optical microscopy: relation to corrosion rate," *Journal of Nuclear Materials*, vol. 324, no. 1, pp. 6–22, 2004.

[4] T. Arima, T. Masuzumi, H. Furuya, K. Idemitsu, and Y. Inagaki, "The oxidation kinetics and the structure of the oxide film on Zircaloy before and after the kinetic transition," *J. Nucl. Mater.*, vol. 294, no. 1-2, pp. 148–153, 2001.

[5] E. Polatidis *et al.*, "Residual stresses and tetragonal phase fraction characterisation of corrosion tested zircaloy-4 using energy dispersive synchrotron X-ray diffraction," *J. Nucl. Mater.*, vol. 432, no. 1-3, pp. 102–112, 2013.

[6] N. Petigny, P. Barberis, C. Lemaignan, C. Valot, and M. Lallemant, "In situ XRD analysis of the oxide layers formed by oxidation at 743 K on Zircaloy-4 and Zr-1NbO," *J. Nucl. Mater.*, vol. 280, no. 3, pp. 318–330, 2000.

[7] H. Swan, M. Blackmur, J. Hyde, A. Laferrere, S. Ortner, P. Styman, C. Staines, M. Gass, H. Hulme, A. Cole-Baker *et al.*, "The measurement of stress and phase fraction distributions in pre and post-transition zircaloy oxides using nano-beam synchrotron x-ray diffraction," *Journal of Nuclear Materials*, vol. 479, pp. 559–575, 2016.

[8] F. Garzarolli, H. Seidel, R. Tricot, and J. Gros, "Oxide growth mechanism on zirconium alloys," in *Zirconium in the Nuclear Industry: Ninth International Symposium*. ASTM International, 1991.

[9] J. Godlewski, "How the tetragonal zirconia is stabilized in the oxide scale that is formed on a zirconium alloy corroded at 400 c in steam," in *Zirconium in the nuclear industry: Tenth international symposium*. ASTM International, 1994.

[10] J. Chevalier, L. Gremillard, A. V. Virkar, and D. R. Clarke, "The tetragonal-monoclinic transformation in zirconia: lessons learned and future trends," *J. Am. Ceram. Soc.*, vol. 92, no. 9, pp. 1901–1920, 2009.

[11] V. Bouineau, A. Ambard, G. Bénier, D. Pêcheur, J. Godlewski, L. Fayette, and T. Duverneix, "A new model to predict the oxidation kinetics of zirconium alloys in a pressurized water reactor," in *Zirconium in the Nuclear Industry: 15th International Symposium*. ASTM International, 2009.

[12] J. Palisaitis, C.-L. Hsiao, L. Hultman, J. Birch, and P. A. Persson, "Direct observation of spinodal decomposition phenomena in inaln alloys during in-situ stem heating," *Scientific reports*, vol. 7, no. 1, pp. 1–8, 2017.

[13] J. D. Murray, "How the leopard gets its spots," *Scientific American*, vol. 258, no. 3, pp. 80–87, 1988.

[14] S. Kondo and R. Asai, "A reaction–diffusion wave on the skin of the marine angelfish pomacanthus," *Nature*, vol. 376, no. 6543, p. 765, 1995.

[15] H. Meinhardt and M. Klingler, "A model for pattern formation on the shells of molluscs," *Journal of Theoretical Biology*, vol. 126, no. 1, pp. 63–89, 1987.

[16] R. L. Cooper, A. P. Thiery, A. G. Fletcher, D. J. Delbarre, L. J. Rasch, and G. J. Fraser, "An ancient turing-like patterning mechanism regulates skin denticle development in sharks," *Science advances*, vol. 4, no. 11, p. eaau5484, 2018.

[17] A. D. Economou, A. Ohazama, T. Porntaveetus, P. T. Sharpe, S. Kondo, M. A. Basson, A. Gritli-Linde, M. T. Cobourne, and J. B. Green, "Periodic stripe formation by a turing mechanism operating at growth zones in the mammalian palate," *Nature genetics*, vol. 44, no. 3, p. 348, 2012.

[18] M. A. Chaplain, M. Ganesh, and I. G. Graham, "Spatio-temporal pattern formation on spherical surfaces: numerical simulation and application to solid tumour growth," *Journal of mathematical biology*, vol. 42, no. 5, pp. 387–423, 2001.

[19] L. Z. Mohamed, W. A. Ghanem, O. A. El Kady, M. M. Lotfy, H. A. Ahmed, and F. A. Elrefaie, "Oxidation characteristics of porous-nickel prepared by powder metallurgy and cast-nickel at 1273 k in air for total oxidation time of 100 h," *Journal of advanced research*, vol. 8, no. 6, pp. 717–729, 2017.

[20] K. S. Srinadh and V. Singh, "Oxidation behaviour of the near α-titanium alloy imi 834," *Bulletin of Materials Science*, vol. 27, no. 4, pp. 347–354, 2004.

[21] S. Y. Kondrat'ev, G. P. Anastasiadi, A. V. Ptashnik, and S. N. Petrov, "Kinetics of the high-temperature oxidation of heat-resistant statically and centrifugally cast hp40nbti alloys," *Oxidation of Metals*, vol. 91, no. 1-2, pp. 33–53, 2019.

[22] M. Mamivand, M. A. Zaeem, H. El Kadiri, and L.-Q. Chen, "Phase field modeling of the tetragonal-to-monoclinic phase transformation in zirconia," *Acta Mater.*, vol. 61, no. 14, pp. 5223–5235, 2013.

[23] F. Yang, X. Zhao, and P. Xiao, "In situ measurement of stresses and phase compositions of the Zirconia scale during oxidation of Zirconium by Raman spectroscopy," *Oxid. Met.*, vol. 81, no. 3-4, pp. 331–343, 2014.

[24] P. Platt *et al.*, "A study into stress relaxation in oxides formed on zirconium alloys," *J. Nucl. Mater.*, vol. 456, pp. 415–425, 2015.

[25] W. Qin, C. Nam, H. L. Li, and J. A. Szpunar, "Tetragonal phase stability in ZrO_2 film formed on zirconium alloys and its effects on corrosion resistance," *Acta Mater.*, vol. 55, no. 5, pp. 1695–1701, 2007.

[26] M. Preuss *et al.*, "Studies regarding corrosion mechanisms in zirconium alloys," *J. ASTM Int.*, vol. 8, no. 9, pp. 1–23, 2011.

[27] H. Wang, Z. Hu, W. Lu, and M. D. Thouless, "A mechanism-based framework for the numerical analysis of creep in Zircaloy-4," *J. Nucl. Mater.*, vol. 433, no. 1, pp. 188–198, 2013.

[28] M. Guerain, C. Duriez, J. L. Grosseau-Poussard, and M. Mermoux, "Review of stress fields in Zirconium alloys corrosion scales," *Corros. Sci.*, vol. 95, pp. 11–21, 2015.

[29] H. J. Frost and M. F. Ashby, *Deformation-mechanism maps: The plasticity and creep of metals and ceramics*. Oxford, UK: Pergamon Press, 1982.

[30] D. Kaddour *et al.*, "Experimental determination of creep properties of zirconium alloys together with phase transformation," *Scr. Mater.*, vol. 51, no. 6, pp. 515–519, 2004.

[31] A. H. Chokshi, "Diffusion, diffusion creep and grain growth characteristics of nanocrystalline and fine-grained monoclinic, tetragonal and cubic zirconia," *Scr. Mater.*, vol. 48, no. 6, pp. 791–796, 2003.

[32] D. L. Douglass, "Oxide plasticity in the oxidation mechanism of zirconium and its alloys," *Corros. Sci.*, vol. 5, no. 4, pp. 255–268, 1965.

[33] B. Baufeld, B. V. Petukhov, M. Bartsch, and U. Messerschmidt, "Transition of mechanisms controlling the dislocation motion in cubic ZrO_2 below 700 °C," *Acta Mater.*, vol. 46, no. 9, pp. 3077–3085, 1998.

[34] M. Parise, O. Sicardy, and G. Cailletaud, "Modelling of the mechanical behavior of the metal-oxide system during Zr alloy oxidation," *J. Nucl. Mater.*, vol. 256, no. 1, pp. 35–46, 1998.

[35] Y.-S. Kim, Y.-H. Jeong, and J.-N. Jang, "Stress measurements during thin film zirconium oxide growth," *J. Nucl. Mater.*, vol. 412, no. 2, pp. 217 – 220, 2011.

[36] M. Blat-Yrieix *et al.*, "Toward a better understanding of dimensional changes in Zircaloy-4: what is the impact induced by hydrides and oxide layer?" in *Zirconium in the Nucl. Industry: 15th Int. Symp.* ASTM Int., 2009, pp. 594–611.

[37] A. T. Donaldson, "Growth in Zircaloy-4 fuel clad arising from oxidation at temperatures in the range 623 to 723 K," in *Zirconium in the Nucl. Industry: Ninth Int. Symp.* ASTM Int., 1991, pp. 177–197.

[38] S. Leistikow, G. Schanz, H. V. Berg, and A. E. Aly, "Comprehensive presentation of extended Zircaloy-4 steam oxidation results (600-1600 deg. C)," Dep. Metallurgy, Atomic Energy Commission of Egypt, Cairo, Egypt, Tech. Rep. IWGFPT–16, 1983.

[39] I. C. Noyan and J. B. Cohen, *Residual stress: measurement by diffraction and interpretation.* New York, USA: Springer-Verlag, 1987.

[40] J. Nakamura, M. Hashimoto, T. Otomo, and S. Kawasaki, "Effects of oxygen partial pressure on oxidation of Zircaloy," *J. Nucl. Mater.*, vol. 200, no. 2, pp. 256–264, 1993.

[41] R. C. Garvie, "The occurrence of metastable tetragonal zirconia as a crystallite size effect," *The journal of physical chemistry*, vol. 69, no. 4, pp. 1238–1243, 1965.

[42] C. Valot, D. Ciosmak, M. Mesnier, and M. Lallemant, "Phase analysis by variable-incidence x-ray diffraction: Application to zirconium oxidation," *Oxidation of metals*, vol. 48, no. 3, pp. 329–345, 1997.

[43] a. Platt, P. Frankel, M. Gass, R. Howells, and M. Preuss, "Finite element analysis of the tetragonal to monoclinic phase transformation during oxidation of zirconium alloys," *Journal of Nuclear Materials*, vol. 454, no. 1-3, pp. 290–297, 2014.

[44] A. Garner, A. Gholinia, P. Frankel, M. Gass, I. MacLaren, and M. Preuss, "The microstructure and microtexture of zirconium oxide films studied by transmission electron backscatter diffraction and automated crystal orientation mapping with transmission electron microscopy," *Acta Materialia*, vol. 80, pp. 159–171, 2014.

[45] A. Evans, N. Burlingame, M. Drory, and W. Kriven, "Martensitic transformations in zirconia—particle size effects and toughening," *Acta metallurgica*, vol. 29, no. 2, pp. 447–456, 1981.

[46] R. C. Garvie and M. V. Swain, "Thermodynamics of the tetragonal to monoclinic phase transformation in constrained zirconia microcrystals," *Journal of materials science*, vol. 20, no. 4, pp. 1193–1200, 1985.

[47] J. Coughlin and E. King, "High-temperature heat contents of some zirconium-containing substances1," *Journal of the American Chemical Society*, vol. 72, no. 5, pp. 2262–2265, 1950.

[48] N. Zhang and M. A. Zaeem, "Role of grain boundaries in determining strength and plastic deformation of yttria-stabilized tetragonal zirconia bicrystals," *Journal of materials science*, vol. 53, no. 8, pp. 5706–5718, 2018.

[49] C. Yin, F. Ye, C. Y. Yin, D. R. Ou, and T. Mori, "An assessment of interatomic potentials for yittria-stablized zirconia," in *Applied Mechanics and Materials*, vol. 492. Trans Tech Publ, 2014, pp. 239–247.

[50] A. M. Turing, "The Chemical Basis of Morphogenesis," *Philosophical Transactions of the Royal Society of London Series B*, vol. 237, pp. 37–72, Aug. 1952.

[51] C. A. Klausmeier, "Regular and irregular patterns in semiarid vegetation," *Science*, vol. 284, no. 5421, pp. 1826–1828, 1999.

[52] M. Mimura and J. Murray, "On a diffusive prey-predator model which exhibits patchiness," *Journal of Theoretical Biology*, vol. 75, no. 3, pp. 249–262, 1978.

[53] A. Gierer and H. Meinhardt, "A theory of biological pattern formation," *Kybernetik*, vol. 12, no. 1, pp. 30–39, 1972.

[54] J. Schnakenberg, "Simple chemical reaction systems with limit cycle behaviour," *Journal of theoretical biology*, vol. 81, no. 3, pp. 389–400, 1979.

[55] I. Prigogine and R. Lefever, "Symmetry breaking instabilities in dissipative systems. ii," *The Journal of Chemical Physics*, vol. 48, no. 4, pp. 1695–1700, 1968.

[56] A. Nakamasu, G. Takahashi, A. Kanbe, and S. Kondo, "Interactions between zebrafish pigment cells responsible for the generation of turing patterns," *Proceedings of the National Academy of Sciences*, vol. 106, no. 21, pp. 8429–8434, 2009.

[57] E. J. Crampin, E. A. Gaffney, and P. K. Maini, "Reaction and diffusion on growing domains: scenarios for robust pattern formation," *Bulletin of mathematical biology*, vol. 61, no. 6, pp. 1093–1120, 1999.

[58] E. Crampin and P. Maini, "Reaction-diffusion models for biological pattern formation," *Methods and applications of analysis*, vol. 8, no. 2, pp. 415–428, 2001.

[59] E. Crampin, W. Hackborn, and P. Maini, "Pattern formation in reaction-diffusion models with nonuniform domain growth," *Bulletin of mathematical biology*, vol. 64, no. 4, pp. 747–769, 2002.

[60] A. Madzvamuse, "Time-stepping schemes for moving grid finite elements applied to reaction–diffusion systems on fixed and growing domains," *Journal of computational physics*, vol. 214, no. 1, pp. 239–263, 2006.

[61] A. Neville, P. Matthews, and H. Byrne, "Interactions between pattern formation and domain growth," *Bulletin of mathematical biology*, vol. 68, no. 8, pp. 1975–2003, 2006.

[62] S. S. Lee, E. Gaffney, and R. Baker, "The dynamics of turing patterns for morphogen-regulated growing domains with cellular response delays," *Bulletin of mathematical biology*, vol. 73, no. 11, pp. 2527–2551, 2011.

[63] A. L. Krause, M. A. Ellis, and R. A. Van Gorder, "Influence of curvature, growth, and anisotropy on the evolution of turing patterns on growing manifolds," *Bulletin of mathematical biology*, vol. 81, no. 3, pp. 759–799, 2019.

[64] I. Heath, *Tip Growth in Plant and Fungal Cells*. Elsevier Science, 2013.

[65] G. Gu and H. Peng, "Numerical simulation of reaction-diffusion systems of turing pattern formation," *International Journal of Modern Nonlinear Theory and Application*, vol. 4, no. 04, p. 215, 2015.

[66] P. N. McGraw, M. Menzinger, and A. P. Muñuzuri, "Harmonic resonant excitation of flow-distributed oscillation waves and turing patterns driven at a growing boundary," *Physical Review E*, vol. 80, no. 2, p. 026209, 2009.

[67] M. Kærn, M. Menzinger, and A. Hunding, "Segmentation and somitogenesis derived from phase dynamics in growing oscillatory media," *Journal of theoretical biology*, vol. 207, no. 4, pp. 473–493, 2000.

[68] M. Kærn, M. Menzinger, R. Satnoianu, and A. Hunding, "Chemical waves in open flows of active media: their relevance to axial segmentation in biology," *Faraday discussions*, vol. 120, pp. 295–312, 2002.

[69] A. Krichevsky, S. V. Kozlovsky, G.-W. Tian, M.-H. Chen, A. Zaltsman, and V. Citovsky, "How pollen tubes grow," *Developmental biology*, vol. 303, no. 2, pp. 405–420, 2007.

[70] E. Pierson, Y. Li, H. Zhang, M. Willemse, H. Linskens, and M. Cresti, "Pulsatory growth of pollen tubes: investigation of a possible relationship with the periodic distribution of cell wall components," *Acta botanica neerlandica*, vol. 44, no. 2, pp. 121–128, 1995.

[71] A. M. Nesterenko, M. B. Kuznetsov, D. D. Korotkova, and A. G. Zaraisky, "Morphogene adsorption as a turing instability regulator: Theoretical analysis and possible applications in multicellular embryonic systems," *PloS one*, vol. 12, no. 2, p. e0171212, 2017.

[72] B. E. Deal and A. Grove, "General relationship for the thermal oxidation of silicon," *Journal of Applied Physics*, vol. 36, no. 12, pp. 3770–3778, 1965.

[73] I. Barrass, E. J. Crampin, and P. K. Maini, "Mode transitions in a model reaction–diffusion system driven by domain growth and noise," *Bulletin of mathematical biology*, vol. 68, no. 5, pp. 981–995, 2006.

[74] "pde2path - a Matlab package for continuation and bifurcation in systems of PDEs, v2.8, howpublished = http://www.staff.uni-oldenburg.de/hannes.uecker/pde2path/, note = Accessed: 2020-04-25."

[75] A. Madzvamuse, "Stability analysis of reaction-diffusion systems with constant coefficients on growing domains," *International Journal of Dynamical Systems and Differential Equations*, vol. 1, no. 4, p. 250, 2008.

[76] A. Madzvamuse, E. A. Gaffney, and P. K. Maini, "Stability analysis of non-autonomous reaction-diffusion systems: the effects of growing domains," *Journal of mathematical biology*, vol. 61, no. 1, pp. 133–164, 2010.

[77] R. A. Van Gorder, V. Klika, and A. L. Krause, "Non-autonomous turing conditions for reaction-diffusion systems on evolving domains," *arXiv preprint arXiv:1904.09683*, 2019.

[78] J. Jung, H.-J. Shin, Y. Kim, and M. Kawai, "Activation of ultrathin oxide films for chemical reaction by interface defects," *Journal of the American Chemical Society*, vol. 133, no. 16, pp. 6142–6145, 2011.

[79] V. Raghavan and A. Entwisle, "The iron the steel institute special report, no. 93," 1965.